WEIGHT REDUCTION AND MATERIAL CHARACTERIZATION IN A PART USED IN AVIATION APPLICATIONS PRODUCED BY ADDITIVE MANUFACTURING METHOD

EKLEMELİ İMALAT YÖNTEMİ İLE ÜRETİLEN HAVACILIK UYGULAMALARINDA KULLANILAN BİR PARÇADA AĞIRLIK AZALTIMI VE MALZEME KARAKTERİZASYONU

BÜŞRA CANER ALDOĞAN

PROF. DR. BORA YILDIRIM

Supervisor

Submitted to Graduate School of Science and Engineering of Hacettepe University

as a Partial Fulfillment to the Requirements

for the Award of the Degree of Master of Sciences

in Mechanical Engineering

2023

ABSTRACT

WEIGHT REDUCTION AND MATERIAL CHARACTERIZATION IN A PART USED IN AVIATION APPLICATIONS PRODUCED BY ADDITIVE MANUFACTURING METHOD

Büşra CANER ALDOĞAN

Master of Sciences, Department of Mechanical Engineering

Supervisor: Prof. Dr. Bora YILDIRIM

June 2023, 95 pages

Optimizing design in the aviation sector without altering load paths, achieving fuel savings through weight reduction, reducing carbon footprint, and gaining high maneuverability for aircraft through such improvements remain key areas open to continuous development in this field. To achieve these goals, novel technologies are being developed. However, design and production must be compatible with each other in order to attain this goal. Traditional production methods often limit design in terms of producibility. To overcome this situation, topology optimization has emerged as a prominent tool in recent years, in addition to additive manufacturing. Specific constraints and target values are assigned to the component to reduce the weight of the part and improve its stress values compared to the initial design. Additionally, the control of the compliance is taken into account to ensure it remains within a certain stiffness range.

In this thesis, optimization was performed on a structural component that already exists in a helicopter. The selected component is made of Al 6061 T62 and is connected through welding. By applying topology optimization to the part, load paths were initially determined,and the material was removed in areas where high stress was not expected, resulting in a total weight reduction of 15.7 %. Modal analysis was conducted to evaluate if the vibration values increased while achieving lightweight. While the initial vibration value was 60 Hz, which was increased to 67 Hz after applying topology optimization with material change for analysis. This vibration analysis is crucial since it affects the lifespan of the component.

Simultaneously, AlSi10Mg material, which is one of the most suitable materials for SLM manufacturing method in terms of strength and superior to Al 6061 material, has been subjected to tensile coupon tests. However, this material exhibits different mechanical properties in different directions due to its anisotropic nature. Therefore, the experiments were carried out the SLM method to produce the material in different directions and geometries. Coupon samples were subjected to stress relief, destructive and non-destructive testing, and the characterization of AlSi10Mg material was performed. The obtained results served as input for size and topology optimizations aimed at further reducing the weight of the optimized parts. These optimized designs were then subjected to modal analysis and the resulting natural frequency values were compared with the natural frequencies of the helicopter.

According to the static and modal analysis results, it is evident that lower stresses are observed on the optimized part, which has a lighter weight.

Keywords: Additive Manufacturing, Topology Optimization, Size Optimization, Modal Analysis, SLM Production Method, Structural Parts, Material Characterization.

ÖZ

EKLEMELİ İMALAT YÖNTEMİ İLE ÜRETİLEN HAVACILIK UYGULAMALARINDA KULLANILAN BİR PARÇADA AĞIRLIK AZALTIMI VE MALZEME KARAKTERİZASYONU

Büşra CANER ALDOĞAN

Yüksek Lisans, Makina Mühendisliği Bölümü

Tez Danışmanı: Prof. Dr. Bora YILDIRIM

June 2023, 95 sayfa

Havacılık sektöründe yapılan analizlerde yük yollarını değiştirmeyecek şekilde optimum tasarım optimizasyonları yapmak, ağırlık azaltımı ile yakıt tasarrufu sağlamak, karbon ayakizinin azaltılması, ve tüm bu güncellemeler sayesinde hava araçlarına yüksek manevra kabiliyeti kazanılması bu alanda sürekli geliştirilmeye açık, önemli konuların başında gelmektedir. Bunu sağlayabilmek için her geçen gün yeni teknolojiler geliştirilmektedir. Fakat bunun için tasarım ve üretimin birbiriyle uyumlu olması gerekmektedir. Geleneksel üretim methodları çoğu zaman tasarımı, üretilebilirlik yönünden kısıtlamakadır. Bunu aşmak adına son zamanlarda eklemeli imalata ek olarak topoloji optimizasyonu ön plana çıkmaktadır. Belirli kısıtlar ve hedef değerler parçayı hafifletmek ve ilk parçanın gerilim değerinde iyileştirme yapabilmek için parçaya atanmıştır. Öte yandan parçanın esnekliğinin kontrolü sağlanarak belirli bir sertlik değeri içinde kalması göz önünde bulundurulmaktadır.

Bu tezde helikopterde halihazırda bulunan bir yapısal parçanın optimizasyonu yapılmıştır. Mevcut malzeme Al 6061 T62 ve kaynak ile bağlantı yapılan bir komponentir. Topoloji optimizasyonu uygulanarak öncelikle yük yolları belirlenmiş ve yüksek gerilim olmayan yerlerde malzeme boşaltılmasına gidilerek totalde %15.7'lik ağırlık azaltımı da sağlanmıştır.

Ayrıca parçada hafiflik sağlanırken titreşim değerlerinde artış olup olmadığına dair modal analiz yapılmıştır. İlk titreşim değeri 60 iken, topoloji optimizasyonu uygulanmış ve malzeme değişikliği yapılmış parçanın titreşim değeri 67 Hz'e yükselmiştir. Bu titreşim analizi , parçanın ömrünü etkilediği için önem arz etmektedir.

Eş zamanlı olarak eklemeli imalat için SLM üretim methoduna en uygun malzemelerden biri olan ve dayanım açısından Al 6061 malzemesinden daha üstün olan AlSi10Mg malzemesi seçilmiş ve kupon çekme testlerine tabi tutulmuştur. Fakat bu malzeme anizotropik olduğu için farklı yönlerde değişik mekanik özellik göstermektedir. Bu yüzden, deneyler malzemenin farklı yönlerde ve farklı geometrilerde SLM methodu kullanılarak üretilmesi ile tekrar edilmiştir. Kupon numuneleri gerginlik azaltma, tahribatlı ve tahribatsız muayenelere tabi tutulmuştur ve AlSi10Mg malzemesinin karakterizasyon incelemesi yapılmıştır. Elde edilen sonuçlar, optimize edilmiş parçaların ağırlığını daha da azaltmayı amaçlayan boyut ve topoloji optimizasyonları için girdi görevi görmüştür. Optimize edilen bu tasarımlar daha sonra modal analize tabi tutulmuş ve ortaya çıkan doğal frekans değerleri, helikopterin doğal frekansları ile karşılaştırılmıştır.

Statik ve modal analiz sonuçlarına göre, optimize edilmiş kısımda daha düşük gerilmelerin gözlendiği ve daha hafif bir ağırlığa sahip olduğu açıktır.

Anahtar Kelimeler: Eklemeli İmalat, Topoloji Optimizasyonu, Boyut Optimizasyonu, Modal Analiz, SLM Üretim Methodu, Yapısal Parçalar, Malzeme Karakteristiği.

ACKNOWLEDGEMENTS

I would like to express my sincere thanks to my advisor Prof.Dr.Bora Yıldırım and co-advisor Asst Prof. Nurullah Balcı.Without their guidance throughout the project, it might not be completed correctly. I feel lucky to have found such great mentors.

I would also like to thank my collegues at Turkish Aerospace, Mehmet Yahşi, Eren Duzcu, Fatih Tosun and Emrah Yalınız for their valuable support throughout my studies.
I wish to extend my sincere thank to my mother, lovely Zübeyde Caner, and my elder sisters, Nihan Solmaz, Cemre Özdemir for their self-sacrificing devotion to encouraging me. Especially without my mother's prayers, this thesis could not be sustained.

Finally, I would also like to give special thanks to my dear husband, Enver Burak Aldoğan, for his continuous support and understanding during the undertaking of my thesis. He was always with me.
I am deeply indebted to my family for always loving me and backing me up.

Büşra CANER ALDOĞAN

June 2023, Ankara

TABLE OF CONTENTS

LIST OF FIGURES

LIST OF TABLES

SYMBOLS AND ABBREVIATIONS

Symbols

E	Energy Density
P	Laser Power
ϑ	Scanning Speed
h	Scanning Rate
t	Layer Thickness
f(x)	Objective Function
ρ	Penalty Factor
ρ_e	Density Factor
$K_{SIMP(\rho)}$	Penalized Global Stiffness Matrix of an Element
N	A Number of Element in Design Area
u	State Variable
H	Objective Function
G_j	Constraint Function
u	State Variable
F_{tu}	Tension Allowable Stress
F_{ty}	Tension Yield Stress
F_{su}	Shear Allowable Stress
M_x	Moment in X Direction
M_y	Moment in Y Direction
M_z	Moment in Z Direction
X_m	Mass Center of Gravity Position, X
Y_m	Mass Center of Gravity Position, Y
Z_m	Mass Center of Gravity Position, Z

Abbreviations

TO	Topology Optimization
AM	Additive Manufacturing
CAD	Computer Aided Design
CAM	Computer Aided Manufacturing
DFMA	Design and Manufacturing for Assembly
SLA	Stereolithography
DLP	Digital Light Processing
CDLP	Continuous Digital Light Processing
FDM	Fused Deposition Modelling
DMLS	Direct Metal Laser Sintering
SLM	Selective Laser Melting
SHS	Selective Heat Sintering
EBM	Electron Beam Melting
SLS	Selective Laser Sintering
SIMP	Solid Isotropic Material with Penalization
RAMP	Rational Approximation of Material Properties
ABS	Acrylonitrile Butadiene Styrene
PLA	PolyLactic Acid
FEA	Finite Element Analysis
STL	Standard Tessellation Language
PBF	Powder Bed Fusion
N/A	Not Applicable
SEM	Scanning Electron Microscope

1. INTRODUCTION

Additive manufacturing is a prospective manufacturing method for aerospace. By applying optimization to a part, the advantages of the additive manufacturing production method can be further enhanced. Structural optimizations can be applied to the part in terms of size, shape, topography, and topology according to the predetermined target. Topology optimization is accomplished by assigning a density design variable to each element in the design, these variables are 0 and 1. The rationale for topology optimization is to find the ideal material distribution in the specified volume and within limits using the density method. The continuous nature of the design variable may result in intermediary outcomes that lack physical plausibility, owing to the unavailability of intermediary material. To compel the density design variables towards values of 0 and 1, a penalization technique is implemented.

In this thesis, a bracket in the nose section of the helicopter has been redesigned via CATIA V5 program as the case study. It is planned to get rid of the traditional manufacturing constraints of the currently used equipment and to reproduce it with more suitable manufacturing techniques. The limitations of the conventional production method can be expressed as the fact that the welding process is restricted in practice in terms of the accessibility of each sub-part that requires complex assembly in general and the same welding process cannot be applied each time.

The primary aims of the research are to minimize the weight of the component while ensuring that stress values remain the same by formulating a numerical objective function under pre-defined boundary conditions, analyze natural frequency-modes correlation and determining the performance requirements of the product, such as load capacity or stiffness. Additionally, the vibration increment or reduction resulting from weight lose is kept within a certain limit. This analysis has been repeated for both Al 6061 T62 and AlSi10Mg materials.

On the other hand, experiments are carried out to find out the tensile test allowable for AlSi10Mg material which is produced by the SLM method, and to examine the material characteristics in detail. AlSi10Mg is an anisotropic material that could be defined as a material whose physical and mechanical properties could change in different directions. Thus, coupon tests are conducted to see how the mechanical properties are changed in different directions. Then, destructive and non-destructive methods are applied to the

samples. SEM analysis is also performed to observe the failure surface of tensile test samples. Moreover, optical microscope analysis and hardness tests are also conducted on the tensile test coupons to characterize the metallurgical properties of the specimens.

As a result of the experimental study conducted on the AlSi10Mg material, these mechanical property results serve as the basis for utilization in the static and modal analyses of the optimized model.

2. LITERATURE VIEW

In recent years, some production methods have developed faster than others according to the supply-demand relationship and consumption area. The restricted product development duration and lack of creativity have a significant impact on the competitive sector. The period between the design and production phases of an item, regardless of the industry, is crucial.

With the help of CAD, CAM, and analysis software packages, efforts are made to reduce the progress of production. Another important issue for the industry is the manufacturability of complex parts and assemblies in a short time. Conflicts between design and construction requirements may arise in many situations. Conventional production methods may not be suitable for parts with complex shapes or parts where topology optimization methods are applied.

Therefore, numerous design principles, such as those for design and manufacturing for assembly (DFMA) methodologies need to be implemented to design the process (Boothroyd et al, 2002).

The combination of finite element-based topology optimization and additive manufacturing provides creative solutions to various industries while complying with DFMA principles. Particularly, the automotive industry stands out in terms of both optimization applications and active usage rates.

As an example, an optimization method is performed on a transmission gearbox by selecting the design goal and maximum displacement as constraints under multiple load conditions by Liang and Chen (2018). The aim of the variable density algorithm of the topology optimization is to reach optimal material distribution by reducing the deformation energy of the gearbox. Firstly, throughout the structure optimization process, the displacement will first rise, subsequently slowly diminish along with the reduction in gearbox material, and finally, converges to a constant value to ensure the highest stiffness of the gearbox design. As can be seen in Table 2.1 , the optimized gearbox withstands a maximum stress of 158 MPa which is the same as the previous maximum stress level. However, the mass of the optimized gearbox decreases noticeably by 7.6% compared to the proposed model. It is evident that as the weight decreases, the strength and stiffness values are not reduced. As stated in Table 2.1 , the first and second-order natural frequencies have increased by approximately 4.1% and 5.0%, respectively.

Table 2.1 Comparison of the Analysis Results

Dynamic performance index	Initial model	Optimized model	Change rate (%)
Mass (kg)	9.85	9.10	−7.6
Maximum stress (MPa)	158	158	0
Maximum displacement (mm)	0.94	0.89	−5.3
First-order natural frequency (Hz)	865.2	900.3	4.1
Second-order natural frequency (Hz)	960.9	1008.7	5.0

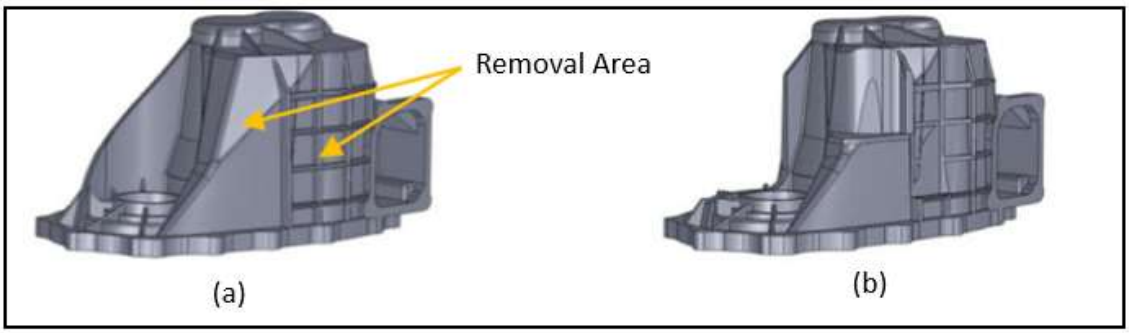

Figure 2.1 Representation of Removal Area on Transmission Gearbox a) Initial Model and b) Optimized Model

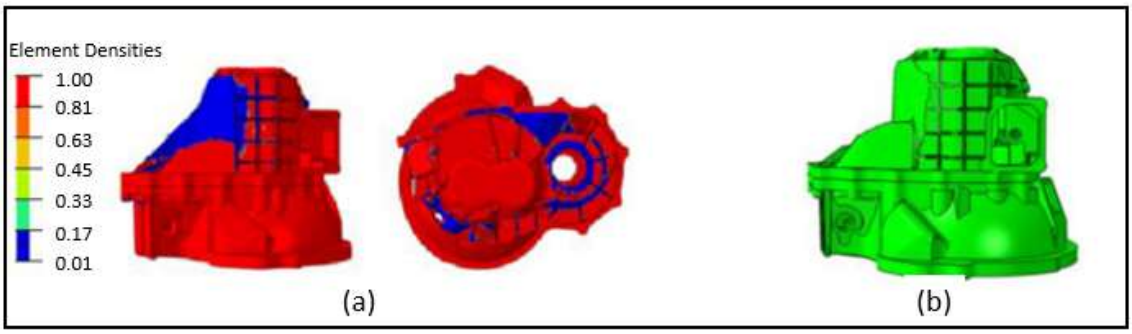

Figure 2.2 The result of Topology Optimization on Transmission GearBox[47]

a) element density representation and (b) optimized model

Shinde, Sheth, Sindkar, and Silas(2021) investigated the engine mounting bracket used in the Peugeot 206 Gti car by applying optimization. Engine mounting components are crucial when it comes to vehicle dynamics. Since the engine produces an extensive amount of noise and shaking, the engine mount bracket is subjected to these disturbances. Both vibration and noise shorten the lifespan of the bracket and also lead to reduced comfort for drivers and passengers. To overcome with these problems, adjusting the dimension of that bracket or material change ise required. According to Shinde, Sheth, Sindkar and Silas, Gray CI material was chosen among the most suitable materials Al, Mg, Gray CI.

The updated design had a deformation of 0.49 mm and an equivalent Von Mises stress of 164.87 MPa, which was considerably lower than the original design's 1.14 mm deformation and equivalent Von Mises stress of 189.11 MPa.

The result of fatigue analysis of the material against the repetitive loads to which it will be exposed throughout its life is shown in the picture below. It was also reported that the natural frequency of the improved design was 257.83 Hz, which was lower than the natural frequency of the preliminary concept, i.e. 268.59 Hz [48].

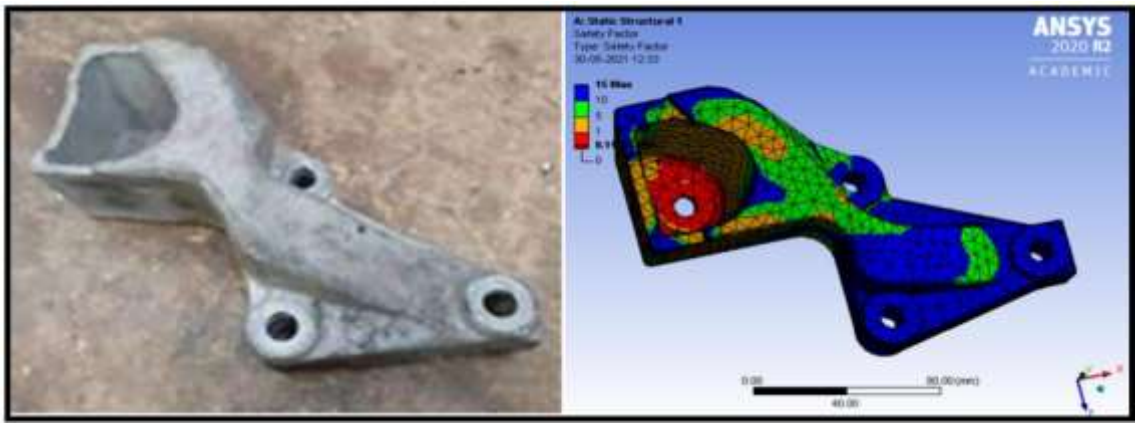

Figure 2.3 The Result Of Fatique Analysis For Engine Bracket [48]

Another promising application of topology optimization and AM is the antenna bracket for RUAG's sentinel satellite, shown in Figure 2.4. As mentioned in reports written by the German Center for Aerospace (DLR) in 2016, space research projects can cost € 20,000 per kilogram of transferred payload. Therefore,each gram that is reduced in the system, impacts launching cost directly. In this circumstance, the Swiss RUAG company required a well-designed antenna attachment. In addition to weight reduction parameter, the frequency of vibration of the bracket was significant as well. Modal analysis is a tool that is commonly utilized to determine the natural frequencies and modal shapes of structural parts. After applying modal analysis to the antenna bracket, it was concluded that the level of frequency was also acceptable.

However, the criteria for stability and robustness are completely opposed to lightweight design for conventional production methods. Thanks to additive manufacturing, an outstanding weight reduction of the finished component dropped from 1.6 kg to 940 g, providing savings of more than 40%. Furthermore, the implementation of additive manufacturing resulted in the minimal stiffness criteria of that part beeing surpassed by more than 30%, even after a turbulent flight.

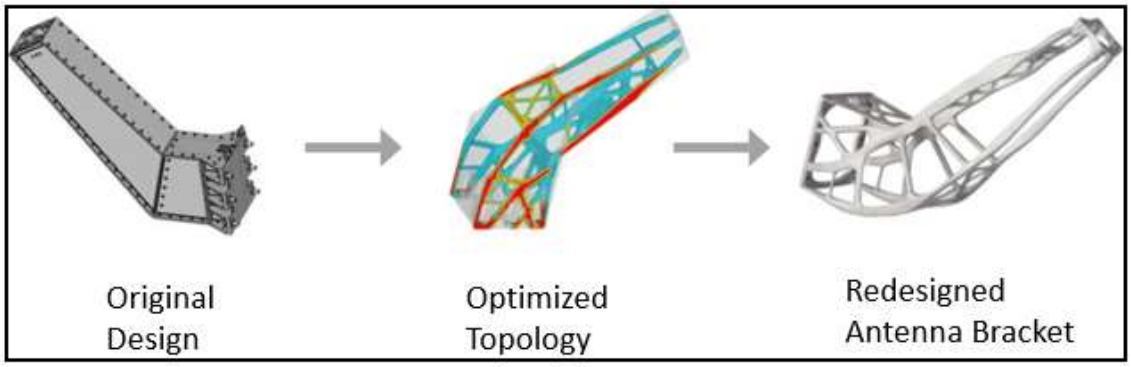

Figure 2.4 Antenna bracket for RUAG's sentinel satellite [46]

It is concluded that more stiffness and lower mass values were achieved concerning the initial sample as can be seen clearly from Figure 2.5. [46].

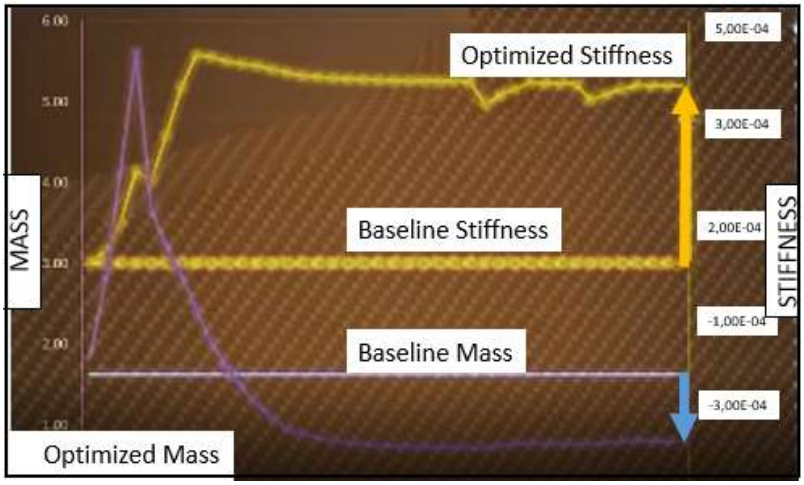

Figure 2.5 The Results of Optimized Antenna Bracket for RUAG's Satellite [46]

Zhu, Zhang, and Xia (2015) have studied the leading edge ribs of the Airbus A380 which were improved to reduce weight while maintaining the specified mechanical characteristics. The action plan resulted in a theoretically different set of ribs shown inFigure 2.6, which met the lightness goal and all stress and buckling requirements specified in the topology optimization [44,45].

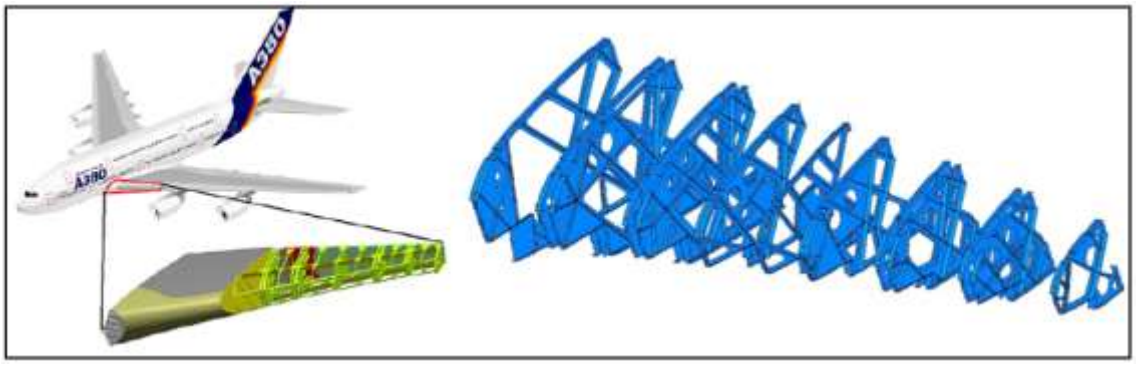

Figure 2.6 Airbus A380 leading edge ribs design using topology optimization [44,45]

Improved rib designs must undergo additional testing and analysis immediately after optimization to control local flange buckling, fatigue, and bird strike. Machining trials and fatigue examinations are currently in progress.

.

2.1 ADDITIVE MANUFACTURING

Material selection and weight saving have been crucial issues in the aircraft industry, as weight increases on structural parts directly impact fuel consumption and flight performance. To tackle with these issues generally, aluminum, titanium and composite materials have been preferred. In fact, the usage of composite structures can be seen as a major step in aviation. However, when comparing composite and metal parts, the usage of metal structures outweighs composite parts in terms of manufacturability, ease of processing, analyzability, and cost.

Additive manufacturing (AM) is another way to turn out parts that are based on the layer-by-layer production of parts instead of subtracting material from raw materials [1].

This novel manufacturing technique enables the fabrication of complex geometries and architectures that would pose significant challenges or be unattainable with conventional manufacturing processes like casting, forging, or machining.

The principal benefit of AM is the capability to produce structural components with lower weight and higher load-bearing capabilities.

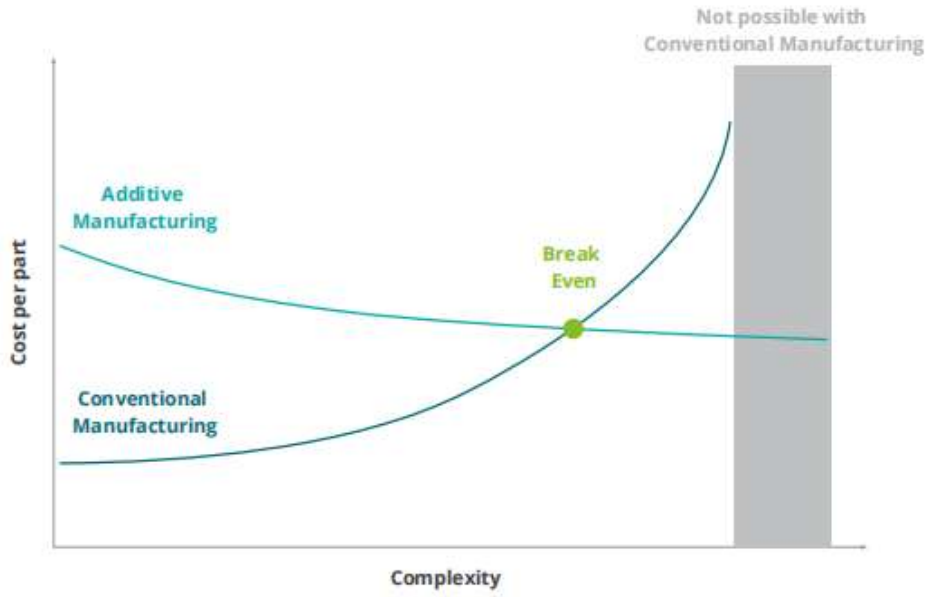

Figure 2.7 Product Complexibility versus Cost : Conventional versus AM [2]

Indeed, versatile design, reducing production costs, customization are made possible by the particular characteristics of AM technology.

These special abilities consist of :

- Design complexity: Without hard toolings, such as molds, dies, or fixtures, additive manufacturing allows for the fabrication of almost any part shape. A significant cost benefit comes from not utilizing molds in additive manufacturing. Moreover, it is possible to create very complicated geometric structures using cellular structures (honeycombs, lattices, foams) or more general structures. Cellular materials (materials with cavities) have high thermal and acoustic insulation qualities as well as good energy absorption capabilities [3]. Following the completion of traditional topology optimization, various lattice structures can be created as size optimization.

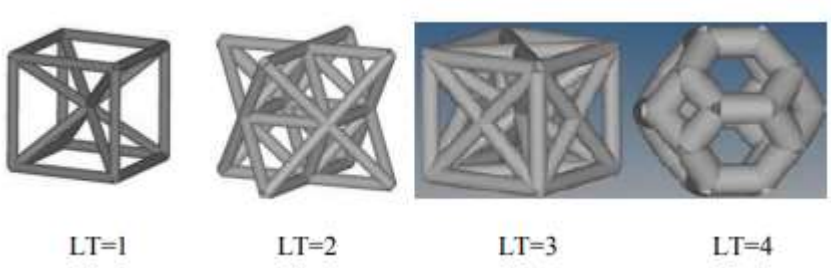

Figure 2.8 Representative Lattice Structures [3]

By combining multiple parts into a single piece, AM can produce lighter weight and higher-performing components than those produced through assembly. As a result, the need for hazardous and life-threatening procedures such as welding and brazing can be reduced or eliminated. In addition to these outputs, AM affects assembly time, maintenance time, spare part inventory and result in cost savings over the lifetime of the product.

- Material Usage: Parts with complicated material compositions and planned property gradients can be produced using additive manufacturing readily. Three-dimensional structures known as lattices are composed of one or more repeating unit cells [4]. These structures can be named as cellular solids, cellular metals, cellular foams and lattice structures [5].

  Lattice structures can achieve a balance between lightweight configurations and high strength. Utilizing lattice structures in additive manufacturing offers the additional benefit of maximizing area use while requiring low material usage. Due to the nature of lattices stretching across nodes with a significant amount of vacant space in between, designers can increase the surface area of a design without

compromising on material usage. Altering the thickness and location of the nodes, beams, or struts allows for incorporating innovative aspects relating to how the component interacts with forces and sound. The use of lattices allows for greater control by designers over shock absorption, impact management, and vibration/noise dampening. Furthermore, designers can protect the important parts of an object by using elements that serve as auxilary features or elements that lessen impact stress. This innovative approach to designing parts through the use of lattices has been shown to have practical implications in various fields, including the aerospace and automotive industries, and has opened up avenues for further research and exploration [6].

Figure 2.9 3D Printed Lattice Structures Demonstration [6]

In the realm of additive manufacturing, the outcome of a printed part is heavily reliant on the selection of appropriate materials as well. In consideration of material properties such as rigidity, weight, and other characteristics, the selection process inevitably influences the lattice's size and density. Notably, lattices printed with more rigid materials tend to offer a greater range of design options, allowing for the creation of thinner members and larger cell sizes. As such, selecting the appropriate material is crucial in achieving the desired performance and properties of a lattice structure. Polymer-based and composite materials have gained significant popularity in the field of additive manufacturing (AM) due to their cost-effectiveness, efficient manufacturing processes, and superior quality. Despite the fact that these materials are generally used, the selection of material varies depending on the process type.

- Functional complexity: Additive manufacturing enables the direct production of complex functional parts that can be used in assembly without the need for additional assembly steps. Monolithic parts, which are single-piece parts, can be produced using additive manufacturing, eliminating the need for assembly of multiple parts. This includes functional parts such as moving parts, such as armor and crank slider mechanisms, as well as gearshifts. Figure 2.10 demonstrates an example of an additively manufactured assembly of the Italian aircraft P180 Avant II by Piaggio Aero Industries S.p.A [7].

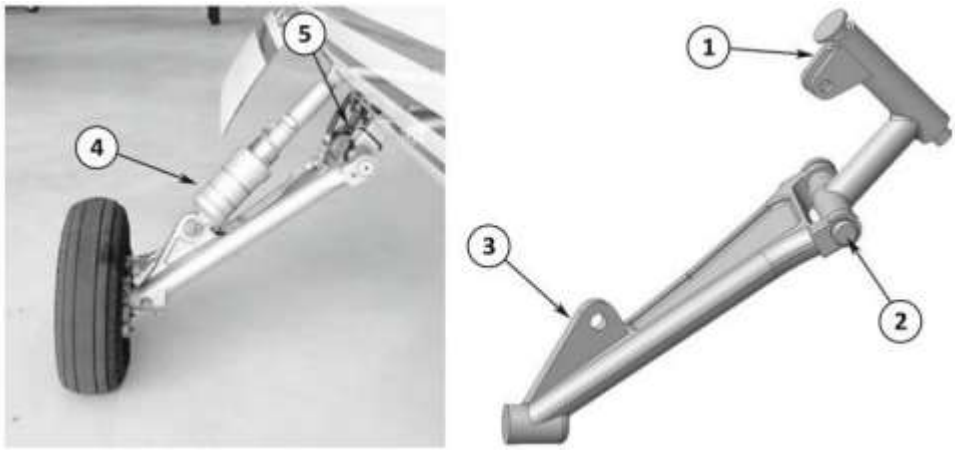

Figure 2.10 Main Landing Gear of the Italian Aircraft P180 Avant II by Piaggio Aero Industries S.p.A [7]

The successful production of these assemblies through additive manufacturing is dependent on proper clearance between its individual parts, which can be achieved through the use of Design for Additive Manufacturing (DFAM) approach. An example of the utilized connection clearance is illustrated in Figure 2.11.

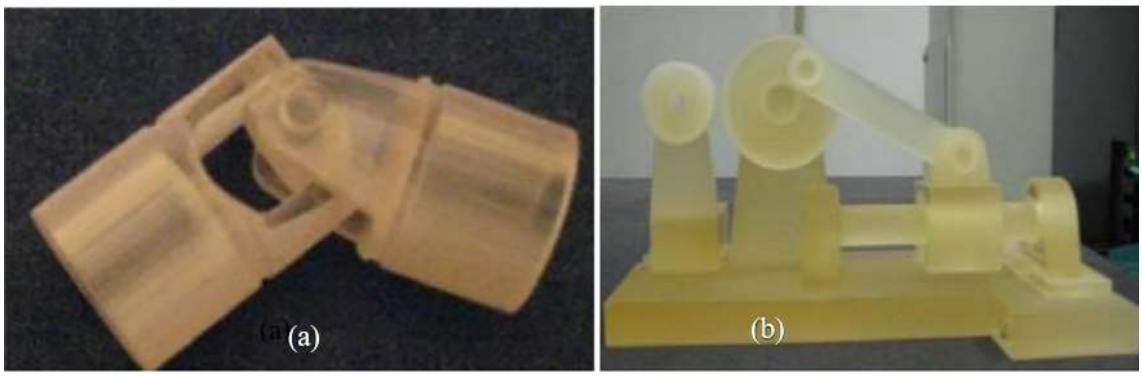

Figure 2.11 Direct Production Of Assemblies (a) joints; (b) crank and slider mechanism [59]

In the aerospace industry, the bulk production of aircraft engine parts using 3D printing was pioneered by GE Aerospace in Alabama. Beginning with the production of fuel nozzles in 2015, Federal Aviation Administration certification was obtained in subsequent years for various engine models such as GE90, CFM LEAP, GEnx, and GE9X. The production process for these parts involves the use of either an electron beam or laser technology.

As a consequence, waste-free, fully dense, complex parts are produced in lesser amount of time required by additive manufacturing. A notable illustration of this is the manufacturing of fuel nozzle tips, which previously required the soldering and welding together of up to 20 components. However, thanks to additive manufacturing, this process now involves producing a single component, resulting in a 25% reduction in weight of the nozzle tip. Figure 2.12 depicts the GEnx jet engine, an exemplary application of additive manufacturing in the aerospace industry [21].

Figure 2.12 GEnx Jet Engine for Boeing 747s [8]

- Hierarchical complexity: It refers to the range of features, sub-features, and other capabilities that can be achieved with AM.

As a result, topology optimization is one of the key strategies to maximize the benefits of AM. However, direct integration of additive manufacturing has been hindered for years due to production limitations on extremely complex shapes and irregular surfaces. Several production methods that are empoyed in additive manufacturing have been developed to address these challenges.

2.1.1 Production Techniques

In recent years, many additive manufacturing techniques have been widely utilized to produce topology-optimized products. These products are chosen for their superior qualities over traditional production methods. The main reasons why these systems are preferred are that they can process various materials (plastic, metal, ceramic, etc.) and do not require specialized support structures, which are key factors contributing to their popularity. Therefore, they are used in the production of parts for important industrial areas such as aerospace, automotive, biomedical, defense industry, and energy sectors. Even though the term "3D Printing" is frequently utilized interchangeably with Additive Manufacturing technology, there are several distinct processes that each uses a different way of creating layers. These processes depend on the type of machine and material used. In response, the American Society for Testing and Materials (ASTM) group "ASTM F42 - Additive Manufacturing" established a set of regulations in 2010 that divided the production processes of additive manufacturing into 7 categories.

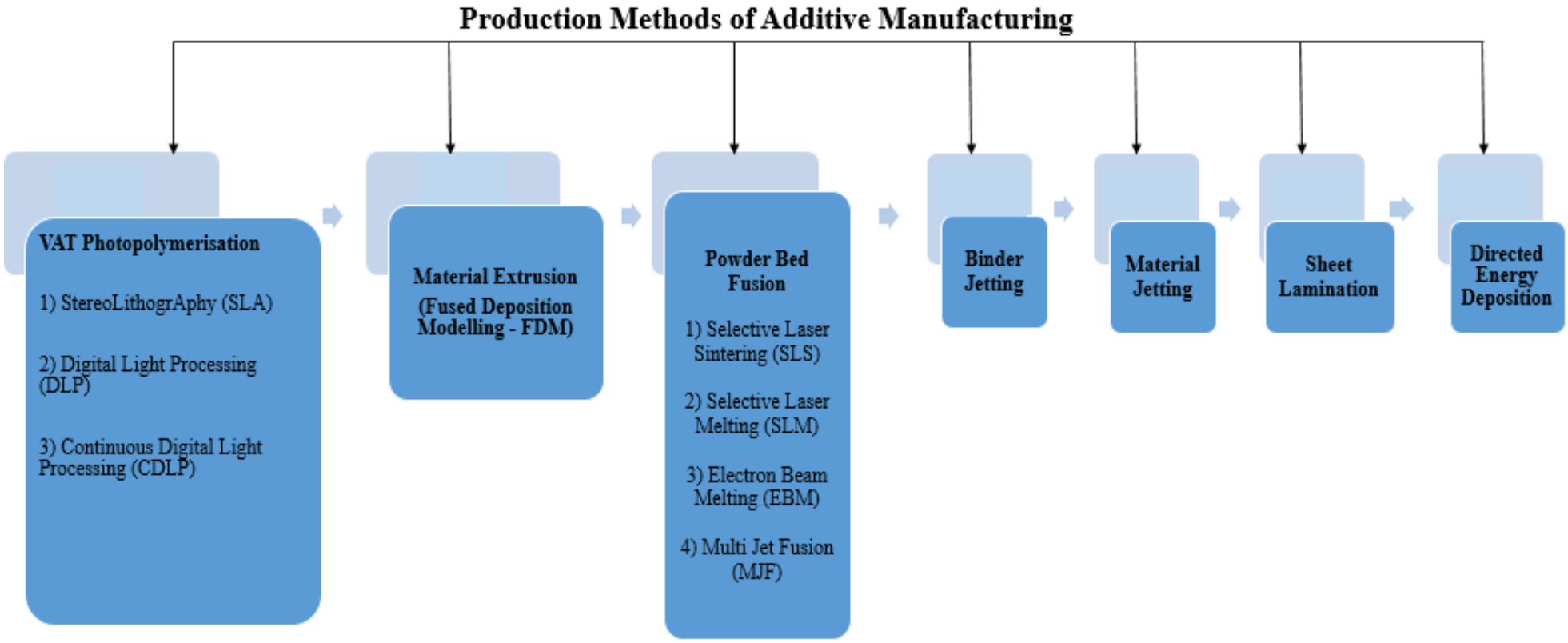

Figure 2.13 Production Methods of Additive Manufacturing

- **VAT Photopolymerisation**

Photopolymerization methods are based on the use of polymer materials that are confined in a vat (or tank) that can solidify by heat source typically ultraviolet light. This process is illustrated in Figure 2.14.

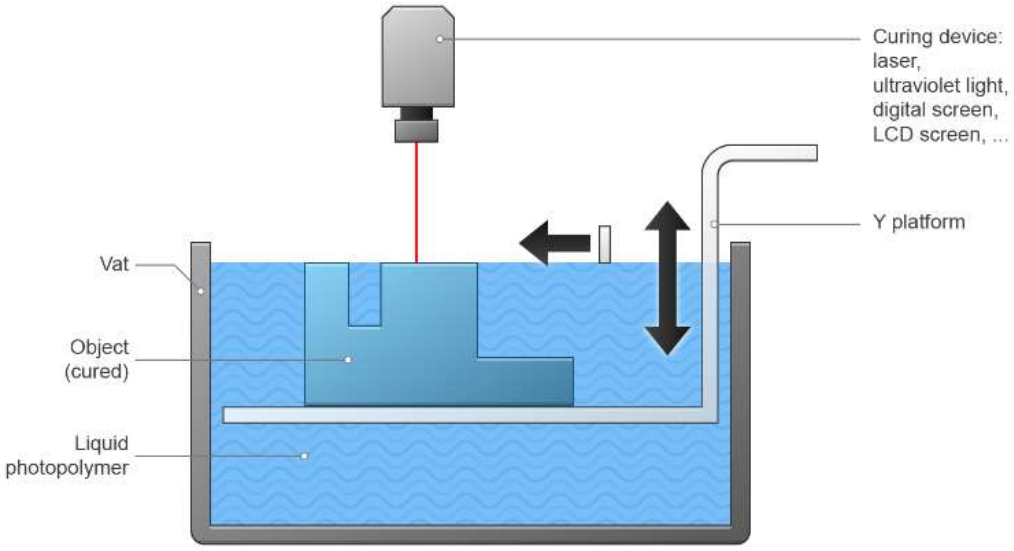

Figure 2.14 VAT Photopolymerisation

In addition to the earliest method, which was used lasers as a heat source, there are many kinds of curing equipment available for photopolymerization methods at current situation. Digital light processing projectors and LCD displays, in particular, have become increasingly popular due to their low cost and high resolution. These approaches have a significant advantage over lasers as they are able to simultaneously cure an entire resin layer, whereas a laser must gradually enlighten the entire surface by moving it. The ability to quickly cure large areas of material with high precision makes digital light processing and LCD displays highly suitable for mass production.

The following are some of the most widely used vat photopolymerization processes for 3D printing;

Stereolithography (SLA), which is often considered the first 3D printing method, was developed in 1986 and enables the cost-effective manufacturing of objects with extremely high surface quality. The main differences between SLA and similar technologies lie in the arrangement of production components, such as the light source, the build platform, and the resin tank. To generate a patterned layer on the resin tank, SLA printing uses a UV laser or a transparent LCD with a UV lamp located below. The surface of the part is

particularly flawless due to the extremely high resolution of the LCD or laser. In SLA printers, the printing time depends on the printing volume rather than the geometry of the part This is due to the fact that the resin used in SLA technology has a very short setting time and solidifies upon exposure to UV light. The cost of producing parts with SLA is also quite convenient when compared to traditional methods. The basic materials used in SLA technology are liquid resin types, and the mechanical and structural characteristics of the final product are directly influenced by the properties of these resin types.

On the other hand, many parameters of the SLA method are available to change the mechanical and structural properties of products. However, the majority of the printer parameters in SLA-type printers are predetermined by the manufacturer and cannot be altered later. Floor height and part direction are variables that can be changed. With a typical layer height of 25 ~ 250 microns in SLA, low layer height allows better results in curved geometries. Nevertheless, low layer height gives rise to increasing the manufacturing process and the risk of errors during printing. For this reason, a height of 100 microns is usually preferred. At Figure 2.15 has been depicted this method.

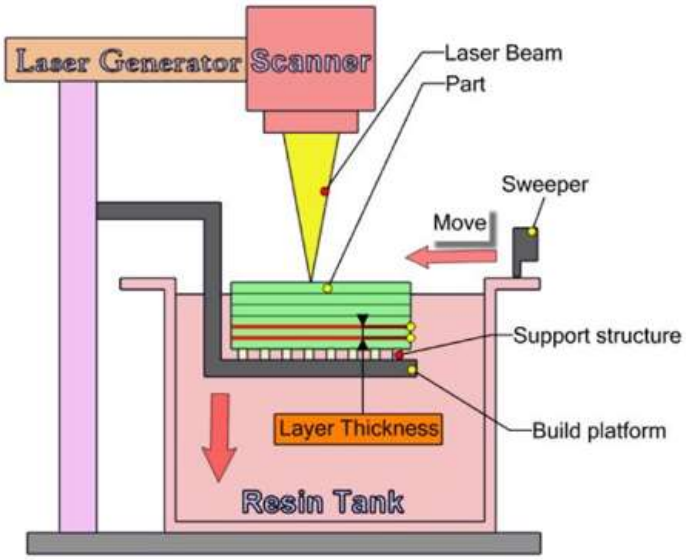

Figure 2.15 Setup of SLA Technology [34]

The another method under VAT Photopolymerization is digital light processing. The DLP 3D printing process utilizes a digital projector screen to instantaneously flash one picture of each layer across the entire platform. Although DLP is quite similar to SLA, DLP machines use projected light to cure the entire layer at once, whereas SLA machines use a laser to trace a layer.

DLP printers have gained widespread recognition for their ability to precisely and efficiently manufacture intricate parts and objects. The reason for their cost-effectiveness is that DLP employs the entire shallow resin vat that is used for each printing process which makes them more affordable for companies. They are usually applied in the orthodontics and audiology sectors owing to their excellent resolution and swift rendering speed. However, there are some disadvantages to DLP printing, such as strong odors produced by melting photopolymers during the printing process and the possibility of warping on larger goods. Additionally, DLP printers are larger than other 3D printers since they contain a projector to project the image to be created. The setup of the DLP production method is shown in Figure 2.16.

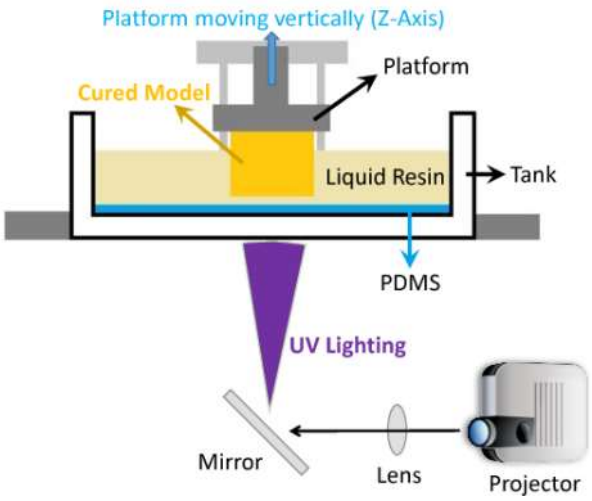

Figure 2.16 The Setup of DLP Production Method [35]

Another vat photopolymerization method is continuous digital light processing (CDLP). In this method, a tank of resin serves as the basic material. There is a window located at the bottom of the vat that is transparent to UV light. Through this window, an ultraviolet light beam enters, revealing the exact cross-section of the object. This light causes the resin to solidify. The item moves gradually enough for the adhesive to flow underneath and remain in contact with the bottom. Underneath the epoxy, an oxygen-permeable membrane provides a dead area. The resin cannot adhere to the glass due to this continuous liquid interface, thus impeding photopolymerization between the window and the polymerizer. Unlike SLA, which has intermittent progress, CDLP promises continuous progress and up to 100 times faster production than existing traditional 3D printing techniques.

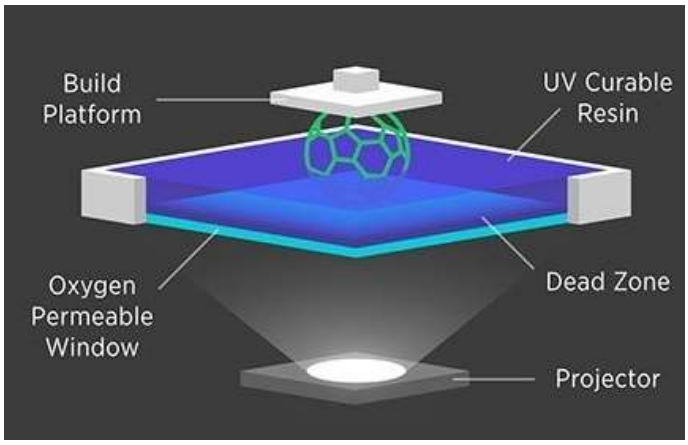

Figure 2.17 The Setup of CDLP Production Method [36]

- **Material Extrusion (Fused Deposition Modelling - FDM)**

The patent for this technology expired in the late 1980s. Since it became open source in 1990, this production method has developed rapidly. In this method, a thermoplastic continuous filament is used as the basic material in 3D printing, with ABS (Acrylonitrile Butadiene Styrene), carbon fiber, and PLA (PolyLactic Acid) based filaments being the most common choices.

In this process, the filaments from a coil are transferred by a moving heated printer extruder head, which is commonly referred to as an extruder. The nozzle of the extruder pushes the molten material out, where it is initially placed onto a heated 3D printing platform for extra adhesion. The yarn solidification process is carried out in the X-Y plane before the nozzle exit.

The main problems with the material extrusion method are dimensional precision issues and a slower printing speed compared to other production methods. The printed material also behaves quite anisotropically. However, the mechanical, chemical, and thermal characteristics of the printed material are adequate for a wide range of applications, making it the most affordable option for non-industrial applications. At Figure 2.18 illustrates the Fused Deposition Method (FDM).

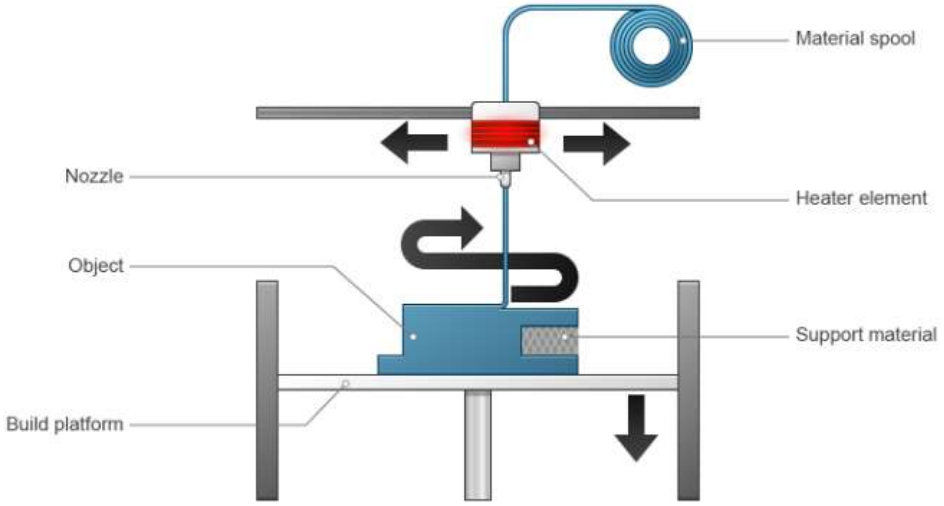

Figure 2.18 The Setup of FDM Production Method [33]

- **Powder Bed Fusion**

The idea behind powder bed fusion technologies is to heat and melt powdered materials to fuse them together by utilizing a power source like a laser, infrared light, or electron beam. This process needs a controlled environment, such as a vacuum or inert gas atmosphere. With the help of a controlled environment, it is easier for powder particles to fuse, less power is used, and the strength properties of the final product are enhanced. Both plastic and metal items are utilized using the powder bed fusion process. Actually, a variety of powders can be employed in the powder bed fusion process. The following paragraph describes some of the metals and polymers that can be used in the PBF process.

- Titanium, cobalt chrome, stainless steel, aluminum and copper (381 x 330 x 457 mm) are commonly utilized in EBM (Electron Beam Melting)
- Nylon is typically used in SLS (Selective Laser Sintering)
- Stainless Steel, titanium, aluminum, cobalt chrome (500 x 280 x 365mm) are preferred for DMLS/SLM (direct metal laser sintering) method.

In the literature, 4 different powder bed fusion methods are mentioned for additive manufacturing production.

These are classifed as selective laser sintering (SLS) , selective laser melting (SLM), electron beam melting (EBM) and multi jet fusion as basically.

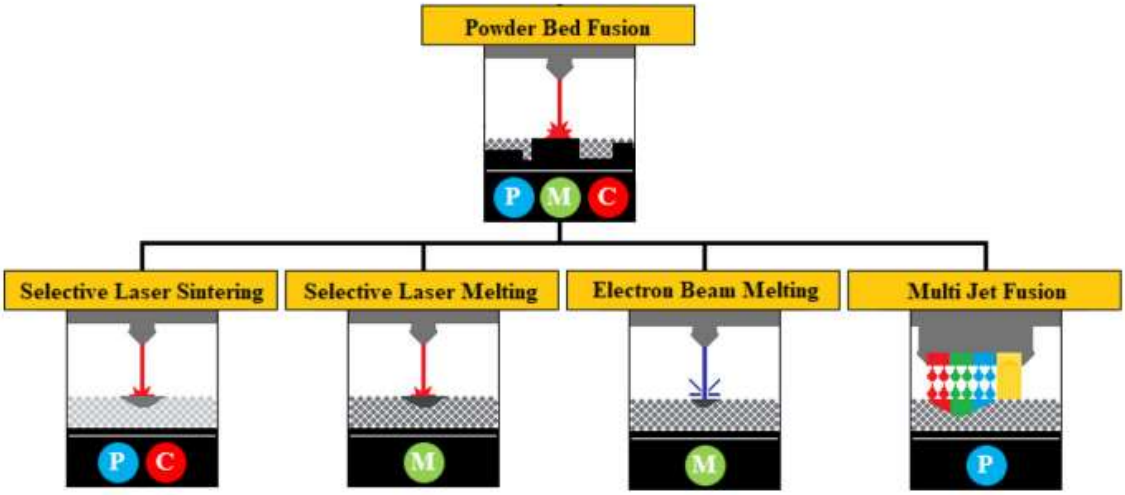

Figure 2.19 Tree diagram of Powder Bed Fusion Method , where (C) ceramic, (M) metal, (P) polymer material

In the SLS method , the temperature is raised just below the melting point of the polymer. The production platform is covered with a thin layer of powder by the re-coating blade. Afterwards, a CO2 laser scans the area of the subsequent layer and sinters or bond with the polymer powder granules. After a layer is produced, the build platform descends and the blade paints the surface once more. After then, the procedure continues until the entire part is accomplished. The setup of SLS production method is shown as Figure 2.20.

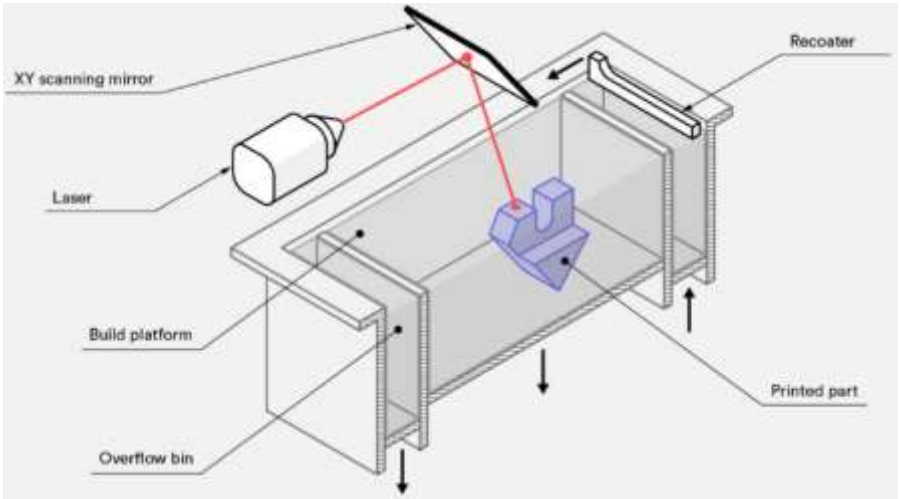

Figure 2.20 The Setup of SLS Production Method [37]

The absence of support structures is a major benefit of SLS method. The component receives all required support from the unsinterred powder. Therefore, SLS can be used to produce free-form shapes that are not possible to produce using any other technique.

Parts produced via SLS method, have superior tensile strength and modulus that are comparable to the casting material. There is no need to make sanding after the process.

On the other hand, SLS products are more brittle , elongation value at rupture is relatively lesser rather than other methods [37].

Unlike SLS method, in SLM method generates more concentrated parts since metals completely dissolves all of its constituent parts. Selective laser melting (SLM) is a novel manufacturing process that emerged in the late 1980s and 1990s. In this process, three-dimensional (3D) objects are fabricated by layer-by-layer melting of metallic powder or wire with an energy source. Parts with high density are obtained by melting the powders laid on the powder bed in a pre-determined scanning direction. The molten powder swiftly cools and solidifies, causing the material to take the form of the finished good. Due to the rapid cooling rate in the SLM method, the parts produced have a fine microstructure, which results in superior mechanical properties. The Setup of SLM Production Method is illustrated in Figure 2.21 as below.

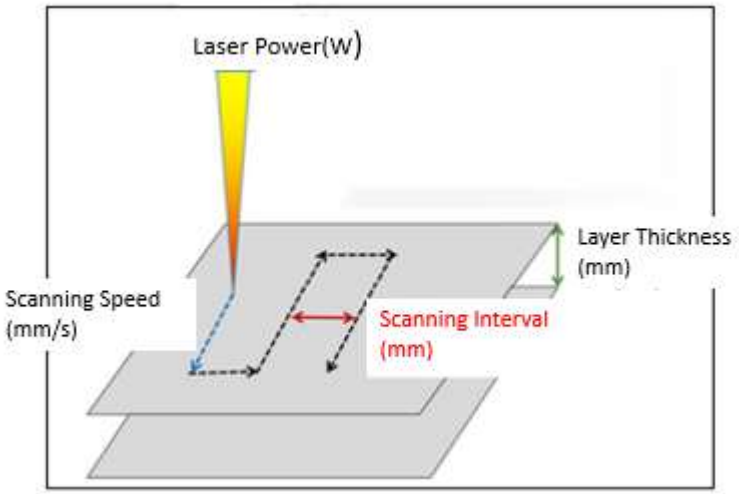

Figure 2.21 The Setup of SLM Production Method

Another essential issue is that the input parameters have a significant impact on the quality of the finished output when using the SLM process. Input parameters such as laser power, scanning speed, scanning interval, layer thickness, scanning pattern, and building direction can affect the quality of the finished product. Below, a list of overall process parameters used in the SLM method is given.

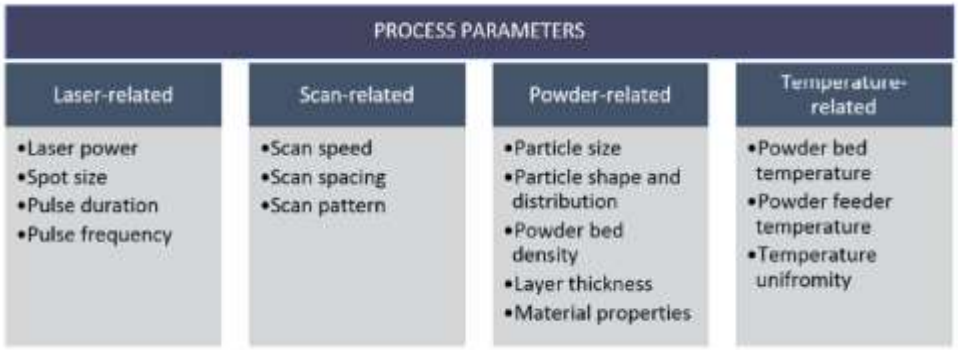

Figure 2.22 Process Parameter of SLM Method

The effects of process parameters on the SLM method can be seen in equation 1.

$$E = \frac{P}{v.h.t} \tag{1}$$

Where , E denotes energy density (J/mm3), P is the laser power (W), v is the scanning speed (mm/s), h is the scanning range (mm) and t is the layer thickness (mm) respectively. The equation states that the energy density of the process will rise if the laser power are increased or scanning speed,range,layer thickness are reduced. Actually, there is an optimum energy density value in the SLM process and this value varies depending on the powder alloy used and the machine tool.

This thesis aims to apply the Selective Laser Melting (SLM) method to specimens, while taking into account all parameters that could affect the test results. In order to successfully apply SLM to parts, it is essential to consider the energy required to melt powder particles, as the amount of energy is critical to achieving full melting of the powders without causing partial melting and formation of defects. Likewise, scan speed has a significant impact on defects, especially for porosity. Increasing the scanning speed helps to eliminate a metallurgical type of porosity, which is the formation of small, spherical hydrogen gases trapped in the melt pool. Nevertheless, when the scanning speed is increased, instability may appear due to rapid cooling. Moreover, it may also cause the formation of balling defects, indicating poor wetting between the melt pool and solidified substrate. However, the formation of balling defects is not only caused by an increased scan speed but also an increase in hatch space, which is the distance between layers or tracks. A decrease in space provides denser components, while the formation of balling defects would be more likely if the space is increased.

Figure 2.23 shows the relationship between the density and hatch space of AlSi10Mg alloy [49].

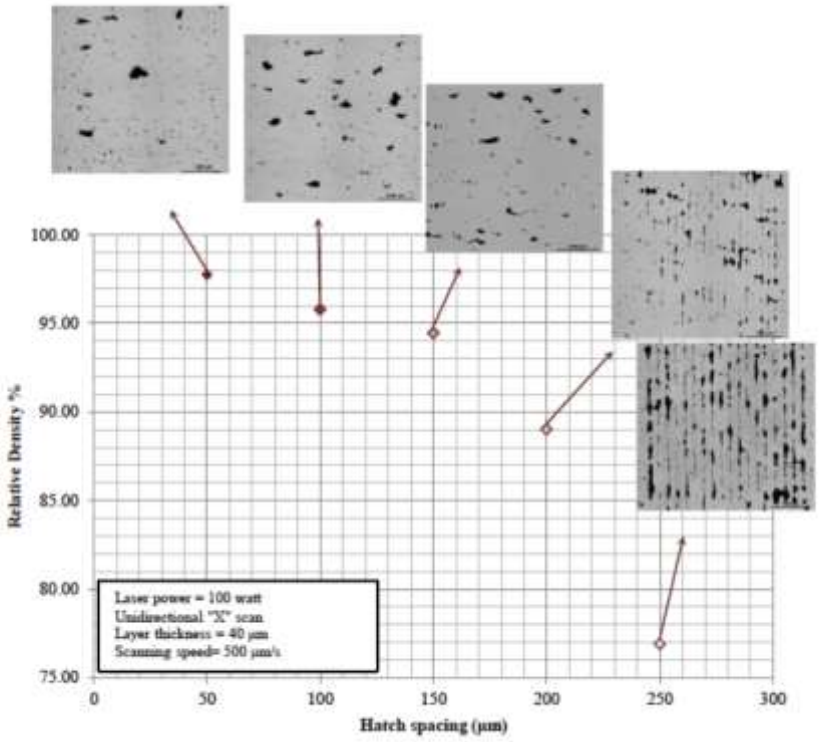

Figure 2.23 ALSi10Mg Density vs. Hatch Space [49]

When it comes to material selection for SLM, the most commonly utilized lightweight alloy types are aluminum and aluminum-silicon alloys. Nowadays, AlSi10Mg material is the subject of many researches. Figure 2.24 shows the distribution of research according to the years.

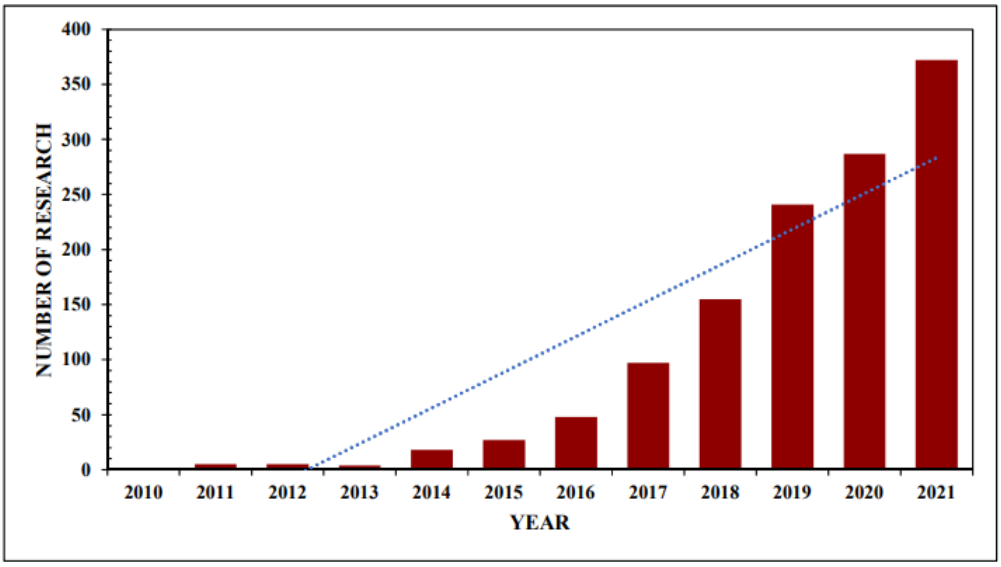

Figure 2.24 Amount of Researches Done on SLM Of Alsi10mg Alloy with the Passage of the Years [51]

The electron beam melting method is another powder bed fusion method that was invented to melt and create 3D structures from electrically conductive powder using an electric beam. Layers of powdered metal are melted by an electron beam, which generates a stream of electrons that are directed by a magnetic field to create an object that precisely matches the requirements specified by a CAD model. A vacuum chamber is utilized during production to prevent oxidation, which could pose a risk for highly oxidizable materials. Selective Laser Melting (SLM) and Electron Beam Melting (EBM) both operate on a powder bed to create objects, but SLM uses a laser while EBM utilizes an electron beam. EBM generates more durable products that maximize the unique abilities of the metals used in the process, by removing impurities that could form when casting metals or utilizing other manufacturing techniques. Despite the fact that EBM has a distinct advantage in terms of speed over other production methods, other powder bed methods such as SLM (Selective Laser Melting) create smoother and more precise parts. Besides, due to the exclusive nature of electron beam melting technology, specialized personnel are required to operate EBM printers and they are used exclusively with selected metals such as titanium and chromium-cobalt.

The last powder bed fusion type is the multi-jet fusion which is used to produce a small array of components as a cost-effective alternative to injection molding. The powder bed is initially heated evenly, and polyamide powder material of the type PA12 is laid layer by layer from the hopper to the bed.

- **Binder Jetting**

This technology was developed at the Massachusetts Institute of Technology in 1993[38]. The binder jetting method utilizes two ingredients: a powder-based material and a binder. Between the layers of powder, the binder performs as an adhesive. The based material is often in powder form, while the binder is typically in liquid form.

The powder is evenly spread in the build chamber, and a nozzle sprays a sticky material to bind the powder particles together. The object is produced where the powder is bonded to the liquid. One disadvantage of this production method is that it cannot be used with all materials. Additionally, the use of binding materials and post-processing significantly increases the production time. Figure 2.25 shows the equipment used for the binder spray manufacturing process.

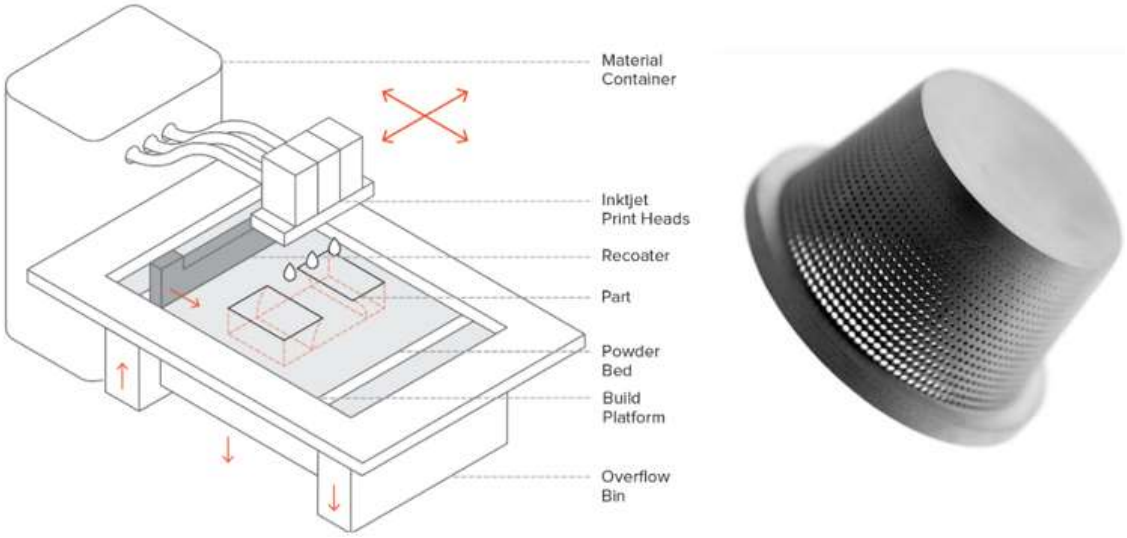

Figure 2.25 The Setup of Binder Jetting Production Method [38]

- **Material Jetting**

In this method, shapes are formed by spraying and curing liquid with ink printer-like moving heads. The biggest advantage of this method is that sensitive and shiny surfaces are is easily obtainable; however, it is a relatively fragile and time-consuming fabrication method. Figure 2.26 shows a product which is produced via material jetting method.

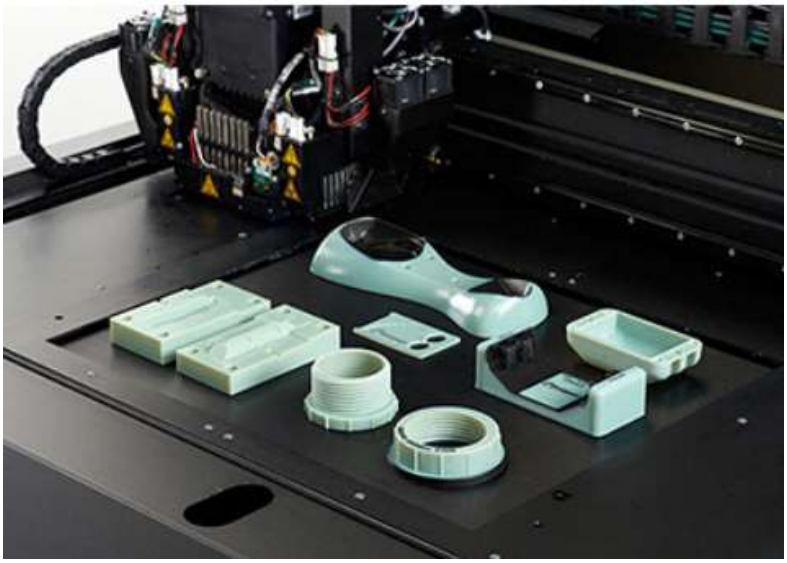

Figure 2.26 A Part Produced by Material Jetting Method

- **Sheet Lamination**

Sheet lamination refers to a type of additive manufacturing process that involves bonding thin layers of material together to create a 3D part, typically by using a feed roller system. There are several materials that can be used for sheet lamination, including paper, polymer, and metal. However, each of them requires a different technique to join the sheets of material together. Generally, paper sheets and certain polymers are held together by applying pressure and heat to an already-applied coating of active glue, whereas metal sheets are joined together by ultrasonic vibrations applied under pressure [39].

- **Directed Energy Deposition**

Directed energy deposition is a commonly preferred additive manufacturing method due to its capacity to alter the grain structure to a significant degree. A laser, electron beam, or plasma arc can be used as a heat source. This production method utilizes a raw material feeder and energy source mounted on a robot arm. Desired parts are produced by melting the raw material and depositing the molten material onto the substrate. The directed energy deposition method is commonly utilized in industrial applications such as the repair of damaged turbine blades and propellers. However, it is also possible to produce parts by starting with this method. In comparison to other metal additive manufacturing techniques such as selective laser melting (SLM) and

selective laser sintering (SLS), directed energy deposition can produce larger and more efficient parts. Nonetheless, it is not feasible to generate intricate geometries like lattice structures using this method. Consequently, this method is favored for producing coarse geometries where high resolution is not necessary. Figure 2.27 illustrates the application of direct energy deposition, which employs laser and electron beams as heat sources.

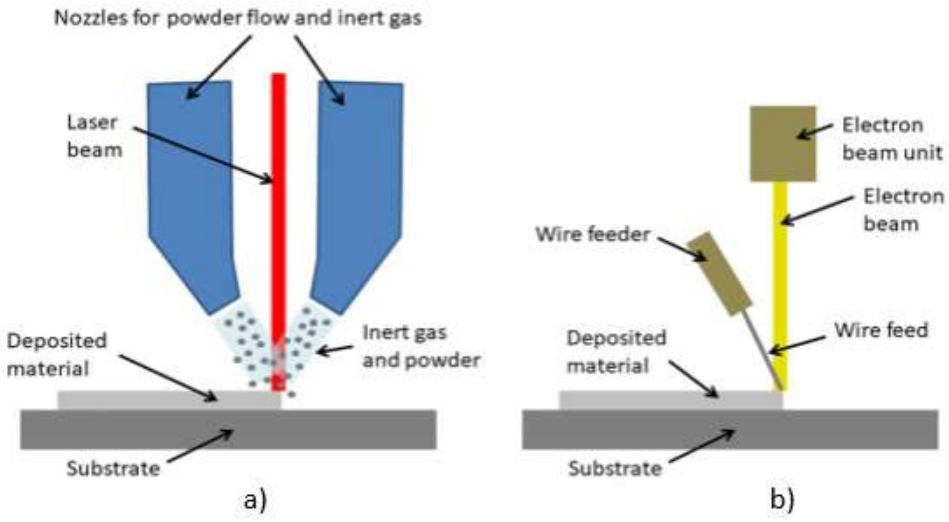

Figure 2.27 Schematics of Two DED Systems a)Uses Laser Together with Powder Feedstock and b)Uses Electron Beam and Wire Feedstock [40]

2.1.2 Material Technologies

Aluminum alloys are commonly used in most additive manufacturing applications due to their low densities, high specific strengths, corrosion resistance and perfect mechanical properties. As the demand for aluminum alloys is very high in aerospace applications, most manufacturers prefer to choose aluminum alloys to produce their components. In the past, manufacturing techniques for aluminum alloys were made with conventional methods such as turning, cutting, and machining. In addition to the conventional machining processes, aluminum and silicon alloys are widely employed in the form of casting application. After the implementation of additive manufacturing, aluminum alloys have become a very popular material. Among aluminum alloys, AlSi10Mg alloys are commonly preferred for the SLM method since their mechanical properties after fabrication are very similar to 6061 T6 alloy [51]. Despite the advantages, there are also several disadvantages of aluminum alloys produced with the SLM method.

Aluminum alloys are naturally lightweight, but poor flowability is one of their significant drawbacks. Achieving a uniform layer thickness during the deposition of aluminum powders requires flowability of the melt as successive powder layers are added. Additionally, high thermal conductivity and reflectivity are other challenges for Aluminum alloys. The increase on thermal conductivity and reflectivity causes to get higher laser power to avoid poor absorption and rapid heat dissipation. Also, high oxygen affinity of aluminum alloys makes it prone to porosity formation.

When reviewing Table 2.2, it can be observed that aluminum alloys have a very high thermal conductivity compared to other materials that are considered for SLM, according to reference [52].

Table 2.2 Thermal Diffusivity versus Thermal Conductivity [52]

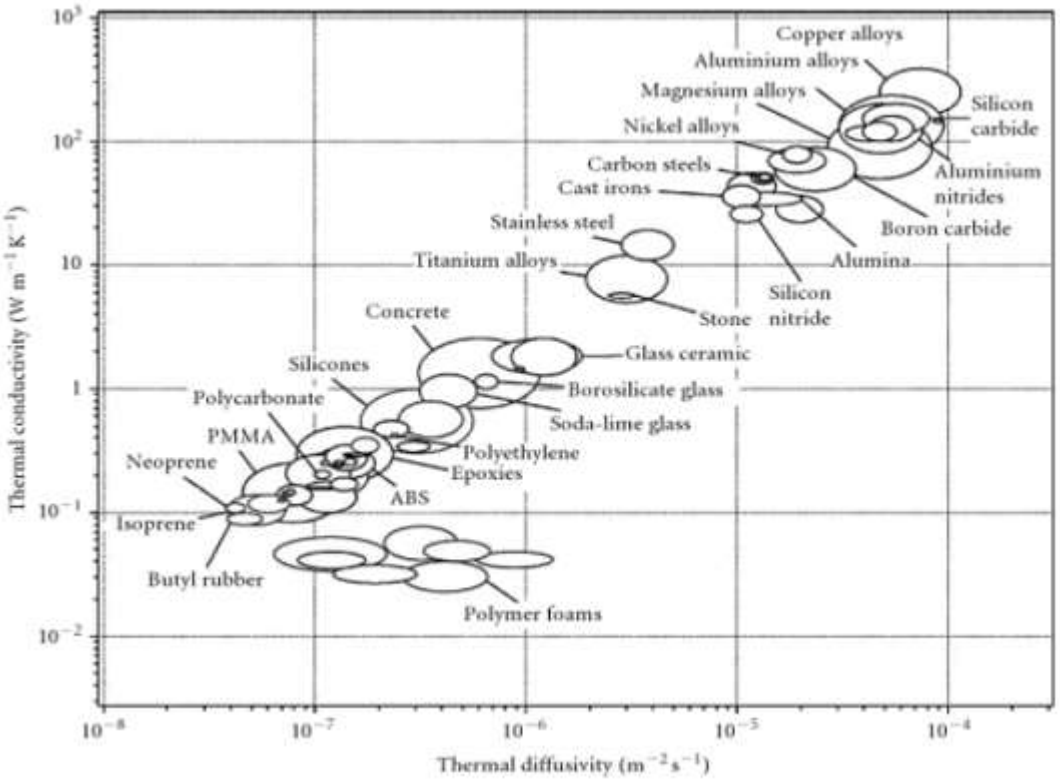

Many researchers have concluded that, despite the drawbacks, aluminum alloys can be effectively utilized in the SLM method [29]. The addition of silicon has been found to increase the flowability of the alloy and reduce its melting point. When silicon is added up to the eutectic composition, it provides excellent casting and welding properties [40]. The phase diagram of the aluminum and silicon alloy is shown in Figure 2.28. Furthermore, the addition of magnesium to the alloy can enhance its strength through solid solution strengthening and increased strain hardening ability. The formation of

Mg2Si provides additional strengthening and yields a heat-treatable alloy. Consequently, Al-Si-Mg alloy provides the best combination of strength, fatigue behavior, and elongation. The metal powder of AlSi10Mg is comparatively easy to process due to the small difference between its solidus and liquidus temperatures [49].

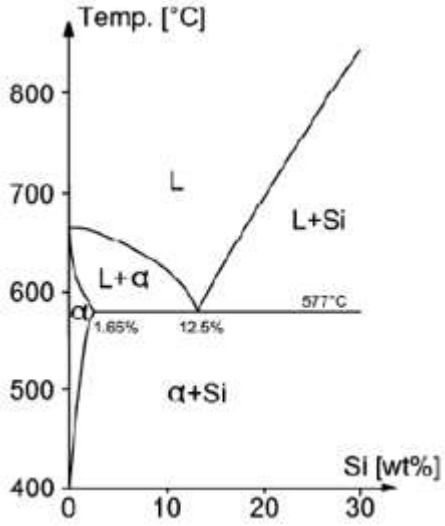

Figure 2.28 Aluminum – Silicon Alloy Phase Diagram [40]

Aboulkhair has pointed out that research is limited to alloy types that are currently in use for industrial applications, and there is still a lack of information on the development of alloys based on the SLM working principle. Currently, the decision to use alloys is based on their castability and weldability due to the similarity of those processes with SLM. Rapid solidification using the SLM method is one of the research topics [41]. For instance, Paul Rometsch and his colleagues are studying the strengthening mechanism of Scandium (Sc) and have found that during rapid cooling, Sc trapped in the solution can easily form precipitates with aluminum alloys with the help of heat treatment [42].

In this thesis, a mechanical and metallurgical characterization of AlSi10Mg will be conducted, along with topology optimization analyses. The objective of the study is to obtain a lightweight design with superior mechanical properties compared to the conventional 6061 T6 alloy, while reducing the manufacturing time.

2.2 STRUCTURAL OPTIMIZATION

Finding the "optimal" structure that is both lightest in weight and strongest is a common structural optimization challenge. A structure can be optimized using a broad range of methods or algorithms.

While first order optimization algorithms use only the gradient method, second order optimization algorithms use the Hessian matrix such as Newton's method.

Gradient-based optimization utilizes an algorithm to solve problems of the form:

$$\min_{x \in R^n} f(x) \tag{2}$$

The function f(x) is commonly referred to as the objective function or criterion in optimization problems. This optimization algorithm is based on an iterative process referred to as the local approximation, and each optimization step only leads to minor modifications in the design. Gradient-based approaches rely on the sensitivity of the system's response to changes in design variables to evaluate the impact of design modifications and improve the system.

In this thesis, the Hypermesh Optistruct module was utilized. The optimization process in the Hypermesh Optistruct program mainly involves three types of criteria methods.

These are as follows:

- The optimality method,
- A dual method and
- A primal feasible direction method.

The optimality criteria method is commonly used for traditional topology optimization formulations that involve minimum compliance (reciprocal frequency, weighted compliance, weighted reciprocal frequency with a mass (volume) or mass (volume) fraction constraint). Depending on the number of constraints and design variables, either binary or primary approaches are employed. When there are more design variables than constraints, the dual technique is preferred as in topology and topography optimization. In the opposite situation, the primal technique is applied, as in size and shape optimizations. However, the program autonomously determines which technique to employ.

2.2.1 Types of Structural Optimization

In the early stages of the design process size, shape, topography and topology optimization are used to forecast an ideal component design to satisfy strength and endurance requirements on a component level. By optimizing this process, the time lost with iterative design revisions is prevented, and the costs associated with design development are decreased. That is, in order to tackle with various structural design problems, optimization types could be used.

- **Size Optimization**

The objective of a typical sizing optimization is to determine the ideal member regions in a structural element or the ideal thickness distribution of a linearly elastic solid without altering the outer boundary of the part. Changing the thickness distribution can lead to alterations in physical parameters such as mean compliance (external work), maximum stress, and deflection. Specifically, an optimal thickness distribution can reduce or increase these values [9].

With size optimization, the ideal combination of some factors like cross-sectional area, material selection, shell thickness, composite ply thickness, length, the moment of inertia and thickness in frames are explored and optimized until the desired performance is attained. In designing the structure, the thickness is considered as the design variable. The state variable, on the other hand, may be chosen based on its deflection.

Figure 2.29 - b illustrates the ideal thickness value of each part as determined by applying the size optimization technique over three iterations. The corresponding stress results are represented in Figure 2.29 - c. Furthermore, it is also seen that the maximum stress value

decreased significantly from 319 Mpa to 220 Mpa by changing the thickness of tube from 3 to 2.2 mm.

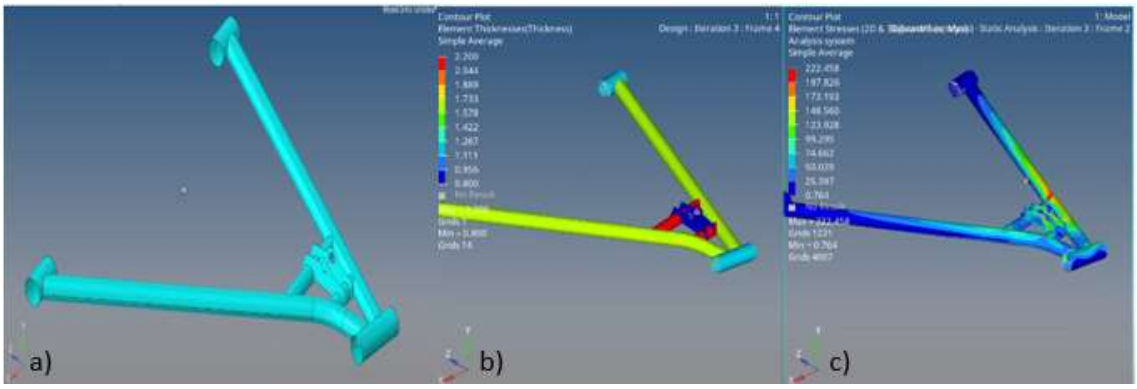

Figure 2.29 Size Optimization Demonstration [23]

a)Initial Model b) The Result of İdeal Thickness Values According to Size Optimization c) The Result of Element Stress Values According to Size Optimization

- **Shape Optimization**

In shape optimization, a structure's ideal outer geometry and hole geometry are found by using finite element models. By managing the part's boundaries (height, length, or radius of the design), the shape of the structure can be improved. The main goal of shape optimization is to decrease stress in some local regions. Contrary to size optimization, complicated edge geometries, holes, and surfaces are also possible to optimize.

On a representative part geometry which is illustrated at Figure 2.30 stress concentration values have been mitigated through the use of shape optimization applied to the part's holes.

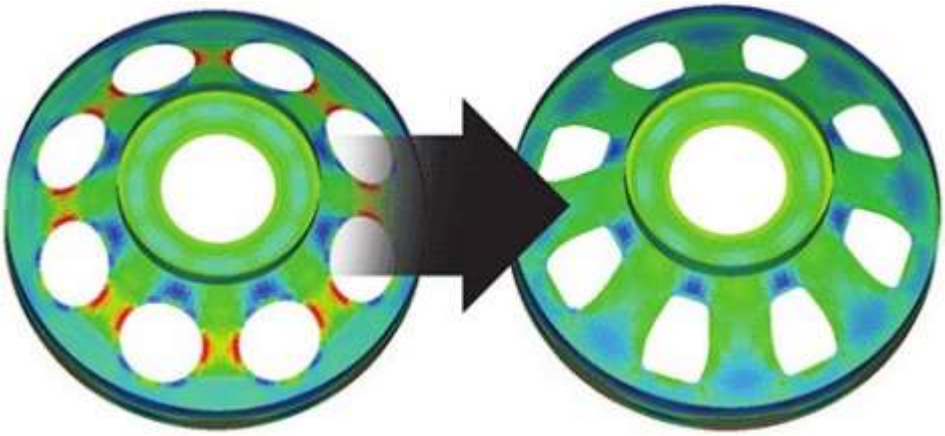

Figure 2.30 Optimized Hole Geometries with Shape Optimization [24]

- **Topography Optimization**

The difference between topography optimization other than size and shape optimization is that only shell structures can be applied. For sheet metal parts, this optimization type is particularly convenient. To enhance structural performance (rigidity and natural frequencies), stamped beads are utilized [22].

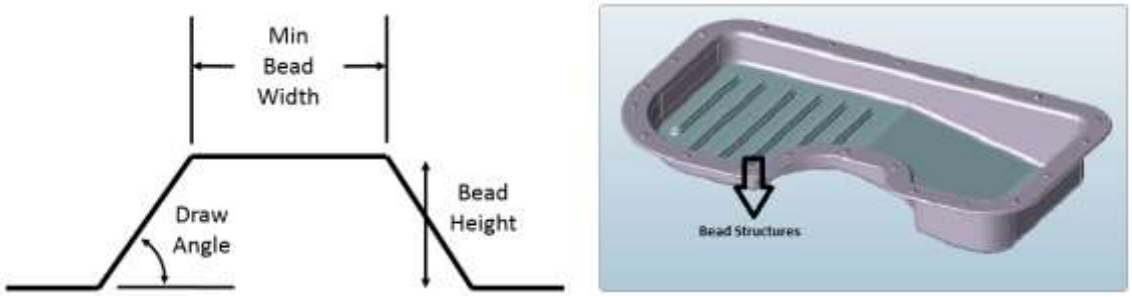

Figure 2.31 Stamped Bead Structures [22]

In the automotive sector, the vibration amplitude of resonated components tends to increase, causing noise and reducing the component's lifespan. Therefore, it is crucial to ensure that the vibration amplitude of sheet metal parts, such as fuel tanks and bonnets, does not conflict with the resonance value of the engine. Topography optimization is a potential solution to this problem that does not increase the weight of the component. Figure 2.32 depicts the topography optimization geometry of the fuel tank.

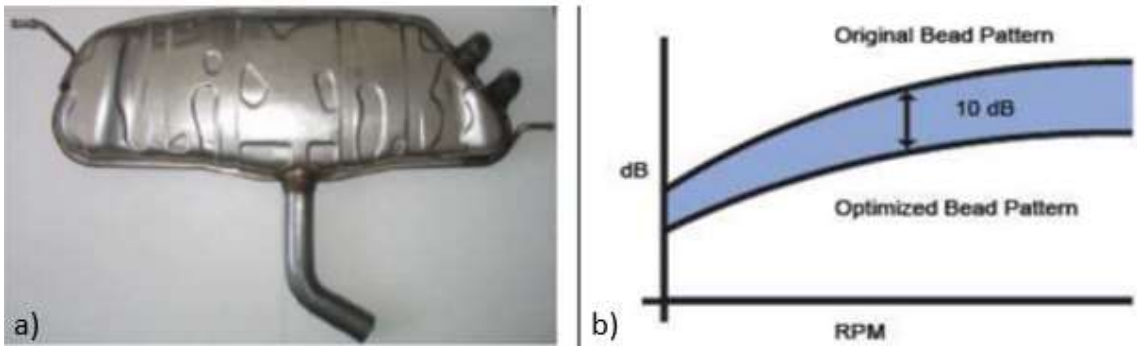

Figure 2.32 Topography Optimization Demonstration a)Optimized Fuel Tank Geometry b)Sound Emission-RPM Graph (-10Db Sound Emission) [24]

- **Topology Optimization**

Topology optimization is the most popular tool that determines the best material distribution in a design space with given a goal for the optimization and a set of restrictions, such as lowering weight while retaining stiffness requirements. The optimization eliminates unnecessary areas by identifying the region that can carry greater

strain energy to create a lighter part design.Topology optimization deals with issues such as determining the necessity of a bar or a component on a lattice system, the number of bars used in the lattice structure and the shape of their connections, as well as the number of holes in a continuous structure. Before advanced structural optimization techniques were employed, these issues were resolved by leveraging the experience and intuition of the designer.

Topology optimization is also a powerful structural design approach that considers both size and shape optimization simultaneously, making it a highly comprehensive method. Other approaches in the literature use similar methods, but differ in the decision criteria for removing or adding material. Figure 2.33 shows a basic part and a redesigned topology optimization model.

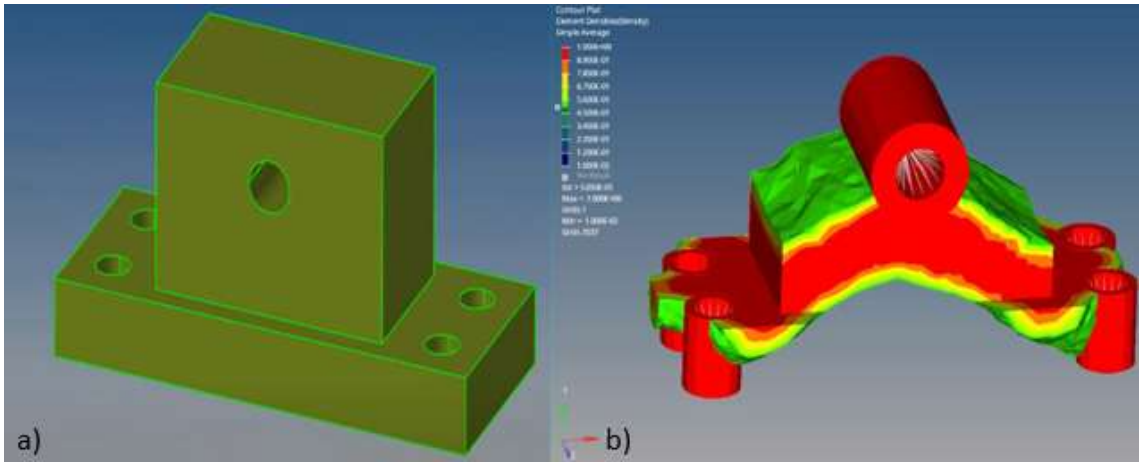

Figure 2.33 Topology Optimization Using Hypermesh Programme a)Initial Model b) The Result of Element Stress Values According to Topology Optimization [26]

Analytical solutions provide valuable insights into the fundamental characteristics of optimal designs. However, they are only applicable to problems that involve simple load and support conditions. In more realistic scenarios, discretized design domains are required. Finite element formulations with a fixed mesh are commonly employed as a discretization model in most studies reported in the literature.

The topology optimization problem for this model is presented in its general form as:

$$\text{minimize: } H(\boldsymbol{u}(\boldsymbol{x}), \boldsymbol{x})$$

$$\text{subject to: } Gj(\boldsymbol{u}(\boldsymbol{x})), \boldsymbol{x} \geq 0 \text{ for } j = 1, 2, \ldots . P$$

$$x_e = 0 \text{ or } 1 \text{ for } e = 1, 2, \ldots . .N \qquad (3)$$

In this context, the design variable vector is represented by x, while u denotes the state field. The objective function is H, and G_j is the jth constraint, with P being the total number of constraints. The design variable vector x comprises the structural members x_e, and the total number of design variables is denoted by N.

Equation (3) typically represents a nonlinear topology optimization .It's essential to keep in mind that design variables are limited to binary values of 0 or 1. This often results in topology optimization problems being ill-posed, meaning that they lack solutions. The other issue is to many design variables give rise to computational limitations in discrete formulations. To overcome these issues, the design variables can be defined as continuous, which allows the use of efficient gradient-based optimization algorithms. The continuous topology optimization problem can then be formulated as:

$$\text{Minimize or maximize: } H(\boldsymbol{u}(\boldsymbol{x}), \boldsymbol{x})$$

$$\text{subject to: } G_J(\boldsymbol{u}(\boldsymbol{x}), \boldsymbol{x}) \geq 0 \text{ for } j = 1, 2, \ldots, P$$

$$0 \leq x_e \leq 1 \text{ for } e = 1, 2, \ldots, N \qquad (4)$$

Springer [28] emphasizes that in order to accurately describe a structural optimization problem, it is substantial to forecast design variables, an objective function, and state variables.

- The term "Design Variable (x) " refers to a function or vector that represents the design and can be altered during optimization. This could stand for material selection or geometric design. When referring to geometry, it may be a complex shape interpolation, just the area of a bar or the thickness of a sheet. N denotes all of the design variables .The e_{th} is a structural part that to be formed from the design variable.

- The State Variable (u) is defined as the response of the structure, which refers to displacement, stress, strain, and force in the context of a mechanical structure. The state variables are dependent on the design variables u (x).

- Objective Function (H) signifies a goal that could either be decreased or increased. A common goal might be a structure's max stiffness or min volume.

- Constraint Function (G_j) is a requirement that must be fulfilled by the solution to an optimization problem. G_j are used to record or capture the model's response. Typically, these variables are used to describe the optimization problem's limitations. If restrictions

are ignored, the resulting design is not functional and feasible. P is defined as the total number of constraints. Maximum deflection, maximum stress could be given as examples of design constraint function [27].

- Sensitivity Analysis

Sensitivity analysis plays a crucial role by examining the impact of minor variations in the design variables on the optimization results. This analysis is essential to determine the optimal allocation of materials within the given design space while considering factors such as stress, displacement, or frequency. The sensitivity analysis cover the derivative of the objective function with respect to the design variables. The meaning of derivative is that gives details on how modifications to the design variables will impact the design's performance. During sensitivity analysis, elements weighted with low material density factors lose their structural importance and are eliminated in subsequent iterations. In the optimization process, iterations continue until the convergence criteria are reached.

In order to conduct sensitivity analysis, several numerical and analytical methods could be utilized such as the Finite Element Method (FEM), Boundary Element Method (BEM), or Meshless Method (MLM).

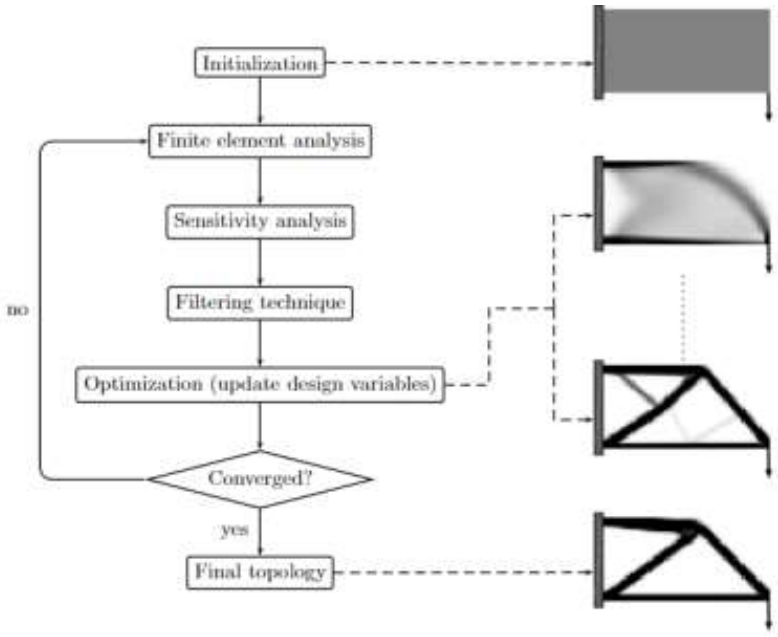

Figure 2.34 Shematic demonstration of all topology optimization steps [53]

2.2.2 Structural Optimization Methods

Various techniques exist to tackle with topology optimization problems, including the homogenization method, density method, and subtitles of density methods such as SIMP, RAMP, and Polynomial. In this chapter, detailed structural optimization methods have been explained.

1) Homogenization Method

Bendsøe and Kikuchi [54] developed the initial homogenization approach for the topology method, which subsequently gave rise to the development of other techniques. In optimization scenarios, it is not feasible to define every detail of a lattice texture in a finite element model. Homogenization theory is therefore the preferred approach for dealing with lattice materials and design issues. This theory assumes that material density has a microstructure similar to that of a composite material with numerous tiny voids [9]. The homogenization technique involves dividing the design volume into a limited number of microstructures with uniform material properties. The primary goal of this method is to simplify the challenging "layout" problem of material distribution into a much simpler "sizing" problem for density and other essential material properties that are achieved by creating small voids in the initial homogenous material [10, 20]. To find the structure with maximum stiffness or minimum compliance, this method uses the dimensions of the both square and rectangular microstructure and the orientation angle as variables which could be seen in the Figure 2.35. Lengths of the voids are assumed to the design variables and continuous. The variables actually determines how the microstructure is distributed when the homogenization method is applied. On the other hand, by using the numerical homogenization method, it is possible to obtain macroscopic constitutive properties of the unit cell like stiffness ,elasticity that are dependent on the hole's height (a1) , width (a2) and angle (Ɵ) parameters which are represented in Figure 2.35.

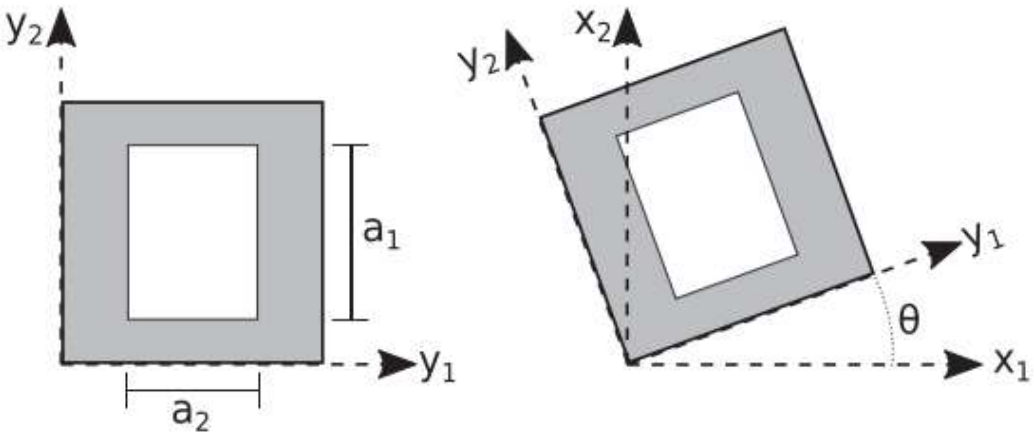

Figure 2.35 Input Parameters of Rectangular Hole Used for Homogenized Method [30]

For linear and relatively simple parts, it is easy to determine the elasticity of part; nevertheless, FEA techniques must be applied and an elasticity evaluation must be carried out for the majority of complicated structures. To give an accurate result, the FEA model should be used the height, width, and angle of a model by interpolating [9].

There are some drawbacks to the homogenization method. These are that it necessitates a larger number of design variables per element in comparison to the density method and optimized design through the homogenized method could have an intricate microstructure, making it challenging to manufacture in reality.

2) Density Method

The general definition of element density is that it is a continuous variable that is derived from a pseudo density variable, with values ranging from 0 to 1. Elements with a value of 1 represent 100% relative density, which are typically defined as solid black areas, as shown in Figure 2.36. Elements with a value of 0 represent areas with no density, resulting in void spaces in the design. Topology optimization results should ideally contain elements with pseudo-densities of 0 and 1, which are usually corresponded to as black and white areas, respectively [12]. In this topology optimization method, the design variable selected is only density. In a 2D component, the thickness of the plate can also be chosen as a design variable. However, predicting design variables in 3D investigations from a density perspective is challenging. Therefore, the entire component needs to be divided into solid or vacant regions, and a penalty is imposed on grey elements when their density value is between 0 and 1. The normalized density is constrained to be either 0 or 1. These penalty techniques between 0 and 1 will be discussed in the next section.

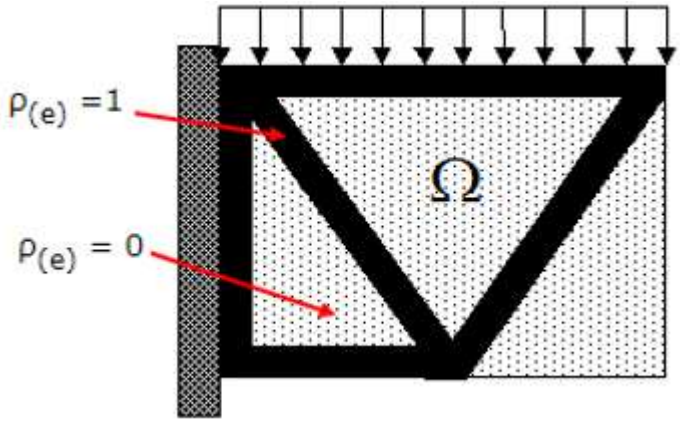

Figure 2.36 Application of Density Method for Topology Optimization

In summary, the differences between the homogenization and density method are that multiple variables are needed for the homogenization method and additional operations are performed for each element to solve the mathematical equations. This method is more suitable for complex microstructures. Therefore the structure of the problem gets more complicated. When it comes to the density method, the density of each finite element is considered a design variable and it is more convenient for designing structures with a uniform material distribution that is easier to fabricate.

There are several density approaches described in the literature. These are commonly known as SIMP, RAMP and Polynomial methods.

- SIMP (Solid Isotropic Material with Penalization)

The most popular mathematical solution method for topology optimization is claimed by Bendsoe ,Kikuchi (1988) and Rozvany, Zhou (1992). According to the SIMP approach, an exponential function of the element density is used to model the elastic properties of a microstructure. As the material relative density is capable of continuous variation, the Young's modulus of each element of the material can also vary continuously. In each element, the relationship between the material relative density factor ρ_e and the modulus of elasticity of the assigned isotropic material model E_0 is calculated according to the power law:

$$E(\rho_e) = \rho_e^p E_0 \quad (5)$$

Penalty factor (ρ), reduces the contribution of elements with intermediate configurations (gray elements) to the overall stiffness and this factor directs the optimization solution to focus on parts that are either invalid white ($\rho_e = \rho_{min}$) or solid black ($\rho_e = 1$)[32]. ρ_{min}

represent the minimum relative density value allowed for empty elements greater than zero and provides the numerical stability of the finite element analysis.

According to experiments conducted, the optimal penalty factor value of p = 3 for SIMP is appropriate as can be seen in Figure 2.37.

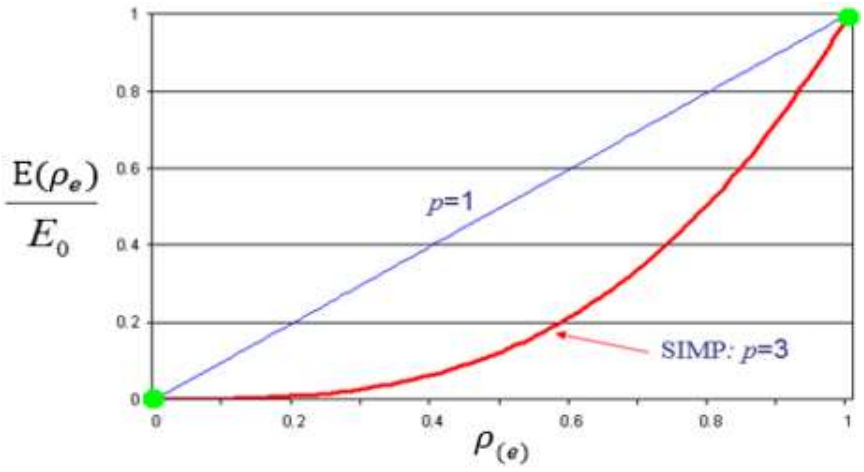

Figure 2.37 The Result of Numerical Experiments for Ideal Penalty Factor According to SIMP

A decrease in the modulus of elasticity of a material element results in a reduction in its stiffness. To regulate the global stiffness of a structure, the SIMP approach is commonly used, which involves adjusting the density of the material in the design domain. This approach penalizes the material properties as the density decreases and the stiffness of the structure is related to the penalized material modulus of elasticity. The following formula can be used to regulate the global stiffness of the structure: increasing the penalization of the material properties results in a stiffer structure, reducing the density of the material leads to a less stiff structure.

$$K_{SIMP(\rho)} = \sum_{e=1}^{N} [\rho_{min} + (1 - \rho_{min})\rho_e^p] K_e \quad (6)$$

Where, $K_{SIMP(\rho)}$ represent the penalized global stiffness matrix of an element, ρ_e is used for element relative density, N corresponding to a number of element in design area.

- RAMP (Rational Approximation of Material Properties)

RAMP interpolation method is preferable for dynamic issues due to concave of interpolation notation. Depending on whether the solution has static or dynamic substates, the software itself determines which interpolation strategy to use. By integrating the RAMP method with the Guide-Weight method, the number of design variables and

iterations can be reduced, resulting in quicker convergence and higher efficiency. This approach enhances the effectiveness of the method. The material interpolation approach known as RAMP (rational approximation of material properties) is described by:

$$E = E_0 \frac{\rho}{1+\rho(1-\rho)} \tag{7}$$

- Polynomial

Polynomial penalty is a method used in both continuous and discrete design variable formulations of topology optimization to enforce design constraints on the solution. This penalty term is used to define a polynomial function of the design variables.

In the context of topology optimization, the polynomial penalty method can be utilized to ensure that the optimized design variables such as lengths, and thickness remain inside the boundaries given. It is capable of managing various restrictions and is efficient in terms of computation. Thus, helps to steer the optimization toward feasible designs that satisfy the constraints.

3. PROBLEM DEFINITION AND ASSUMPTIONS

In the field of aerospace engineering, the primary objective is to design structures that have minimal weight to diminish emissions and carbon footprint. Furthermore, this optimal design impacts both fuel efficiency and the service life of parts. However, it may not be feasible to produce every optimal design using conventional manufacturing techniques. The advancement of additive manufacturing technology has enabled the fabrication of complicated structures while exhibiting superior mechanical properties through the application of topology optimization, size optimization and shape optimization.

In this thesis, a bracket which is located on a helicopter at the nose section has been selected to apply topology optimization in order to reduce weight and minimize compliance. All components have been made of 6061 T62 series Aluminum alloy and for some parts of the assembly, the welding process has been applied. While the upper part is supported with FLIR equipment, the lower part of the bracket is supported with a gun. To briefly mention their duties of equipment, Forward-looking infrared (FLIR) cameras are generally known as thermal imaging equipment and are located in the nose section of helicopters due to their missions. These cameras detect infrared radiation, which is usually released from a heat source (thermal radiation) to produce images. Another gun turret, commonly abbreviated as a "turret," is also a weapon positioning platform that offers shelter, observation, and the ability to swivel. Since working in harmony with one another is required, it is planned to be located in close proximity to each other.

Equipments and brackets have been illustrated in Figure 3.1. representative modelling has been made via the CATIA V5 program to simulate the 3D model of the FLIR and gun turret equipment.

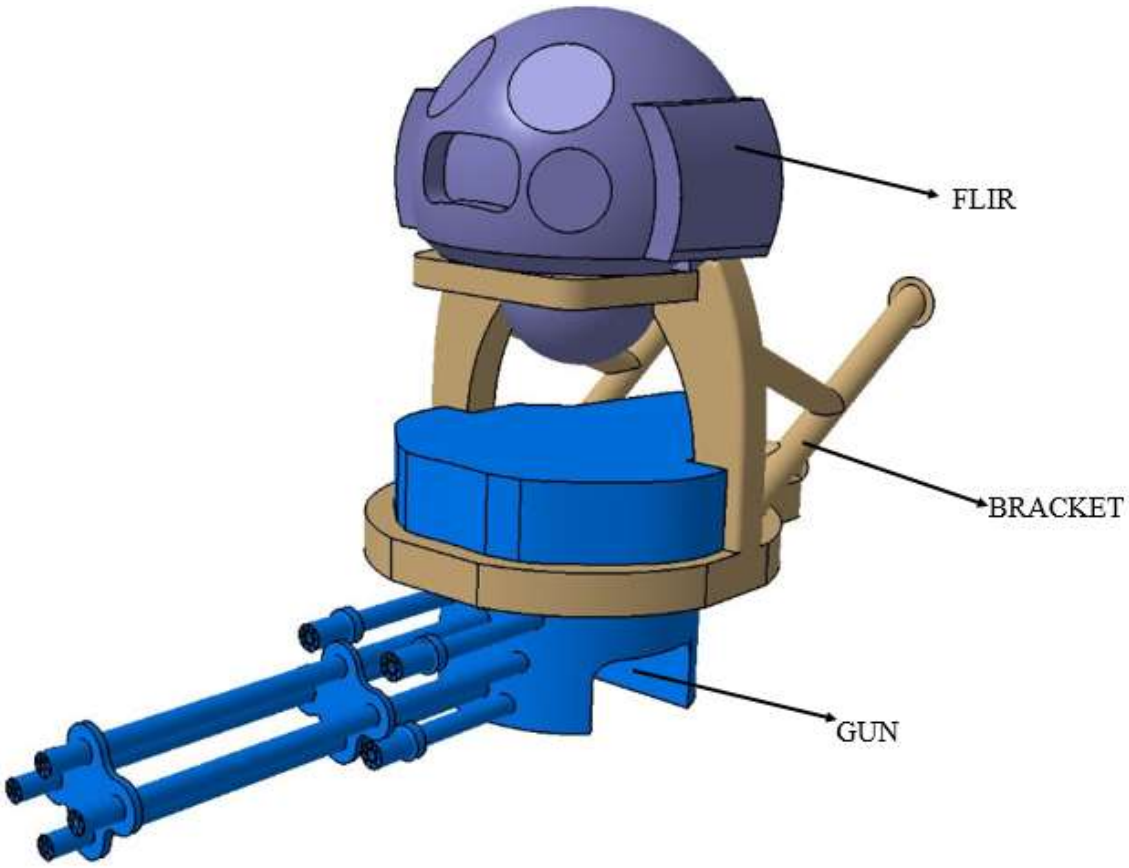

Figure 3.1 Modelling of FLIR,Gun Equipment and Bracket

Initially, the bracket model is designed as 6.04 kg and has composed of tubular part and machined part which are depicted in Figure 3.2. Due to the application of the welding process during the assembly phase, the need for improvement has been noticed. In some assembled parts have manufacturing problems(deformation, porosity, etc.) and access problems to tubes in assembly.

To handle these issues, an optimal design have been created. Firstly, static analysis and modal analysis have been performed to the initial model respectively. Secondly, by applying topology optimization, both weight reduction and a decrease in stress levels are intended to be achieved. Subsequently, modal analyses are conducted to ascertain the inherent frequencies and modal configurations of the bracket structure subjected to specific boundary conditions. Modal analyses have been implemented for each load step via Hypermesh EIGRL card.

On the other hand, this study involves repeating the aforementioned procedures with different materials and subsequently comparing the outcomes. For this purpose, AlSi10Mg, the prevailing Aluminum alloy utilized in additive manufacturing technology,

was selected due to its favorable machinability and cost-effectiveness in comparison to other metals. However, AlSi10Mg is an anisotropic material whose physical properties could change in different directions. To investigate the mechanical effects of different orientations, coupon tests were conducted. The results of the coupon test have been applied to topology optimization. Afterward, all results have been compared in terms of weight, stress level, stifness value and natural frequency.

3.1 Finite Element Analysis

The objective of performing static analysis on the bracket is to examine its capacity to endure all loads experienced during the initial phase. The bracket consists of tubular and machined parts which is illustrated in Figure 3.2. Besides, all parts are fixed to each other by welding process. The tubular parts have an outer diameter of 30 mm and a thickness of 3 mm.

In this thesis, the Hypermesh program was chosen for meshing since it is widely used in the aerospace and automotive industries as a Finite Element Analysis (FEA) tool and to solve Optistruct program has been preferred.

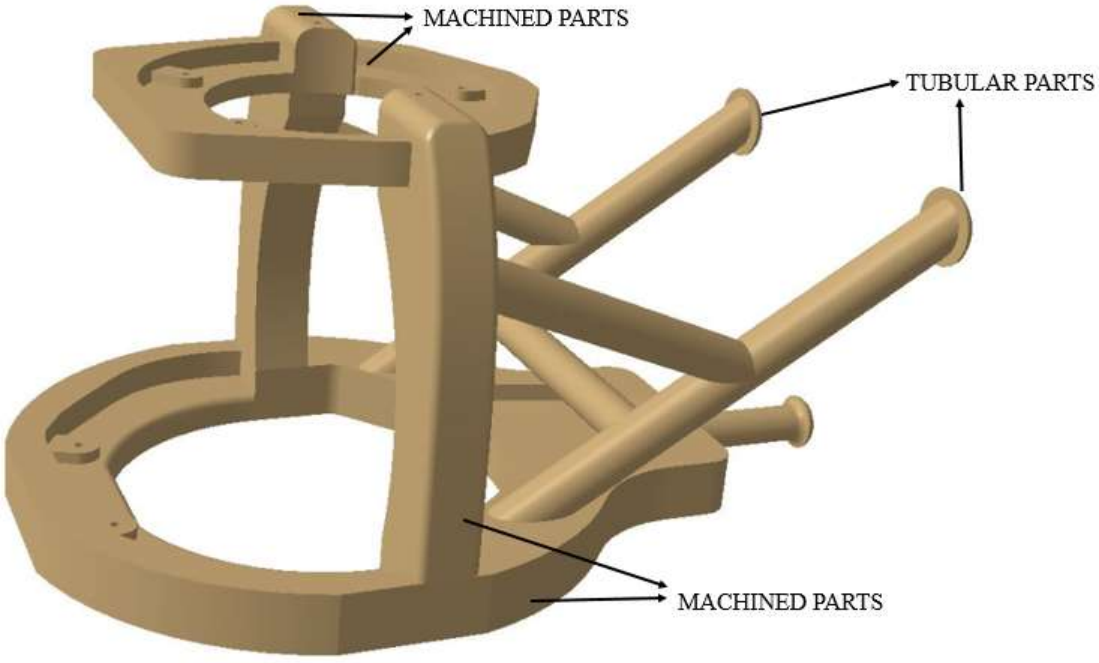

Figure 3.2 Subparts of Assembly

- Mass Data

Table 3.1 expresses the weight and center of gravity of the components located on the bracket at the nose section. The weight of FLIR equipment has been selected as 80 kg and gun weight has been assumed as 100 kg.

Table 3.1 CG Positions of Equipments

Item	Weight	X_m	Y_m	Z_m
------	[kg]	[mm]	[mm]	[mm]
FLIR Equipment	80	398.41	0	964.5
Gun Equipment	100	375.46	-25.14	345.46

- Material and Allowable Data

The mechanical properties of the materials used in the bracket design are clarified in this section. Table 3.2 should be taken into account for the 6061 T62 Plate, whereas Table 3.3 will be utilized for the 6061 T62 tubular part.

Table 3.2 Mechanical Properties of 6061 T62 Plate [55]

E	E_c	G	ϑ	ρ	F_{tu}	F_{ty}
68258 N/mm²	69637 N/mm²	-	0.33	2.71E-06 kg/mm³	289.7 N/mm²	241.4 N/mm²
9.9 X 10³ ksi	10.1 X 10³ ksi	3.8 X 10³ ksi	0.33	0.098 Ib/in³	42.00 ksi	35.00 ksi

Table 3.3 Mechanical Properties of 6061 T62 Tube [55]

E	E_c	G	ϑ	ρ	F_{tu}	F_{ty}
68258 N/mm²	69637 N/mm²	-	0.33	2.71E-06 kg/mm³	289.7 N/mm²	241.4 N/mm²
9.9 X 10³ ksi	10.1 X 10³ ksi	3.8 X 10³ ksi	0.33	0.098 Ib/in³	42.00 ksi	35.00 ksi

In these tables, E denotes Young Modulus, E_c Modulus of Elasticity , G Shear Modulus, ϑ Poisson's Ratio, ρ Density, F_{tu} Tension Allowable Stress , F_{ty} Tension Yield Stress respectively.

- Load Data

The next step is to apply loads and boundary conditions to the model, to simulate how the structure will respond under different scenarios. This section, involves specifying the amount and direction of loads applied to the structure, as well as constraints on its movement to helicopter fuselage section. Ground maneuver loads are considered and flight maneuver loads are neglected.

Table 3.4 Load Conditions for FLIR Equipment

α	β	P [Mpa]	Fx [N]	Fy [N]	Fz [N]	Mx [Nmm]	My [Nmm]	Mz [Nmm]
0	50	$2500X10^{-6}$	270	-650	450	$750X10^{3}$	$90X10^{3}$	$-340X10^{3}$
-50	0	$2500X10^{-6}$	250	640	450	$-720X10^{3}$	$50X10^{3}$	$320X10^{3}$
25	0	$4500X10^{-6}$	3	0	650	$15X10^{3}$	$-370X10^{3}$	$-6X10^{3}$
0	-25	$3500X10^{-6}$	300	50	120	$-60X10^{3}$	$270X10^{3}$	$25X10^{3}$

Table 3.5 Load Conditions for Gun Equipment

α	β	P [Mpa]	Fx [N]	Fy [N]	Fz [N]	Mx [Nmm]	My [Nmm]	Mz [Nmm]
0	-90	$500X10^{-6}$	2400	25	-80	$-49X10^{3}$	$-340X10^{3}$	$-90X10^{3}$
90	0	$1400X10^{-6}$	-40	-330	-260	$25X10^{3}$	$-25X10^{3}$	$70X10^{3}$
25	0	$1400X10^{-6}$	-320	200	350	$110X10^{3}$	$25X10^{3}$	$3X10^{3}$
0	-25	$4500X10^{-6}$	-320	-200	350	$110X10^{3}$	$-25X10^{3}$	$3X10^{3}$

According to Table 3.4 and Table 3.5, the most critical angles, 3 axial forces , 3 axial moments and pressure have been applied to the model.

For the analysis, firing conditions are not considered. Thus, the linear analysis method is used. Analysis under the effect of limit and ultimate loads are performed. Ultimate load conditions are obtained by multiplying by the safety factor. The load and boundary conditions applied on the modal are shown in Figure 3.3 as follows.

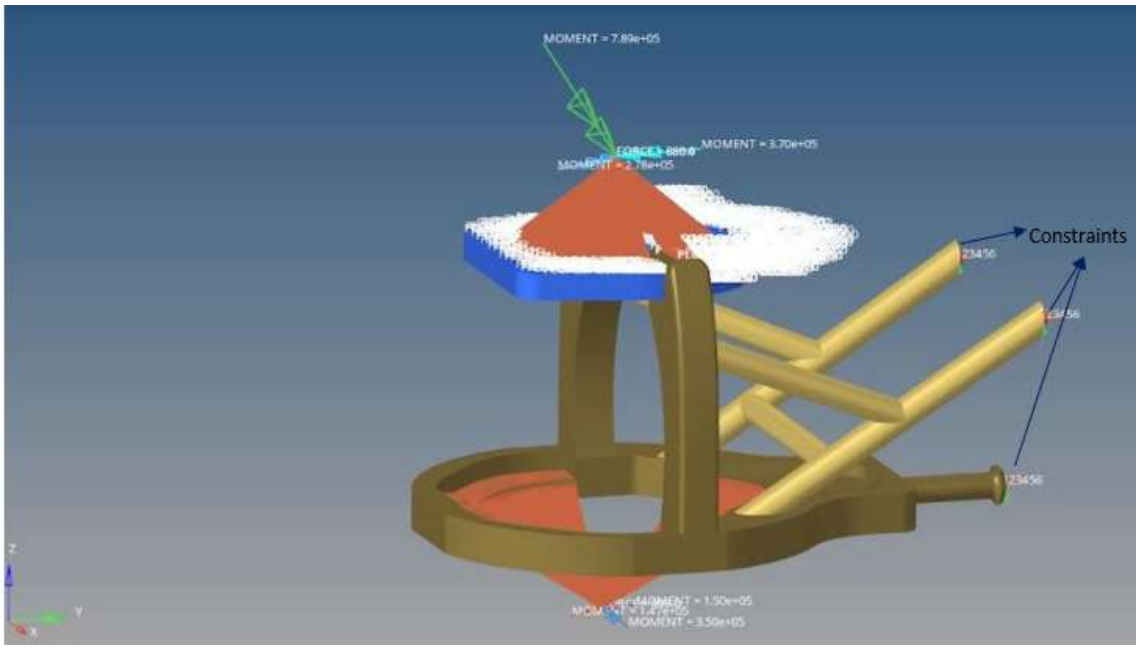

Figure 3.3 Notation of Loads and Boundary Conditions

- Mesh Definition and Mesh Size Refinement

The mesh convergence study aims to find the ideal element size by applying different mesh sizes to the model. Normally, smaller element sizes give more reasonable results. However, finite element analysis may take longer to apply and it gives similar outputs. In this section, static analysis was performed with the assumption of a 0.5 mm element size. Some areas on the bracket shown in Figure 3.4 were subjected to more stress than other areas on the bracket. As can be seen in Table 3.6, when the element size is decreased from approximately 2 mm to 0.25 mm, there is little change in the stress value and similar results are obtained in terms of stress level.

Therefore, as a result of the mesh convergence study, the mesh dimensions were determined as 0.5 mm.

Table 3.6 Change of Stress Level for Different Mesh Sizes

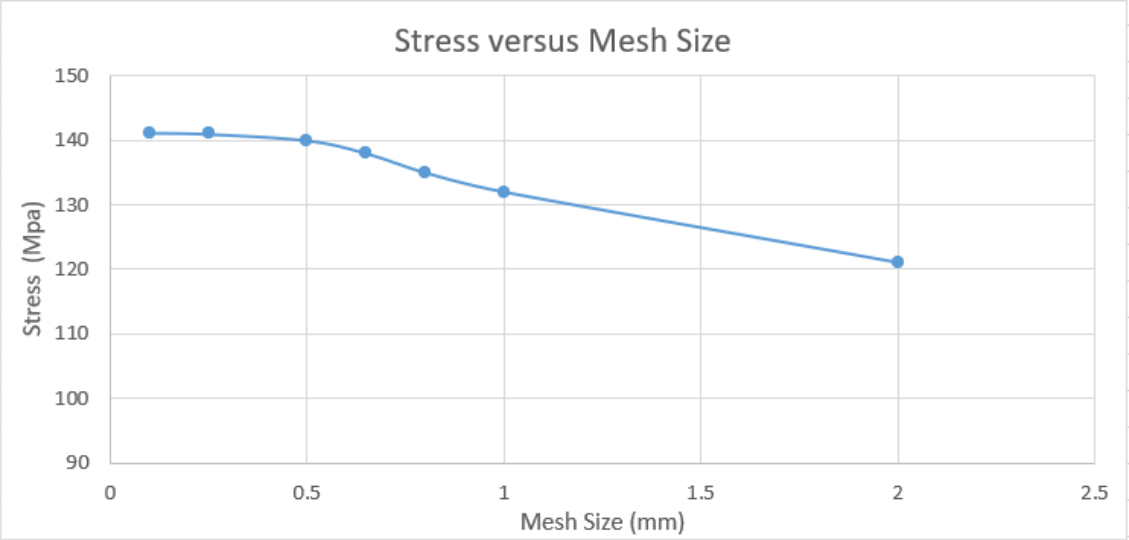

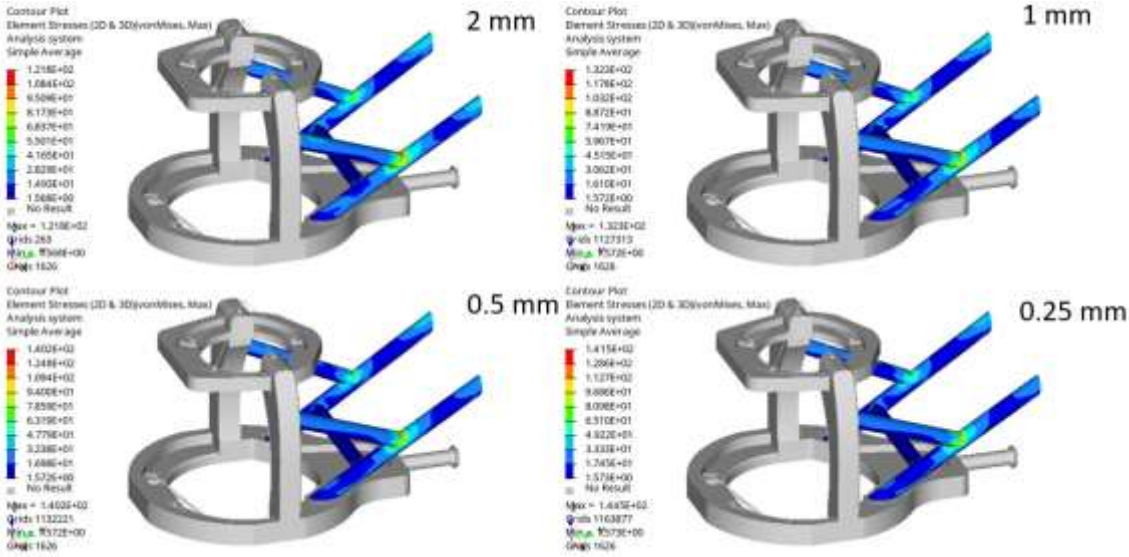

Figure 3.4 Mesh Convergence Study

- The Results of Finite Element Analyis

This section presents the outcomes of the static analysis conducted on the part subjected to the aforementioned force, moment, and pressure values. The analysis was carried out on Al 6061, the material utilized in the current configuration. Related Von-Misses stress and displacement values are provided in Figure 3.5 below.

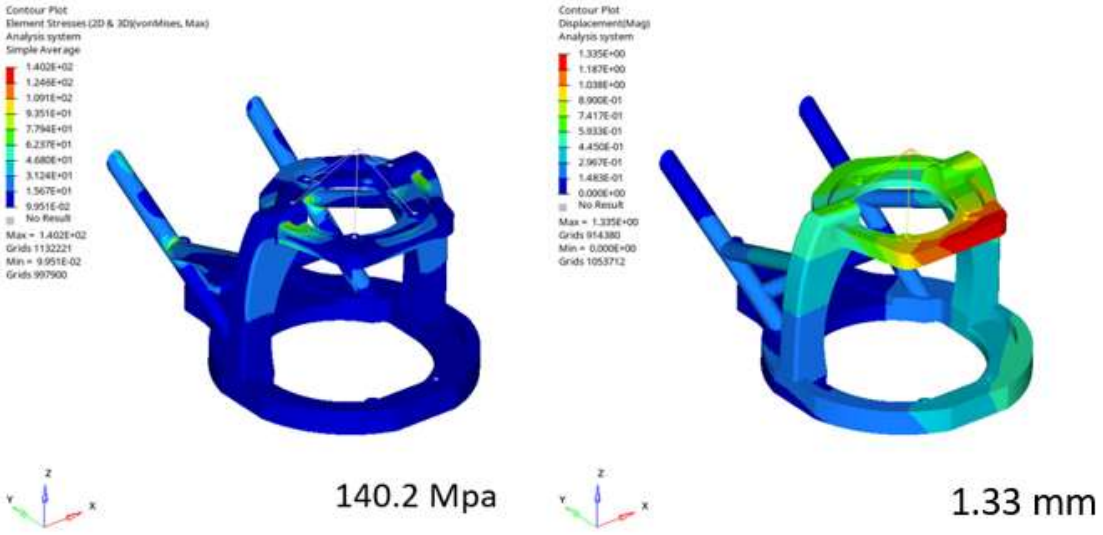

Figure 3.5 The results of Finite Element Analysis for Initial Model

a) Von-Misses Stress Level(Mpa) b) Displacement (mm)

Based on the finite element analysis results depicted in Figure 3.6 , the initial compliance value for the Al 6061 T62 material has been found as 1721 Nmm.

```
Volume                              =  2.22896E+06   Mass      =  6.04047E-03
-----------------------------------
Subcase    Compliance       Epsilon
-----------------------------------
      1  1.720964E+03  1.836612E-10
```

Figure 3.6 The Results of Finite Element Analysis

3.2 Modal Analysis

Modal analysis is utilized to specify the vibration characteristics of components. Dynamic characteristics of structural parts could be made more meaningful through modal analysis.

Natural frequency is sometimes referred to as the eigenfrequency at which a system typically oscillates in the lack of any driving force. Normal mode is the vibration pattern of a system operating at its natural frequency. When an external factor or excitation is applied to a system, a type of vibration known as forced vibration occurs. If a part is

disturbed by an external force at the natural frequency of the part, this energy accumulates over time and causes excessive oscillation which is called resonance.

In this thesis, the modal analysis will be performed via Hypermesh EIGRL control card. Using a finite element model, the normal modes of the initial model were calculated. The corresponding center of gravity is applied with the masses for the FLIR equipment and gun. The results of the calculation are given in Table 3.7 and Figure 3.7.

Table 3.7 The Results of Modal Analysis for Different Mode Shapes
(Al 6061 T62 Material)

Mode 1 - F = 6.121856E+01	Mode 11 - F = 1.053205E+03
Mode 2 - F = 1.936691E+02	Mode 12 - F = 1.174336E+03
Mode 3 - F = 2.926343E+02	Mode 13 - F = 1.367046E+03
Mode 4 - F = 3.875162E+02	Mode 14 - F = 1.600502E+03
Mode 5 - F = 4.783136E+02	Mode 15 - F = 1.641011E+03
Mode 6 - F = 4.917851E+02	Mode 16 - F = 1.749475E+03
Mode 7 - F = 5.100351E+02	Mode 17 - F = 1.781561E+03
Mode 8 - F = 7.389966E+02	Mode 18 - F = 1.962189E+03
Mode 9 - F = 8.126287E+02	Mode 19 - F = 2.019597E+03
Mode 10 - F = 8.806668E+02	Mode 20 - F = 2.129083E+03

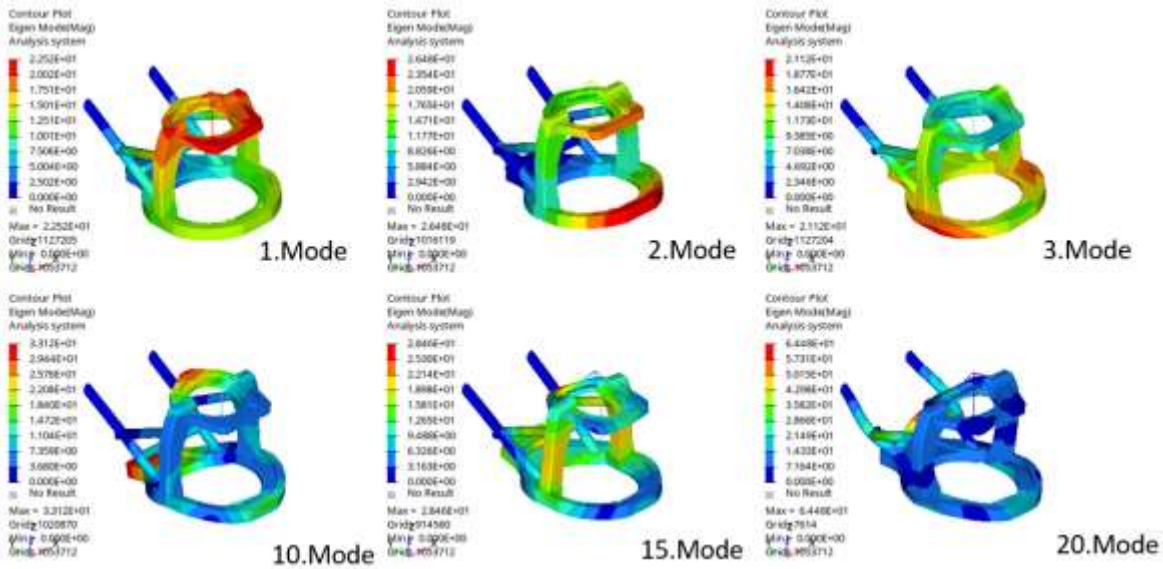

Figure 3.7 Natural Frequency Modes 1,2,3,10,15 and 20 for Initial Model
(Al 6061 T62 Material)

To prevent resonance, it must be ensured that the bracket modes do not fall into critical modes or modes ranges with the main rotor and blade transition frequencies in the helicopter. Table 3.8 shows the modal analysis results for the first model. When the bracket frequency and rotor were compared, it was concluded that the main rotor modes and blade did not overlap any range neither the helicopter rotor nor the gun.

Table 3.8 Representative Rotor System Induced Frequencies on Helicopter

Forcing	Range	Range
-	F_{min} [Hz]	F_{max} [Hz]
1 x Revolution	10.7	15.6
5 x Revolution	53.5	78
10 x Revolution	117	156
15 x Revolution	160.5	212

4. PART OPTIMIZATION AND VERIFICATION

In this thesis, a series of optimization techniques listed in sequentially applied to the model. The aims of performing various optimization types to brackets are to observe the effect of material change on weight, performing size optimization in addition to topology optimization to the same model. Furthermore, the last optimization objective unlike other optimizations is to establish an optimized design and load paths by implementing topology optimization on a bulk material, despite the absence of a specific design at the initial stage.

sequentially applied to the model. The aims of performing various optimization types to brackets are to observe the effect of material change on weight, performing size optimization in addition to topology optimization to the same model. Furthermore, the last optimization objective unlike other optimizations is to establish an optimized design and load paths by implementing topology optimization on a bulk material, despite the absence of a specific design at the initial stage.

Table 4.1 Optimization Index of FLIR and Gun Bracket

#	Optimization Index	Material	Objective	Specific Initial Model
1	Initial Model	Al 6061 T62 Material	-	✓
2	Topology Optimized Model-1	Al 6061 T62 Material	Mass Reduction	✓
3	Topology Optimized Model-1	AlSi10Mg Material	Mass Reduction	✓
4	Size Optimized Model	Al 6061 T62 Material	Thickness Reduction	✓
5	Size Optimized Model	AlSi10Mg Material	Thickness Reduction	✓
6	Topology Optimized Model-2	AlSi10Mg Material	Mass Fraction Reduction	✗

The main purposes and constraints of general topology optimizations have based on the following formulations as below. In the literature, there are more formulations to apply topology optimization which are given in Table 4.2.

Table 4.2 General Formulations for Topology Optimization [56]

	Objectives	Constraints
1	Minimize (total/regional) Volume/mass Fraction	Max Stress
2	Minimize (total/regional) Volume/mass Fraction	Constrained Frequencies
3	Minimize (weighted/total/regional) Compliance	Constrained Volume/Mass Fraction
4	Minimize (total/regional) Volume/mass Fraction	Constrained Displacements
5	Minimize Combined Compliance and Frequencies	Constrained Volume/Mass Fraction

In this thesis , third formulation have been utilized. Other formulations have been selected as out of scope. To achieve this goal the following procedures are carried out respectively, while performing topology optimization. Firstly, by using part and generative shape modeling tools, design and non-design areas were specified which can be seen in Figure 4.1. Design variables have changed according to selected optimization types.

The design space denotes the region within which the optimal distribution of materials is to be determined, whereas the non-design space encompasses the regions that are subject to boundary conditions and are excluded from the optimization process. In other words, the non-design area is the specific region in which material should be discarded through the optimization process. Nondesign areas have been selected as fasteners and these areas are considered as 1 in every iteration. Therefore, nondesign areas are not considered in any topology optimization iterations.

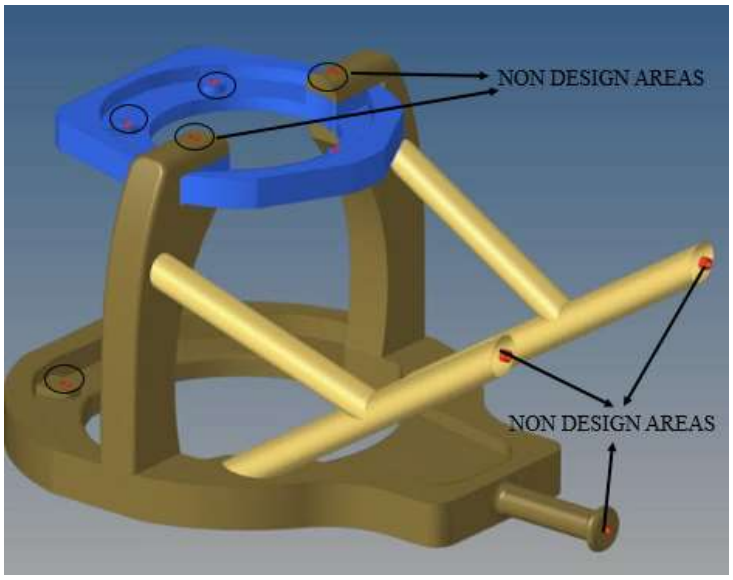

Figure 4.1 Design and Non-Design Areas on Initial Model

After the design and non-design areas were determined, the mechanical properties of Aluminum 6061 T62 were applied to the hypermesh program in the material selection section. These are E, ϑ, and ρ values which are used as inputs to the Hypermesh Altair topology optimization program

Afterwards, it has been decided to an ideal mesh size. Maximizing the size of the design space guarantees that the optimization outcome attains its actual optimal value. However, enlarging the design space also leads to a longer solution time as the number of finite elements increases unnecessarily, consequently reducing the performance of the solver. Furthermore, to avoid complex mesh requirements that result in a high number of finite element usage in the finite element model, the geometry of the design space model has been kept as straightforward as possible.

On the other hands, to deal with discreteness and the checkerboard effect, the optimization problem executes the minimum member size as a constraint function.

The occurrence of the checkerboard effect is attributed to the utilization of mesh elements that are too small, in addition to assigning an inappropriate degree of freedom to each node. Furthermore, checkerboard effect could give rise to improper results and resembles a checkerboard in appearance. However, increasing this minimum member size enhances the design's manufacturability. For all of these reasons, the optimal mesh size has been determined with a mesh study. The element size has been specified as 0.5 mm, and in the design area, a total of 1019398 finite elements and 229345 nodes are utilized .

Generally, volume tetra has been utilized on the model while meshing and tubes are modelled as shell structures. The meshed model which is given in Figure 4.2 was transferred to the Altair Optistruct program from Hypermesh to generate a topology optimization modeling.

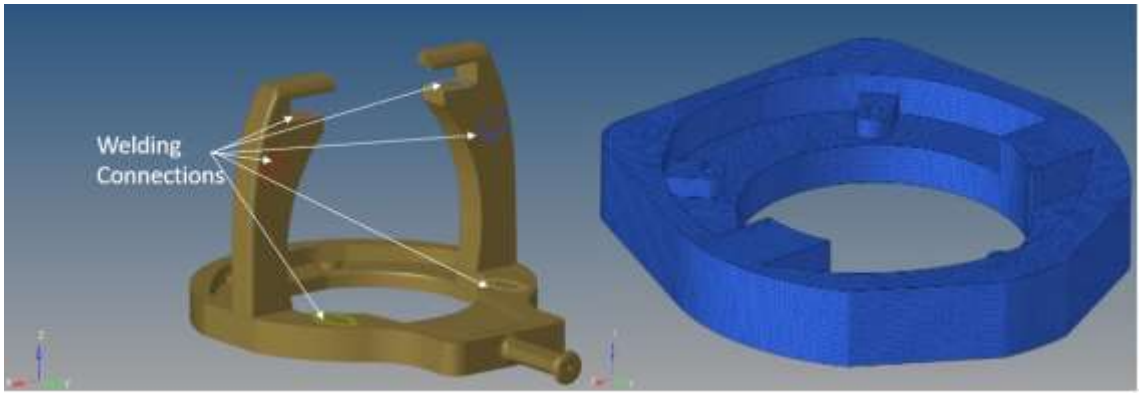

Figure 4.2 Meshed Model with 0.5 mm Element Size

After meshing, another step is to create the necessary inputs for the setup of the topology optimization on the Altair Optistruct program. Taking into account these pieces of information and also based on past experiences, convenient responses, objective and constraints are defined in Table 4.3 .

Table 4.3 Inputs of Topology Optimization Application to Initial Model

Design Variables :	The density of each element in the design space.
Objective Function:	Minimize Mass
Response :	1) Compliance 2) Mass Fraction (%25)
Constraints :	1) Min Compliance 2) Massfrac

4.1 Topology Optimization and Analysis Results-1

- For Al 6061 T62 Material

Typically, when topology optimization is applied to a component, the outcome may include truncated geometries and potentially inaccurate results. To mitigate this issue, the utilization of the Osssmoth tool supports in obtaining more realistic results. By employing

this tool, the clipped geometries within the part are smoothed or softened, ensuring improved accuracy in the optimization outcomes. Values have been included as references in Table 4.20 to demonstrate the difference between the results obtained through topology optimization with Ossmoth applied and the direct output of topology optimization in the next chapter.

The results of the topology optimization in terms of stress and displacement for the material Al 6061 T62 are given in the Figure 4.3 below. In the next section, these stress values for tube and filler equipment are separated, since these results will be compared with the size optimization of the tube. While the stress value of the filler bracket was 144 MPa, the tube was subjected to a stress of 140.8 MPa. Deformation value has been found as 0.5 mm and 1.35 mm for tube and filler bracket respectively.

- For Tube

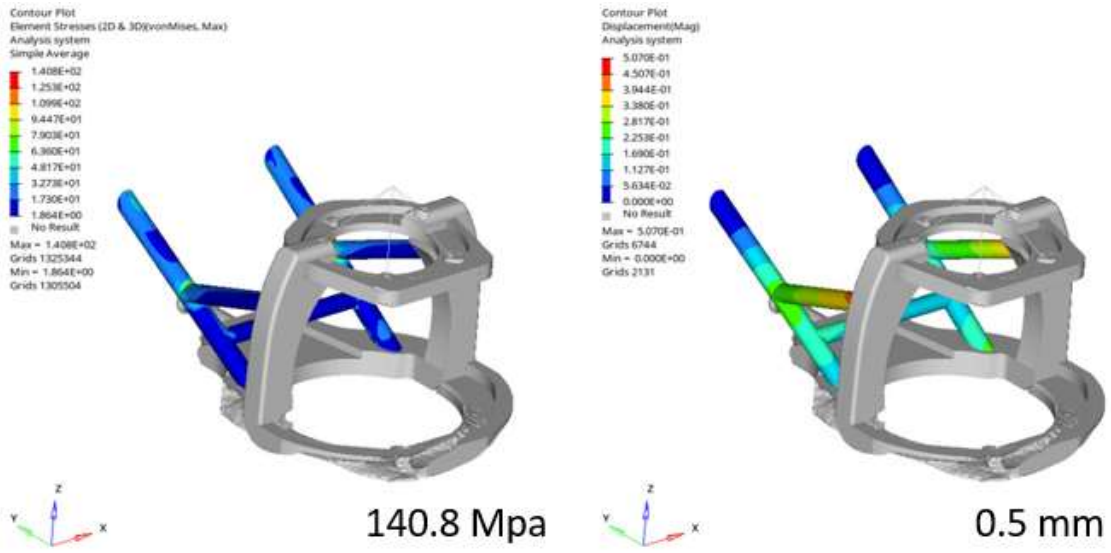

Figure 4.3 The results of Finite Element Analysis with OSSmooth for Al 6061 T62

a) Von-Misses Stress Level (Mpa) b)Displacement (mm)

- For Filler

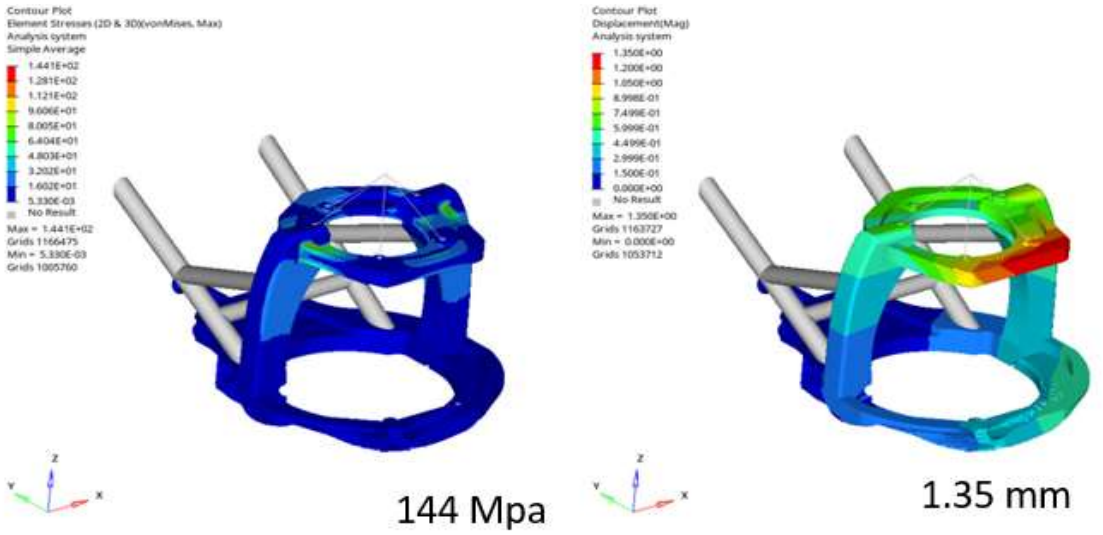

Figure 4.4 The results of Finite Element Analysis with OSSmooth for Al 6061 T62

a) Von-Misses Stress Level (Mpa) b)Displacement (mm)

Furthermore, compliance rose from 1721 Nmm in the initial model to 1733 Nmm which is provided in Table 4.4. Since the difference in compliance is minimal, it could be disregarded. A 15.7 % reduction in weight value was observed. Consequently, it can be inferred that the stiffness remains unchanged during the weight reduction process for the topology optimized part.

Table 4.4 The Results of Topology Optimized Finite Element Analysis (Al 6061 T62 Material)

Volume	= 1.87950E+06	Mass	= 5.09345E-03

Subcase	Compliance	Epsilon
1	1.733218E+03	1.239987E-10

- For AlSi10Mg Material

AlSi10Mg is characterized as an anisotropic material, indicating that its mechanical properties vary with different directions or orientations. By using the experimental data which will be explained in the following chapter in detail, the lowest Elastic Modulus value which is illustrated in Table 4.5, are utilized to complete topology optimization.

Table 4.5 The Results of Tensile Test for AlSi10Mg

Building Direction	Elastic Modulus(GPa)	Yield Strength(MPa)	Tensile Strength(Mpa)
1)Horizontal As-Machined	71	256	395
2)Vertical As-Build	65	234	379
3)Vertical As-Machined	65	255	438

As seen in Figure 4.5 and Figure 4.6, while the stress value for the tube structure is 140.8 MPa, the stress value for the filler structure is 144.1 MPa. When comparing the stress levels of AlSi10Mg and Al 6061 T62 materials under identical load conditions and modeling , no significant changes in stress levels were observed. Nevertheless, the AlSi10Mg material has a lower elastic modulus compared to the Al 6061 T62 material. Thus, the displacement values for the tube and filler have increased from 0.5 mm and 1.35 mm to 0.532 mm and 1.42 mm respectively.

- For Tube

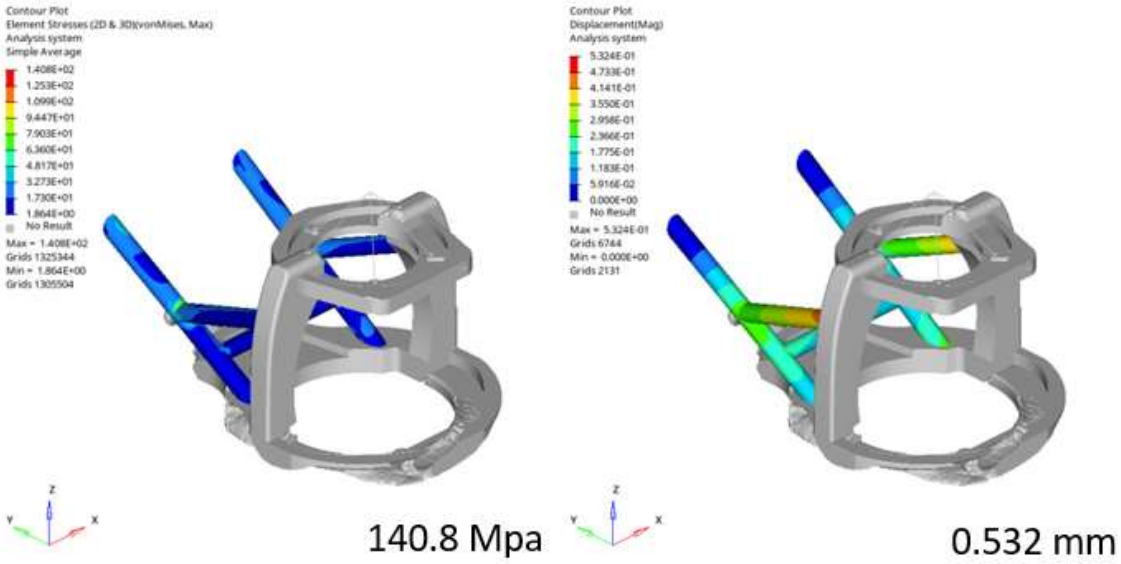

Figure 4.5 The Results of Finite Element Analysis a) Von-Misses Stress Level (Mpa) b)Displacement (mm)

- For Filler

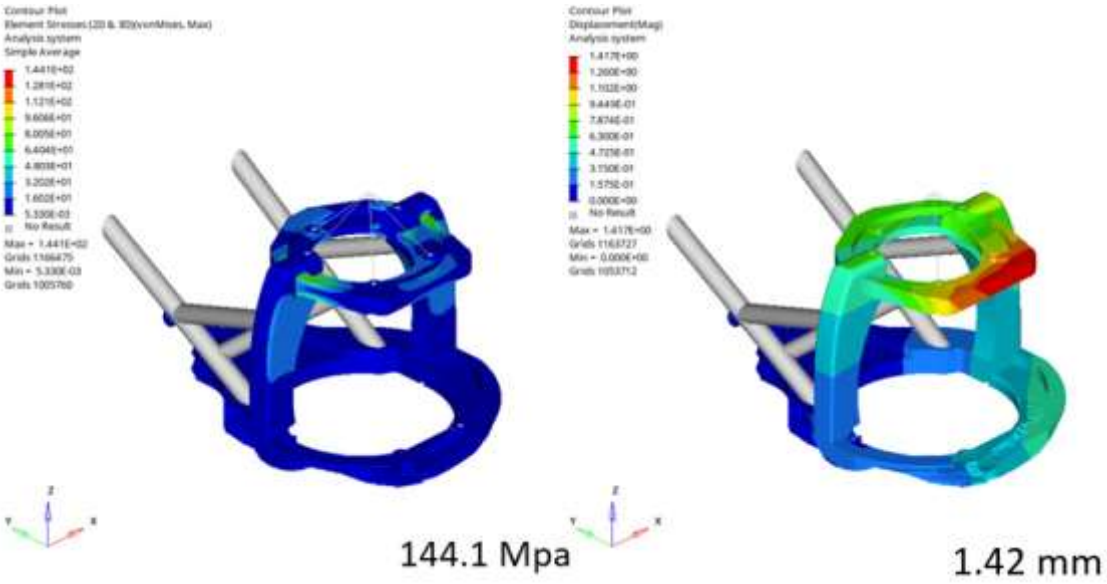

Figure 4.6 The Results of Finite Element Analysis a) Von-Misses Stress Level (Mpa) b)Displacement (mm)

The results of the mass and compliance for bracket are provided in Table 4.6. The findings indicate that the weight remains unchanged compared to the previous material, which can be attributed to the fact that both materials have the same density. Additionally, there was an increase in compliance from 1733 Nmm in the initial model to 1820 Nmm. This is due to the fact that the elastic modulus of the material is lower than the elastic modulus of the initial material. Due to the increase in compliance, there has been a reduction in the stiffness value.

Table 4.6 The Results of Topology Optimized Finite Element Analysis (AlSi10Mg Material)

Volume		=	1.87950E+06	Mass	= 5.09345E-03
Subcase	Compliance	Epsilon			
1	1.820092E+03	-6.099325E-10			

4.2 Size Optimization and Analysis Results

Size optimization have been performed on tubes and filler bracket in order to further reduce weight and maximize stiffness. Initially, tubes on bracket have been modelled as shell elements. Thickness of tubes have been selected as design variables. Input data of size optimization are given in Table 4.7.

Table 4.7 Inputs of Size Optimization Application to Optimized Model

Design Variables	:	Thickness of Tubes (1.6 mm-3 mm) Increments 0.1 mm
Objective Function	:	1) Minimize Mass
Response	:	1) Compliance 2) Static Stress
Constraints	:	1) Min Compliance 2) Mass

1) Al 6061 T62 Material

Since the aim of size optimization is to find the ideal tube thickness, machined parts have been displayed separately in terms of stress level and displacement.

Upon applying size optimization to the component previously subjected to topology optimization, the stress values in the tube section, originally measured at 140.8 MPa, exhibited an increase to 232.3 MPa. The stress value on the filler bracket remained nearly unchanged after the size optimization process. In the size optimization for Al 6061 T62 material, the deformation values have exhibited an increase compared to the previous topology optimization model. This can be attributed to the rise in the compliance value. The corresponding outcomes are illustrated in Figure 4.7 and Figure 4.8.

- For Tube

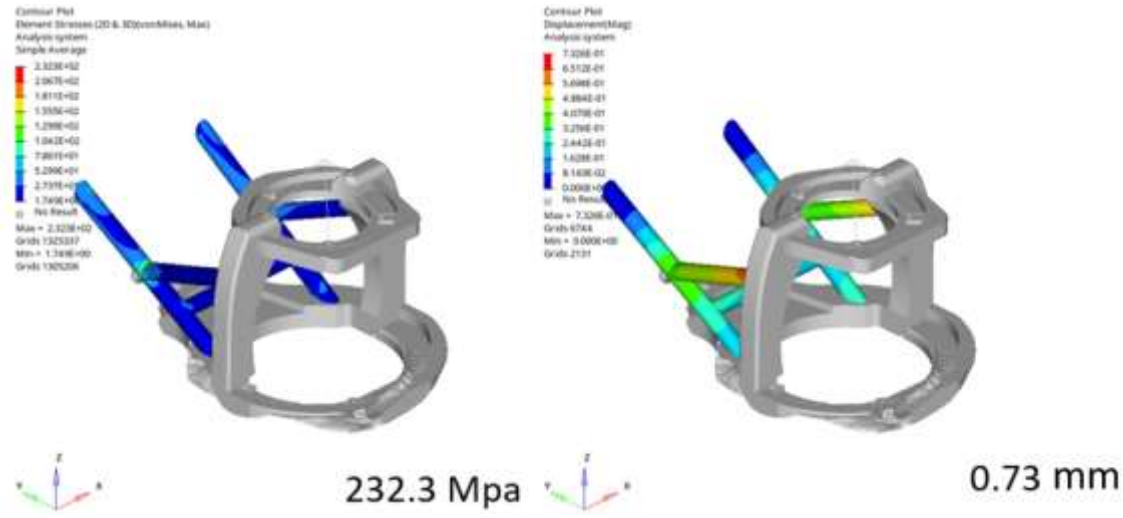

Figure 4.7 The results of Finite Element Analysis a) Von-Misses Stress Level (Mpa) b)Displacement (mm)

- For Filler

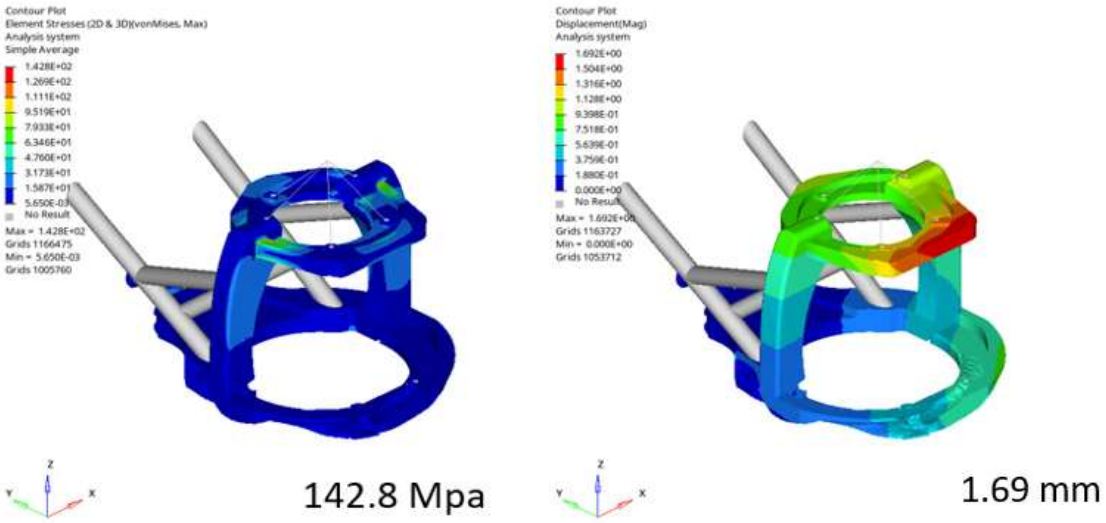

Figure 4.8 The results of Finite Element Analysis a) Von-Misses Stress Level (Mpa) b)Displacement (mm)

According to constraint of minumum compliance and mass , ideal thickness value has been found as 1.87 mm. By reducing the tube thickness from 3 mm to 1.87 mm, the overall weight decreased to 4.89 kg from 6.04 kg, while the stiffness experienced a decrease. Compliance values have changed from 1721 Nmm to 2066 Nmm, as indicated in Table 4.8, without material change.

Table 4.8 The Results of Size Optimized Finite Element Analysis (Al 6061 T62 Material)

Volume		=	1.80449E+06	Mass	= 4.89017E-03
Subcase	Compliance	Epsilon			
1	2.066485E+03	4.754079E-10			

2) AlSi10Mg Material

The stress, displacement, stiffness, and weight values for the AlSi10Mg material in size optimization are presented in the Figure 4.9 , Figure 4.10 and Table 4.9.

When comparing the size optimization outcomes for AlSi10Mg and Al 6061 T62 materials, it was observed that the stress values remained unchanged for tube and stress value increased from 232.3 Mpa to 245.5 Mpa. However, due to the lower elastic modulus of the AlSi10Mg material in comparison to the Al 6061 T62 material, the compatibility

increased from 2066 Nmm to 2218 Nmm. Furthermore, a decrease in stiffness and an increase in deformation were observed.

- For Tube

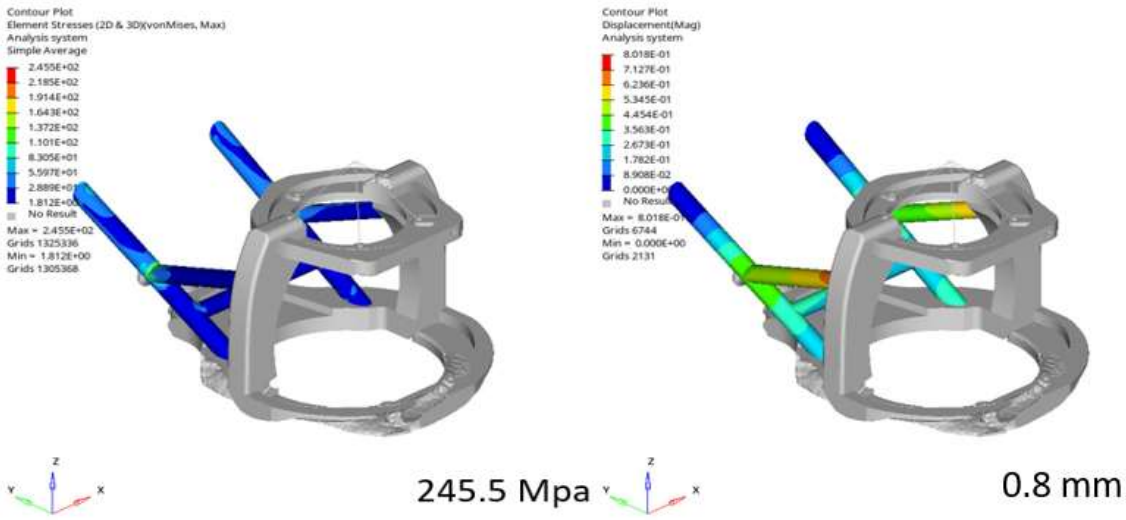

Figure 4.9 The results of Finite Element Analysis a) Von-Misses Stress Level (Mpa) b)Displacement (mm)

- For Filler

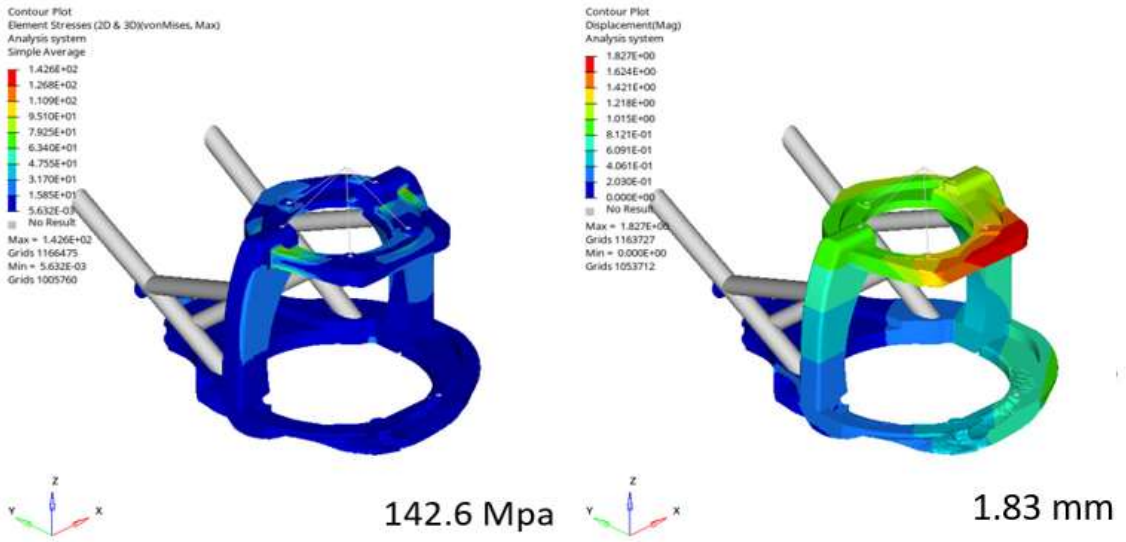

Figure 4.10 The results of Finite Element Analysis a) Von-Misses Stress Level (Mpa) b)Displacement (mm)

Since both AlSi10Mg and Al6061 T62 materials have the same density, the mass value, as indicated in Table 4.9 remains unaltered.

Table 4.9 The Results of Size Optimized Finite Element Analysis (AlSi10Mg Material)

```
Volume                          =  1.79823E+06   Mass      =  4.87321E-03
-----------------------------------
Subcase    Compliance       Epsilon
-----------------------------------
      1  2.218122E+03 -6.001413E-10
-----------------------------------
```

4.3 Topology Optimization and Analysis Results-2

Throughout all applied optimizations in this thesis, the initial design was predetermined. However, in this topology optimization application, optimization has been employed to extract the optimal shape from the bulk material, utilizing the same boundaries and load condition as the previous model. Hence, the initial design does not exist.

Firsly, the mesh has been re-implemented, utilizing a mesh element of 1029724, with 241791 nodes being utilized in the analysis AlSi10Mg material.

Input data of shape optimization are given in Table 4.10. Design space has been selected outer boundary of previous model.

Table 4.10 Inputs of Shape Optimization Application to Optimized Model

Design Variables :	Design Space
Objective Function:	1)Minimize Mass
Response :	1) Mass 2) Total Displacement
Constraints :	Mass Fraction (0.5)

Boundary condition and the reesult of topology optimization have been shown in Figure 4.11. In general, it is recommended to apply optimization before the modeling stage[60].

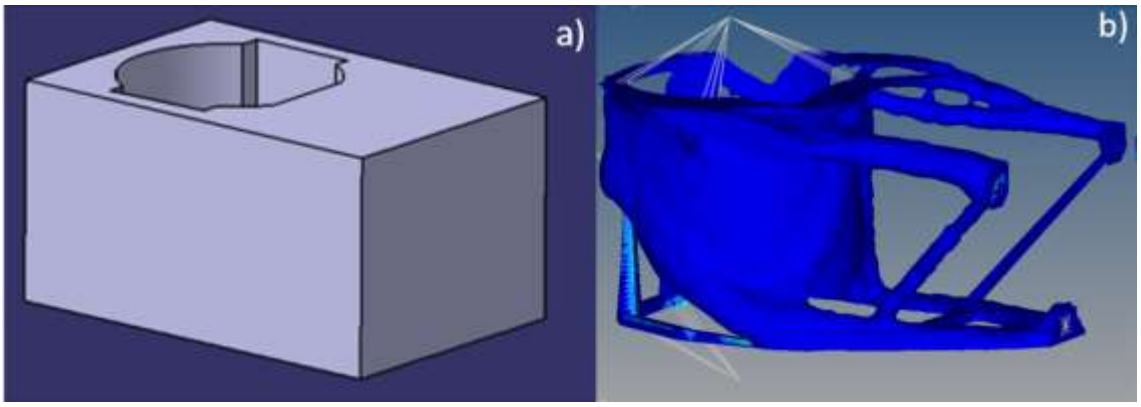

Figure 4.11 a)Initial Boundary Condition b)Topology Optimized Design from Bulk Model

Figure 4.12 and Figure 4.13 show a significant reduction in stress from 140.2 MPa to 114 MPa. In addition, the weight decreased to 4.79 kg from 6.04 kg. Simultaneously, the compliance value drops from 164 Nmm to 1721 Nmm, indicating a significant improvement in stiffness as shown in Table 4.11.

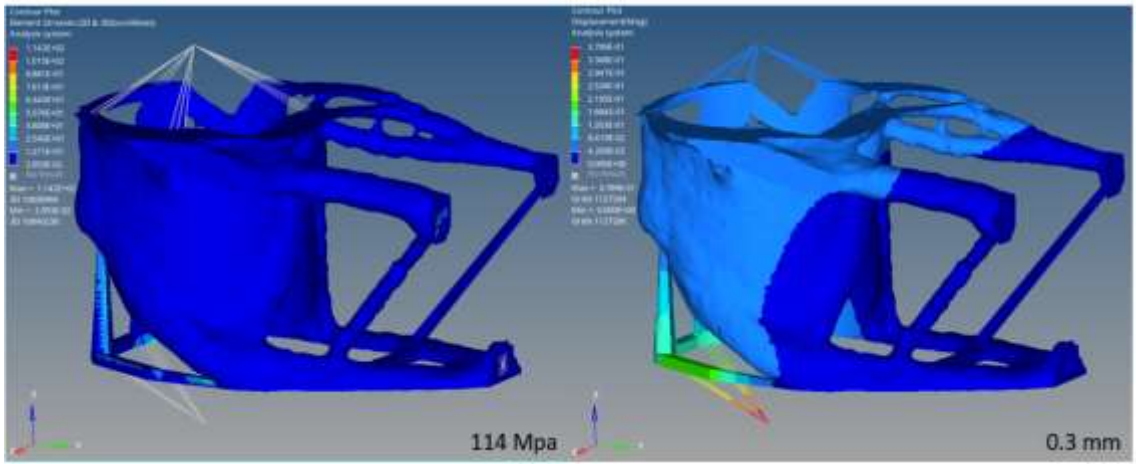

Figure 4.12 The results of Finite Element Analysis a) Von-Misses Stress Level (Mpa) b)Displacement (mm)

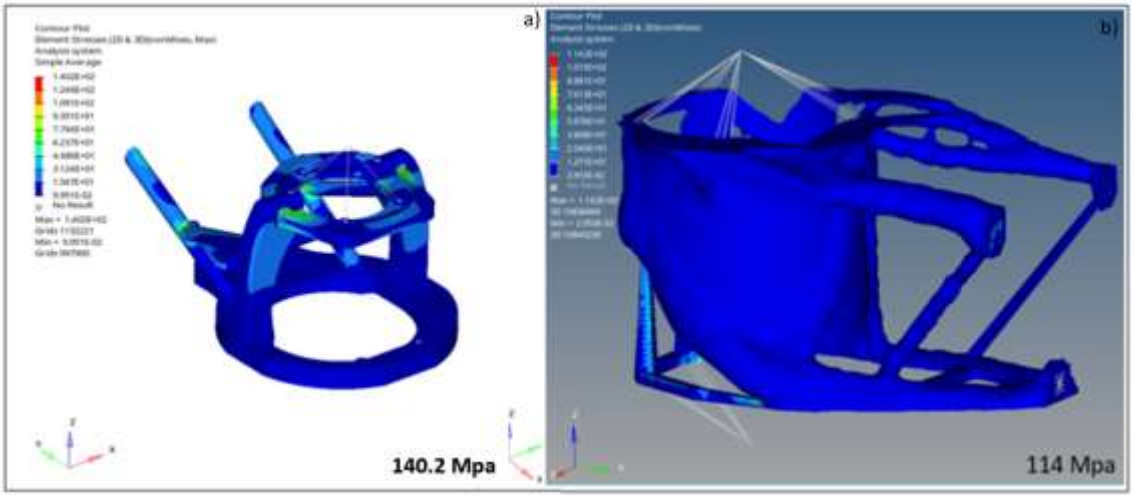

Figure 4.13 The Comparison of Von-Mises Stress Level a) Initial Model (Al 6061 T62 Material) b)Shape Optimized Model (AlSi10Mg Material)

Table 4.11 The Results of Size Optimized Finite Element Analysis (AlSi10Mg Material)

Volume		=	1.77054E+06	Mass	= 4.79817E-03

Subcase	Compliance	Epsilon
2	1.591035E+02	6.831062E-13
3	1.648088E+02	7.418910E-13

According to topology optimization result, mass fraction value has been converged to 0.05 which is shown in Table 4.12.

Table 4.12 Mass Fraction vs Iteration Number Graph

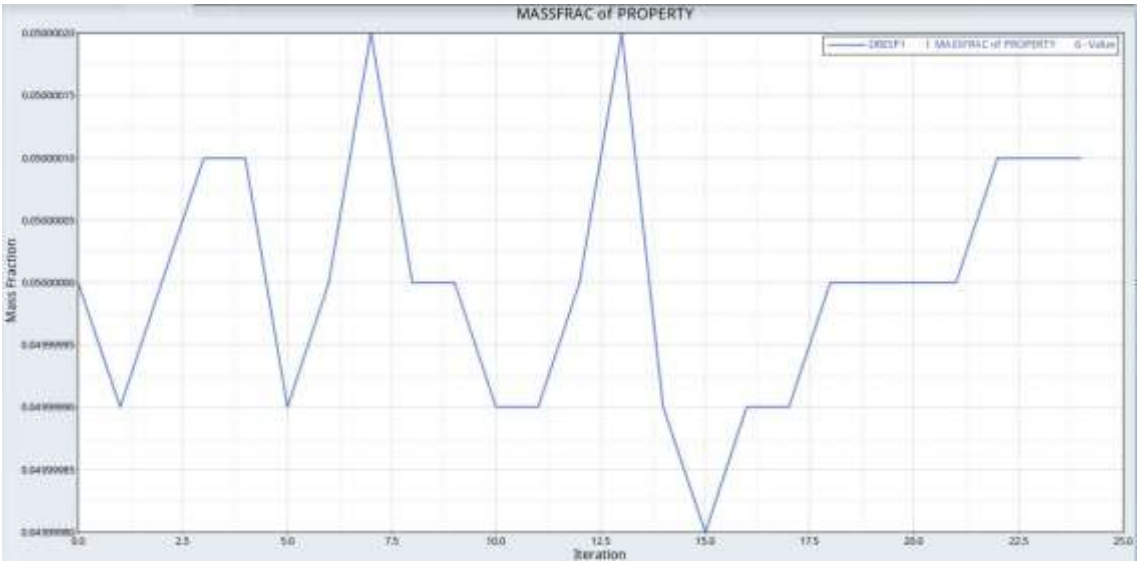

Optimization has been completed with 14 iteration which is illustrated in Table 4.13. The objective value remained the same after 14 iterations.

Table 4.13 Compliance vs Iteration Number Graph

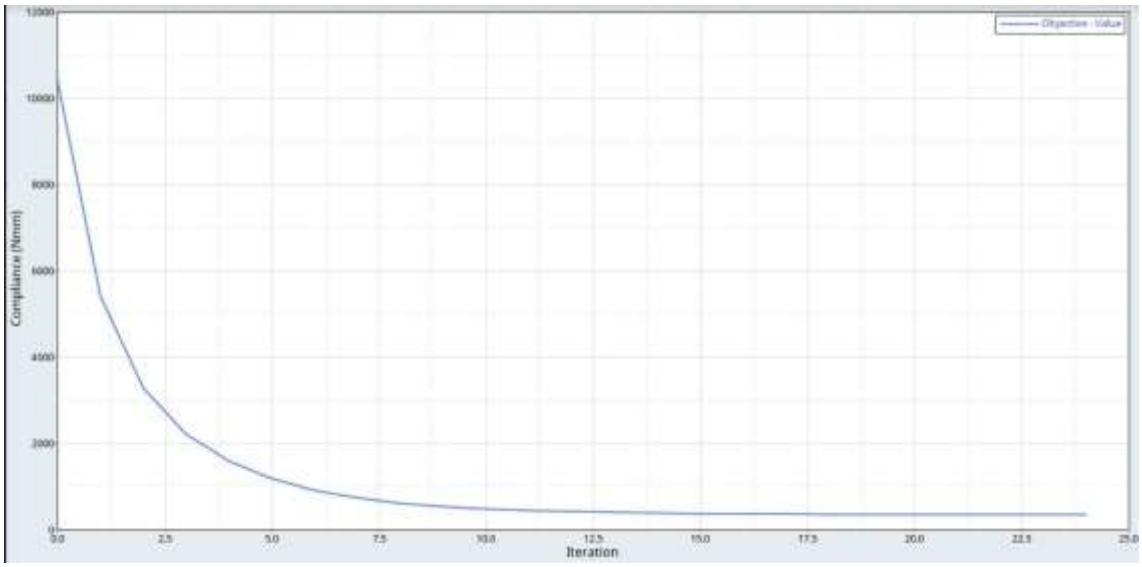

The final graph, represented in Table 4.14, illustrates that a feasible design has been successfully attained, meeting all the predetermined constraints.

Table 4.14 Iteration vs Constraint Violation(%) Graph

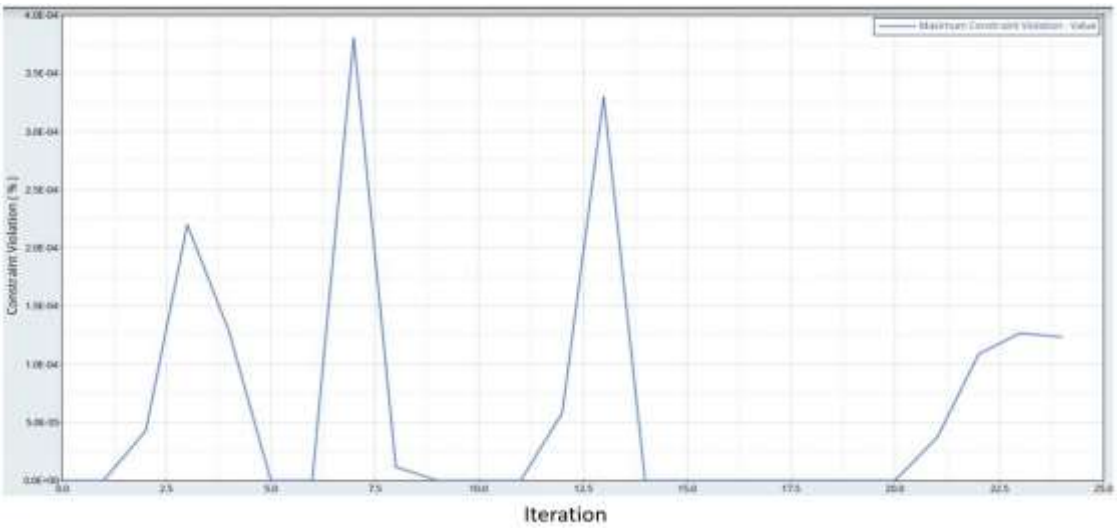

4.4 Modal Analysis Results

Although weight reduction and stress level could be controlled by topology optimization, additional analysis is required to calculate the frequency values of the optimized model. Therefore, after the optimization process is completed, modal analysis is used to calculate the natural frequency of the optimized part and the associated modes of vibration of that part.

- Topology Optimized Modal Analysis : Al 6061 T62 Material

Topology optimization modal analysis for Al 6061 T62 material is shown in Table 4.15 and Figure 4.14. According to the modal analysis results, the first 3 natural frequency values are 67, 185 and 304 Hz, respectively. These values do not coincide with helicopter main rotor and blade pass frequencies.

Table 4.15 The Results of Modal Analysis for Different Mode Shapes (Al 6061 T62 Material)

Model	Model
Subcase 1 (modal1)	
Mode 2 - F = 1.855671E+02	
Mode 1 - F = 6.764114E+01	Mode 11 - F = 9.518261E+02
Mode 2 - F = 1.855671E+02	Mode 12 - F = 1.117480E+03
Mode 3 - F = 3.044751E+02	Mode 13 - F = 1.345040E+03
Mode 4 - F = 3.490846E+02	Mode 14 - F = 1.447433E+03
Mode 5 - F = 4.469521E+02	Mode 15 - F = 1.527890E+03
Mode 6 - F = 4.547319E+02	Mode 16 - F = 1.604162E+03
Mode 7 - F = 4.785911E+02	Mode 17 - F = 1.627806E+03
Mode 8 - F = 6.921451E+02	Mode 18 - F = 1.850840E+03
Mode 9 - F = 7.885495E+02	Mode 19 - F = 1.899581E+03
Mode 10 - F = 8.428496E+02	Mode 20 - F = 1.988375E+03

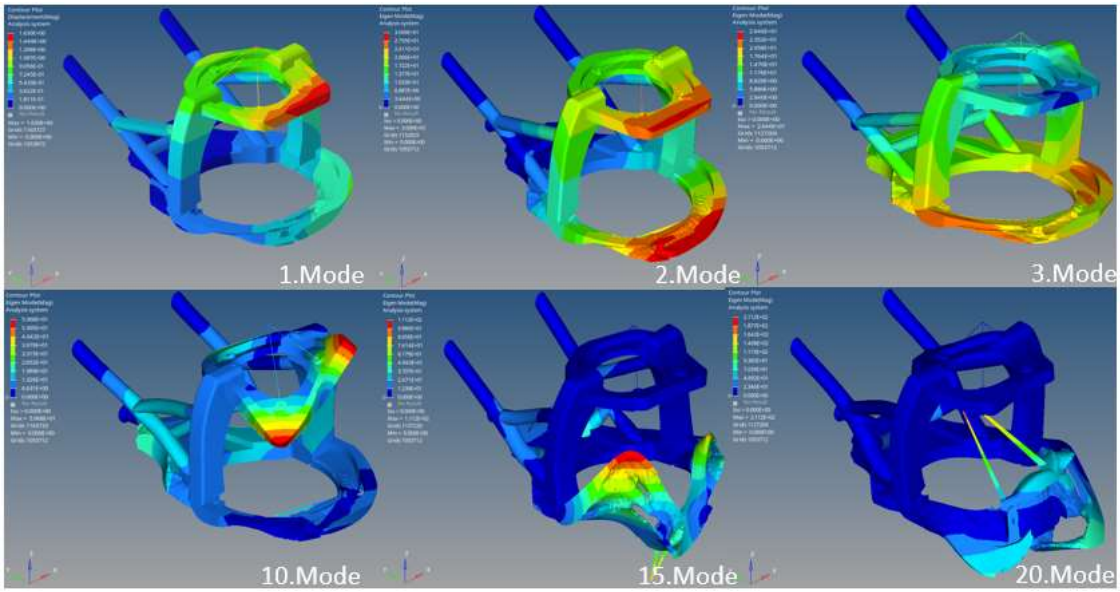

Figure 4.14 Natural Frequency Modes 1,2,3,10,15 and 20 for Topology Optimized Model (Al6061 T62 Material)

- Topology Optimized Modal Analysis : AlSi10Mg Material

The identical analysis was conducted for the AlSi10Mg material to examine whether the natural frequencies of the new design coincide with the natural frequency value of the

helicopter. These results have been illustrated in Figure 4.15 and Table 4.16. The first 3 frequency values are as follows; approximately 60 Hz ,180 Hz and 261 Hz.

Table 4.16 The Results of Modal Analysis for Different Mode Shapes (AlSi10Mg Material)

Model	Model
Subcase 1 (modal1)	
Mode 1 - F = 6.001050E+01	
Mode 1 - F = 6.001050E+01	Mode 11 - F = 9.288328E+02
Mode 2 - F = 1.809635E+02	Mode 12 - F = 1.090485E+03
Mode 3 - F = 2.611198E+02	Mode 13 - F = 1.312548E+03
Mode 4 - F = 3.406518E+02	Mode 14 - F = 1.412467E+03
Mode 5 - F = 4.361550E+02	Mode 15 - F = 1.490980E+03
Mode 6 - F = 4.437469E+02	Mode 16 - F = 1.565410E+03
Mode 7 - F = 4.670297E+02	Mode 17 - F = 1.588483E+03
Mode 8 - F = 6.754249E+02	Mode 18 - F = 1.806129E+03
Mode 9 - F = 7.694995E+02	Mode 19 - F = 1.853693E+03
Mode 10 - F = 8.224888E+02	Mode 20 - F = 1.940341E+03

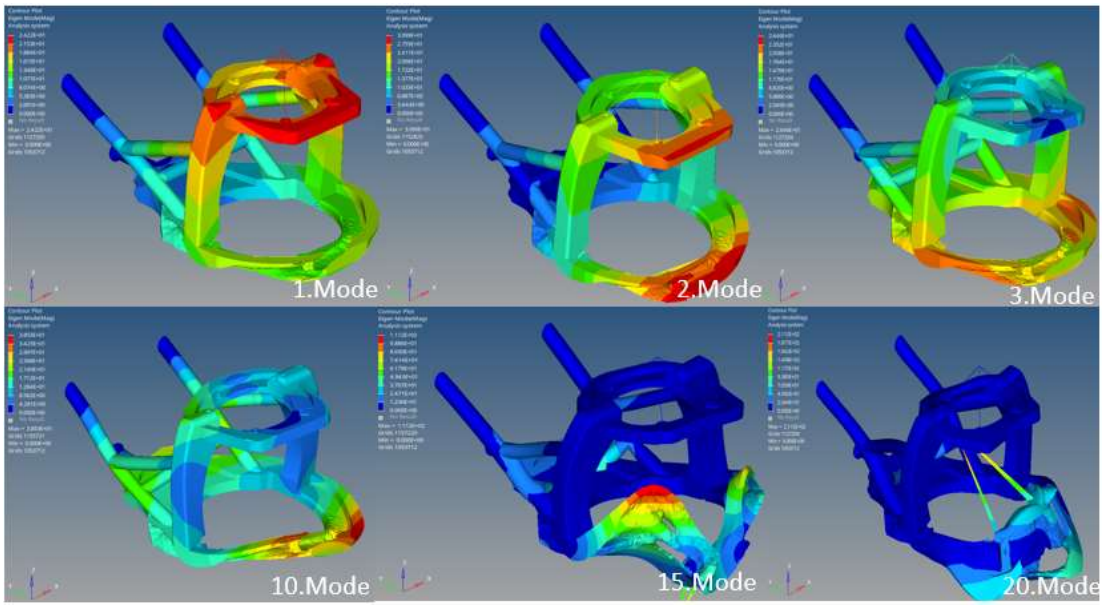

Figure 4.15 Natural Frequency Modes 1,2,3,10,15 and 20 for Topology Optimized Model (AlSi10Mg Material)

- Size Optimized Modal Analysis : Al 6061 T62 Material

The results of the size optimizated modal analysis for Al 6061 T62 material are presented in Table 4.17 and Figure 4.16. According to the modal analysis findings, the first three natural frequency values are 70 Hz, 149 Hz, and 297 Hz, respectively. These frequencies do not align with the main rotor and blade pass frequencies of the helicopter.

Table 4.17 The Results of Modal Analysis for Different Mode Shapes (Al 6061 T62 Material)

Model	Model
Subcase 1 (modal1)	
Mode 1 - F = 6.991050E+01	
Mode 1 - F = 6.991050E+01	Mode 11 - F = 9.288328E+02
Mode 2 - F = 1.499635E+02	Mode 12 - F = 1.090485E+03
Mode 3 - F = 2.971198E+02	Mode 13 - F = 1.312548E+03
Mode 4 - F = 3.406518E+02	Mode 14 - F = 1.412467E+03
Mode 5 - F = 4.361550E+02	Mode 15 - F = 1.490980E+03
Mode 6 - F = 4.437469E+02	Mode 16 - F = 1.565410E+03
Mode 7 - F = 4.670297E+02	Mode 17 - F = 1.588483E+03
Mode 8 - F = 6.754245E+02	Mode 18 - F = 1.806129E+03
Mode 9 - F = 7.694995E+02	Mode 19 - F = 1.853693E+03
Mode 10 - F = 8.224888E+02	Mode 20 - F = 1.940341E+03

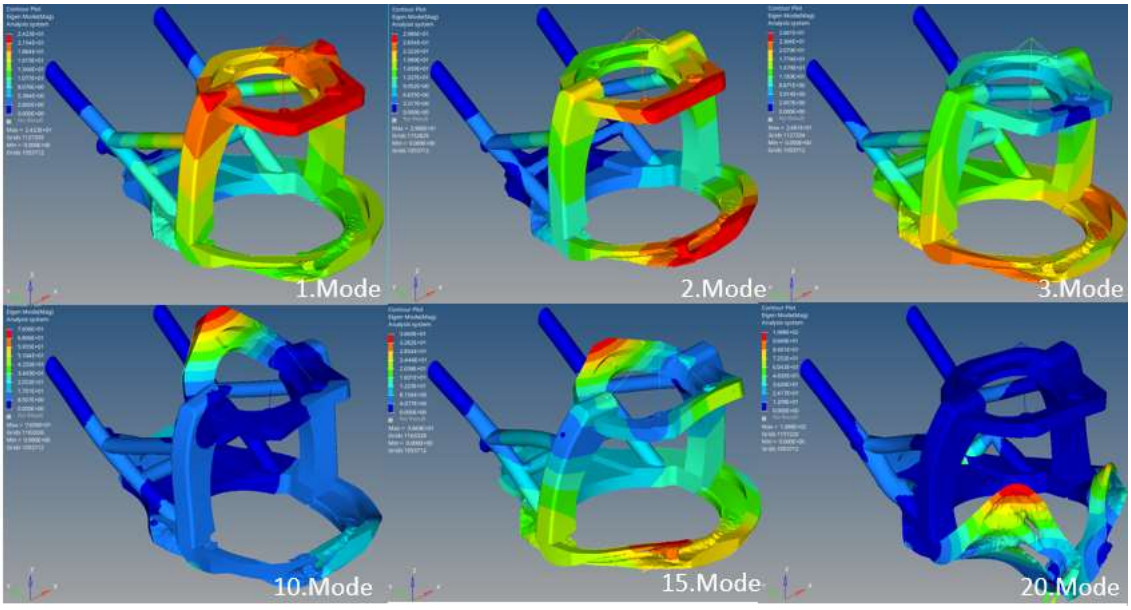

Figure 4.16 Natural Frequency Modes 1,2,3,10,15 and 20 for Topology Optimized Model (Al 6061 T62 Material)

- Size Optimized Modal Analysis : AlSi10Mg Material

A parallel analysis was also performed on AlSi10Mg material to evaluate the harmony between the natural frequencies of the new design and the natural frequency of the helicopter. The results of this analysis are shown in Table 4.18 and Figure 4.17. The first three frequencies obtained are approximately 60 Hz, 170 Hz and 297 Hz.

Table 4.18 The Results of Modal Analysis for Different Mode Shapes (AlSi10Mg Material)

Model	Model
Subcase 1 (modal1)	
Mode 1 - F = 5.991050E+01	
Mode 1 - F = 5.991050E+01	Mode 11 - F = 9.288328E+02
Mode 2 - F = 1.709635E+02	Mode 12 - F = 1.090485E+03
Mode 3 - F = 2.971198E+02	Mode 13 - F = 1.312548E+03
Mode 4 - F = 3.406518E+02	Mode 14 - F = 1.412467E+03
Mode 5 - F = 4.361550E+02	Mode 15 - F = 1.490980E+03
Mode 6 - F = 4.437469E+02	Mode 16 - F = 1.565410E+03
Mode 7 - F = 4.670297E+02	Mode 17 - F = 1.588483E+03
Mode 8 - F = 6.754249E+02	Mode 18 - F = 1.806129E+03
Mode 9 - F = 7.694995E+02	Mode 19 - F = 1.853693E+03
Mode 10 - F = 8.224888E+02	Mode 20 - F = 1.940341E+03

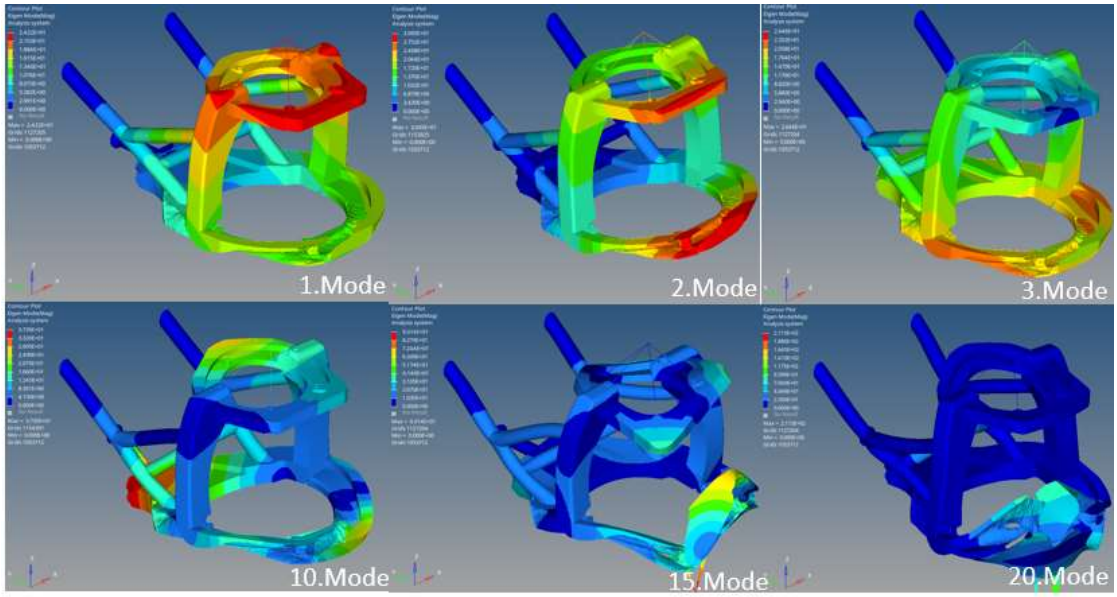

Figure 4.17 Natural Frequency Modes 1,2,3,10,15 and 20 for Topology Optimized Model (AlSi10Mg Material)

- Topology Optimization Modal Analysis : AlSi10Mg Material (Bulk Model)

The modal analysis results for the topology-optimized configuration by using AlSi10Mg material are shown in Table 4.19 and Figure 4.18. The difference in this model is that the novel model is obtained by removing material from the bulk structure while maintaining the boundary condition of the first topology optimized model.

Based on the analysis, the first three natural frequency values are identified as 228 Hz, 289 Hz, and 426 Hz, respectively. Furthermore, it is observed that these frequencies do not correspond to the main rotor and blade pass frequencies of the helicopter.

Table 4.19 The Results of Modal Analysis for Different Mode Shapes (AlSi10Mg Material)

Mode 1 - F = 2.282267E+02	Mode 1 - F = 2.282267E+02
Mode 1 - F = 2.282267E+02	Mode 11 - F = 1.522565E+03
Mode 2 - F = 2.890302E+02	Mode 12 - F = 1.611203E+03
Mode 3 - F = 4.269063E+02	Mode 13 - F = 1.666375E+03
Mode 4 - F = 6.809297E+02	Mode 14 - F = 1.761228E+03
Mode 5 - F = 7.345931E+02	Mode 15 - F = 1.800271E+03
Mode 6 - F = 1.042045E+03	Mode 16 - F = 1.833475E+03
Mode 7 - F = 1.063515E+03	Mode 17 - F = 1.861891E+03
Mode 8 - F = 1.198807E+03	Mode 18 - F = 1.911501E+03
Mode 9 - F = 1.329168E+03	Mode 19 - F = 1.982084E+03
Mode 10 - F = 1.414811E+03	Mode 20 - F = 2.056609E+03

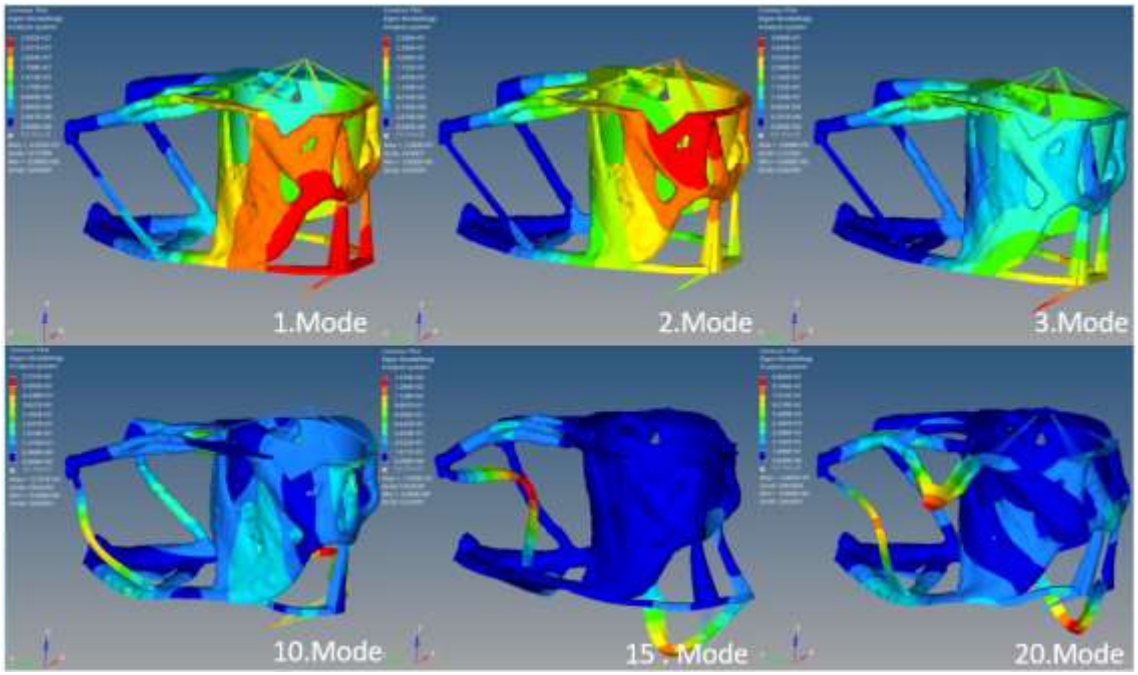

Figure 4.18 Natural Frequency Modes 1,2,3,10,15 and 20 for Topology Optimized Model (AlSi10Mg Material)

According to these results, mode shapes have been shifted and structural stiffnesss has been enhanced from 61 Hz to 228 Hz when the initial modes of the structure were compared with those of the first model.

To sum up, Table 4.20 demonstrates that both topology and size optimizations contribute to the reduction of component weight. After the initial analysis, it is observed that the topology-optimized model, made of Al 6061 material, has a slightly higher compliance value. An increase in compliance implies a decrease in material stiffness, resulting in a slight increase in strain. Meanwhile, the increase in compliance and strain is assumed to be negligible. Furthermore, both the initial model and the topology-optimized model exhibit the same stress values. Comparing the stress, strain, and compliance values, it can

be concluded that the weight reduction does not have a significant impact on the static analysis results. Following the completion of the initial run, the subsequent analysis continued with a new model featuring smoother surfaces compared to the initially optimized design. As the topology optimization process may result in clipped images, the model was smoothed using the Ossmoth program which is special tool, rendering it suitable for modal analysis. Subsequently, a second round of analysis was carried out, and the results are presented in Table 4.20, labeled as "Topology Optimized_Oss". Once again, similar stress, strain, and compliance values were obtained when compared to the initial model. The first optimized model, with its sharp surfaces, was solely utilized for illustrative purposes, whereas the outputs of the second analysis are considered as the actual values for further analysis and comparison with the initial model.

Separate stress results for both the tube and filler components as shown as Table 4.20, facilitate comparison with the results of size optimization. In an effort to reduce the component's weight, size optimization was carried out by decreasing the thickness of the tube component from 3 mm to 1.87 mm, resulting in the expected increase in stress values, from 140.8 MPa to 232.3 MPa. As anticipated, stress values have increased. However, since the factor of safety, as indicated in Table 4.21, remains above 1, these values can be considered acceptable. Thus far, the results of topology and size optimization for Al 6061 material have been presented for the purpose of comparison with the results for AlSi10Mg material. Subsequently, all the analyses conducted for Al 6061 material were replicated for AlSi10Mg, and the outcomes are provided in Table 4.20. Upon analyzing the results, no significant changes in stress, strain, and compliance values were observed since density of both material was taken as same, and elastic modulus values were similar.

Finally, additional topology optimization from the bulk structure was conducted, resulting in a notable reduction in stress values from 140.2 MPa to 114 MPa. Moreover, a significant decrease in compliance values was observed. The decrease in compliance signifies an increase in stiffness, leading to a more rigid structure. Consequently, the deformation was reduced from 1.33 mm to 0.3 mm. Additionally, final topology optimization led to a substantial increase in the first-order natural frequency, ascending from 61 Hz to 228 Hz. This improvement in the dynamic characteristic of the part indicates an enhanced rigidity resulting from the shape optimization process.

Consequently, it can be inferred that utilizing the SLM method with optimization enables the production of lighter components within a short time manufacturing frame, without significantly compromising the safety margin of the part.

Table 4.20 Comparing of Material Properties and Dynamic Characteristics

	Optimization Types	Mass (kg)	Stress (Mpa)	Deformation (mm)	Compliance (Nmm)	Thickness (mm)
1)	Initial Model (Al6061 Material)	6.04	140.2	1.33	1721	3
2)	Topology Optimized_Oss* (Al 6061Material)	5.09	Tube:140.8 Filler:144	Tube:0.5 Filler:1.35	1733	3
3)	Size Optimized Model (Al 6061 Material)	4.89	Tube:232.3 Filler:142.8	Tube:0.73 Filler:1.69	2066	1.87
4)	Topology Optimized Model (AlSi10Mg Material)	5.09	Tube:140.8 Filler:144.1	Tube:0.53 Filler:1.42	1820	3
5)	Size Optimized Model (AlSi10Mg Material)	4.87	Tube:245.5 Filler:142.6	Tube:0.8 Filler:1.83	2218	1.77
6)	Topology Optimized Model (Bulk-AlSi10Mg Material)	4.79	114	0.3	164	X

*OSSmooth Tool

Table 4.21 Comparison of Modal Analysis Results and Safety Factors

Dynamic Performance Index	Mass (kg)	First-order Natural Frequency (Hz)	Second-order Natural frequency (Hz)	Third-order Natural frequency (Hz)	Yield Strength (Mpa)	Factor of Safety
Initial Model (Al6061 Material)	6.04	61	193	292	241.4	1.72
Topology Optimized_Oss (Al 6061 Material)	5.09	67	185	304	241.4	1.68
Size Optimized Model (Al 6061 Material)	4.89	70	149	297	241.4	1.04
Topology Optimized Model (AlSi10Mg Material)	5.09	60	180	261	255	1.77
Size Optimized Model (AlSi10Mg Material)	4.87	52	146	215	255	1.04
Topology Optimized Model (AlSi10Mg Material) Bulk Model	4.79	228	289	426	255	2.23

5. EXPERIMENTAL PROCEDURES AND RESULTS

5.1 Experimental Procedure of Coupon Sample Manufacturing

In this study, AlSi10Mg material which is known as anisotropic material was utilized. Anisotropic materials could be defined as materials whose physical properties could change in different directions. Firstly, 12 coupon samples were manufactured by using an SLM machine. SI3619 machine which is an M400 model of EOS company was used. Their orientation and geometry in the machine were different. Powder sizes were selected as 30 µm per EN10204 specification. The recoater speed was selected as 250 mm/s. The samples were printed in two different orientations; horizontal and vertical. Moreover, their geometry was categorized into two different shapes, cylindrical and “dog-bone” shapes. These are shown in Figure 5.1 and Figure 5.2. The purpose of producing cylindrical specimen is to subsequently machine them into "dog-bone" tensile specimen geometry, following the specifications outlined in ASTM-E8 for Specimen 3 type round bars. The remaining samples were aimed to use in tensile test as-build condition. The decision not to produce "Dog-Bone" shaped samples in the horizontal orientation was due to the significant number of supports required during the printing process. Since the required number of supporters was very high, it was not effective to manufacture “Dog-Bone” shaped samples in horizontal orientation. “Dog-Bone” and cylindrical-shaped specimens are called as As-Build and As-Machined, respectively, in this thesis. Table 5.1 indicates the specimens used for mechanical and metallurgical characterization of AlSi10Mg alloy. Figure 5.1 depicts the schematic of the specimen in the form of a round dog bone.

After printing operations were completed, all specimens were exposed to stress relief heat treatment at 190 °C for 2 hours. Then, as-machined samples were machined by using a turning machine in order to obtain tensile specimens according to the dimensions given in Figure 5.1. Permanent markings with the vibro-engrave method were carefully applied on the bottom micro specimens while specimens representing the top side of the samples were already identified during printing as shown in Figure 5.4. Then, destructive and non-destructive tests were performed as explained in section 5.2.

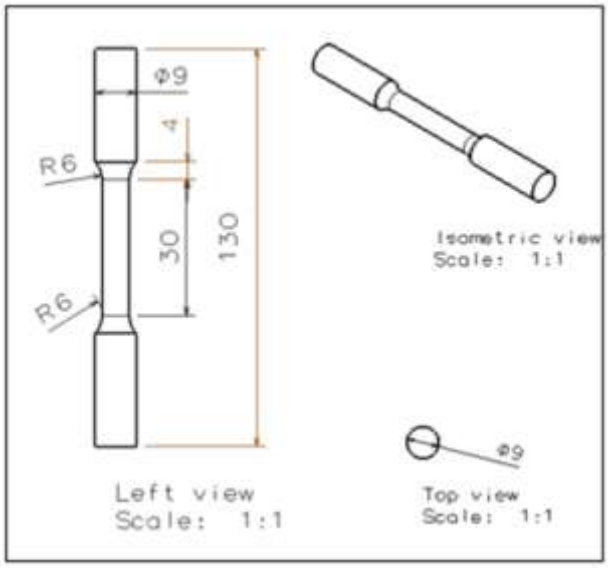

Figure 5.1 Drawing of Dog Bone Shape Test Sample

Figure 5.2 Cylindrical Shaped and Dog Bone Shaped Test Samples

Table 5.1 Quantity of Printed Specimens

# of Batch	Specimen Identification	Vertical	Horizantal
1. Batch	As-Machined	3	6
	As-Build	3	N/A

Each specimen were marked during printing. Table 5.2 indicates their definitions respectively.

Table 5.2 Type and Identification of the Specimens

# of Batch	Specimen Identification	Specimen Type
1. Batch	V1	As-Build
	V2	As-Machined
	V3	As-Build
	V4	As-Machined
	V5	As-Build
	V6	As-Machined
	H1	As-Machined
	H2	As-Machined
	H3	As-Machined
	H4	As-Machined
	H5	As-Machined
	H6	As-Machined

5.2 Test Methods of Coupon Samples

5.2.1 Non-Destructive Tests

- **Radiographic Test**

First of all, all as-machined and as-build samples were raidographically examined as explained in the following chapter. Each sample given in Table 5.2 was inspected by using digital X-ray radiography per ASTM E2033. The results were evaluated per ASTM E2422. Acceptance criteria were given per AMS-A-21180 Table 2 Grade B. Balteau Baltographt SD225/3 Digital X-Ray machine was used during radiographic film examination.

- **Surface Roughness**

After radiographic test, representative samples were selected from all 12 specimens. 3 of them were used for surface roughness analysis. Mahr surface roughness measurement machine, MarSurf VD 280 BG 22, was used during the experiments.

Samples given in Table 5.3 were selected for roughness measurement to represent all batches.

- **Liquid Penetrant Inspection**

After the roughness measurement is completed, a liquid penetrant inspection was performed on the as-machined samples according to ASTM E1417 Type I Method A Form D Sensitivity Level 3. No crack or linear indications were accepted.

Up to now, non-destructive tests and inspections were detailed. The following chapters give details about the destructive test examinations.

- **Microstructure Analysis**

Microstructural analysis was performed from the representative 3 samples. Table 5.3 shows the identification of the samples conducted for microstructural analysis.

Table 5.3 Surface Roughness and Microstructural Analysis Sample's Identification

# of Batch	Specimen Identification	Specimen Type
1. Batch	V1	As-Build
	V2	As-Machined
	H2	As-Machined

Samples given in above were firstly cut from the top and bottom faces as they were seen in Figure 5.3 and Figure 5.4. ATM BRILLANT 265 cutting machine was used for microstructural specimen extractions. The remaining middle portion of the samples was used for tensile test activity. After tensile test activities were completed, microstructural samples from the middle portion were extracted.

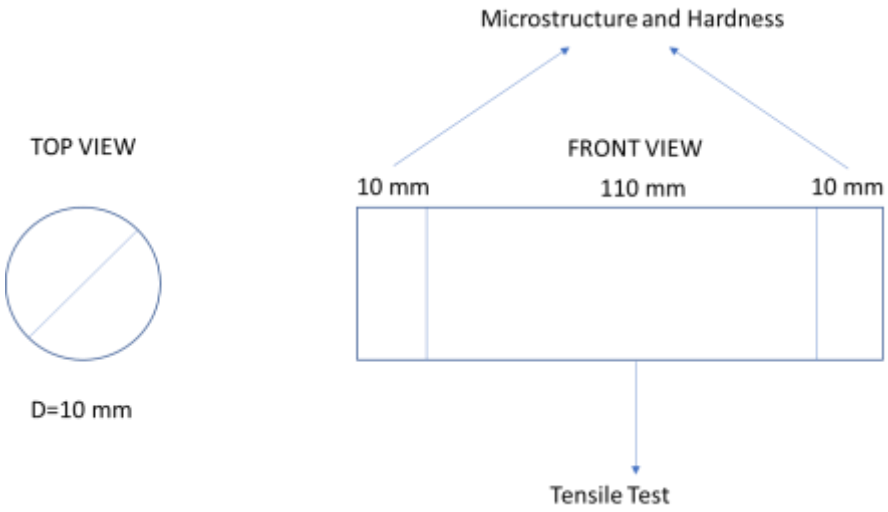

Figure 5.3 Schematic View of As-Machined and As-Build Samples Microstructural Examination

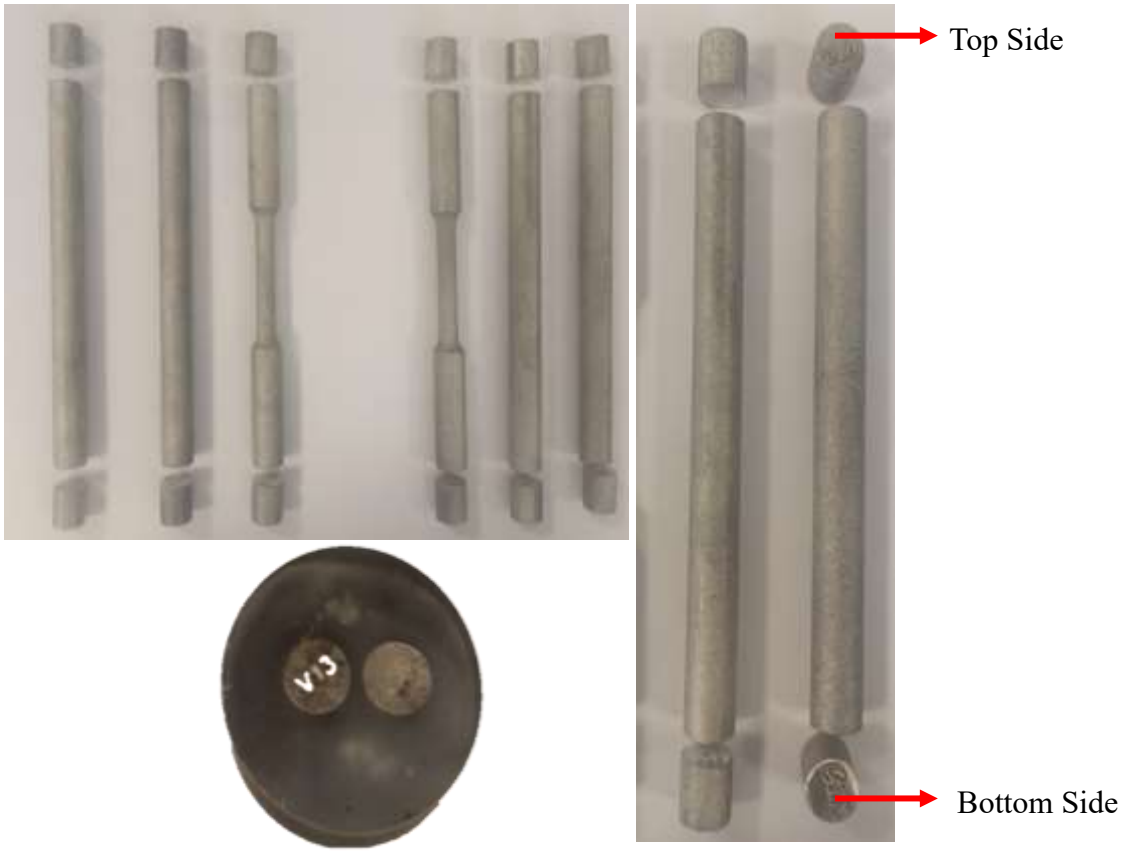

Figure 5.4 Cutting Images of Microstructural Specimens

After obtaining all microstructural specimens, samples were prepared with metallographic specimen preparation methods.

- Firstly, all samples were mounted with bakelite in ATM OPAL 410 machine. All samples were identified as shown in Figure 5.4.
- Then, grinding was applied by using 220, 400, 600, 800, and 1200x grinding papers. Automating grinding machine whose name is ATM SAPHIR 550 was used.
- Then, polishing was performed in order to obtain a polished surface.
- Finally, Keller etchant was used in order for microstructure examination.

Microstructural examinations were conducted by using both optical and scanning electron microscopes, whose brand names are NIKON and PHENOM XL G2, respectively. The total numbers of specimen which were examined is classified as given in Table 5.4. Each specimens cut from the top face of the sample was called as bottom and top, and they were identified as "B" and "T", representatively. Moreover, after tensile tests were completed, additional microstructural review specimens were also extracted from the middle portion of the sample, and it was called as middle, "M".

Table 5.4 Microstrucrual Specimen Identification After Cutting from Top and Bottom Surface

# of Batch	Specimen Identification		Specimen Type
1. Batch	V1	V1-B	As-Machined
		V1-M	
		V1-T	
	V2	V2-B	As-Build
		V2-M	
		V2-T	
	H2	H2-B	As-Machined
		H2-M	
		H2-T	

5.2.2 Destructive Tests

- Tensile Test

INSTRON 5985 machine was used for tensile test activities in order to get tensile and yield strength values together with % elongation.

- Failure Analysis

Failure analysis was conducted by ZEISS EVO 10 machine on fracture surfaces of tensile test specimens.

- Hardness Test

Each microstructural specimen given in Table 5.4 was also dedicated for hardness measurement per ASTM E10, Brinell Method. At least 2 measurements were performed on each specimen. Qness Q60 A+ machine was used for hardness measurement analysis.

5.2.3 Experimental Results

- Tensile Test Results

In the following figures, it can be seen the comparison of all printed samples which are categorized as follows:

- Vertical samples (vertical as-build samples, vertical as-machined samples)
- Horizontal samples (horizontal as-machined samples)

As explained in previous chapters, all horizontal samples are printed as – machined due to difficulties of 3D printing for “dog-bone” shape in horizontal condition, which need many supporters. When quantity of supporter is increased, that is cooling capacity decreases, lower mechanical properties are expected. Thus, this configuration was not studied.

Figure 5.5 indicates the all printed 12 tensile specimens’ test results together with results of 6061 T62 which is given in Table 3.2 and Table 3.3. It can be seen that all samples’ mechanical characteristics are superior than 6061 T62. When Figure 5.5 is reviewed in detail, tensile strength results of printed vertical and horizontal specimens differs due to orientation and surface condition of the specimens. Since vertical samples have less amount of supports, which causes higher cooling rate, their tensile strength values are greater than horizontal ones. Yield strength values are similar when all 12 sample results are reviewed. Since yield strength is a material characteristic, these results have been already expected. It can be easily concluded that machined vertical samples have higher

tensile strength among all samples due to their roughness, and specimen orientation giving higher cooling rate.

Figure 5.5 Strength vs Specimen Numbers for AlSi10Mg Material

Table 5.5 shows the results of yield and tensile strength values together with elongation values.

Table 5.5 All Printed Specimens and 6061 T62 Tensile Strength Results

All Specimens				
		Yield Strength (MPa)	Tensile Strength (MPa)	% Elongation
Vertical	V1	235	381	3.9
	V2	251	437	4.4
	V3	225	378	3.8
	V4	257	438	4.4
	V5	242	378	2.6
	V6	258	440	4.6
Horizontal	H1	262	397	6.9
	H2	259	395	7.3
	H3	257	397	7
	H4	254	394	6.8
	H5	252	395	7.3
	H6	250	391	8.1
Average		250	402	5.6
Standard Deviation		10.5	22.2	1.7
6061 T62 [55]		241.4	289.7	6

Figure 5.6 shows the affect of printed specimen geometry and surface roughness on mechanical properties. As it can be seen, % elongation and tensile strength values have significant differences among as-machined and as-build specimens. As explained in above paragraph, as-build samples having higher supporter, which are needed to be able to obtain desired geometry, causes to slower cooling rate. Therefore, excellent mechanical properties can be achieved by using machined vertical samples.

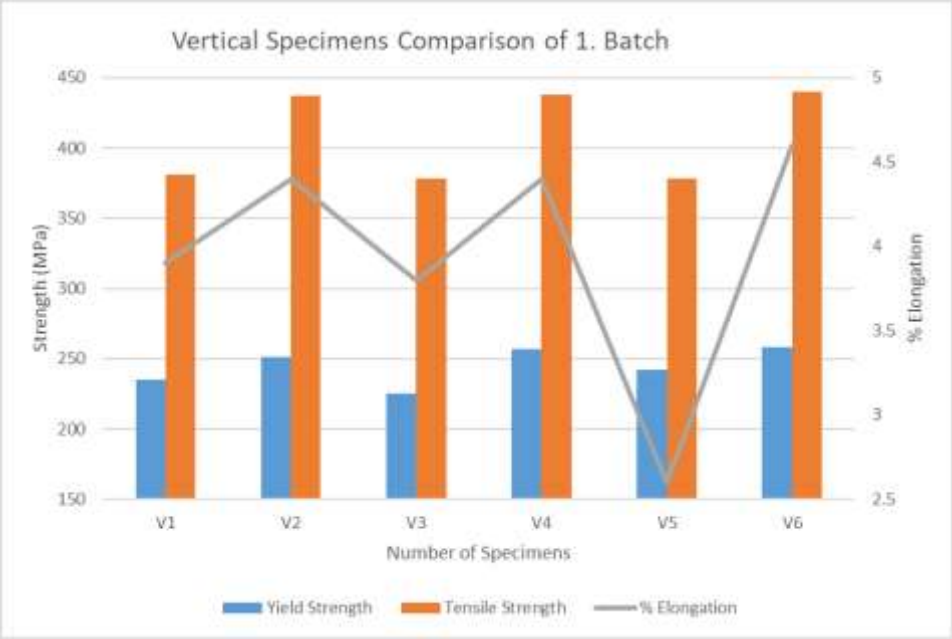

Figure 5.6 Strength vs Specimen Numbers according to Vertical Orientation for AlSi10Mg Material

Table 5.6 shows that standard deviation in tensile strength values. They are very high when compared remaining specimen results. It can be explained that since vertical specimens include 2 different geometry, as-machined and as-build, its effect on tensile strength is considerably higher as explained in previous paragraph.

Table 5.6 Vertical Specimens Tensile Strength Results

Vertical Specimens				
		Yield Strength (MPa)	Tensile Strength (MPa)	% Elongation
Vertical	V1	235	381	3.9
	V2	251	437	4.4
	V3	225	378	3.8
	V4	257	438	4.4
	V5	242	378	2.6
	V6	258	440	4.6
Average		245	409	4.0
Standard Deviation		12.0	29.7	0.7

Figure 5.7 and Table 5.7 show the tensile test results of as-build vertical samples. As explained previously, their results having same orientation and surface geometry have very low standard deviation.

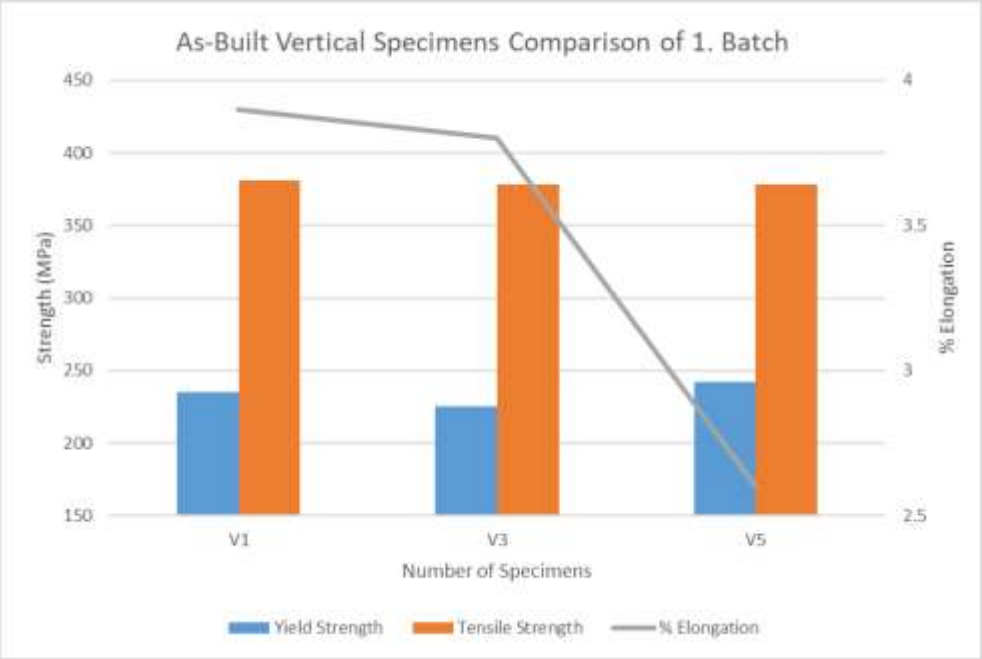

Figure 5.7 As-Build Vertical Specimens Comparison for AlSi10Mg Material

Table 5.7 As-Build Vertical Specimens Tensile Strength Results

As-Built Vertical Specimens				
		Yield Strength (MPa)	Tensile Strength (MPa)	% Elongation
Vertical	V1	235	381	3.9
	V3	225	378	3.8
	V5	242	378	2.6
Average		234	379	3.4
Standard Deviation		7.0	1.4	0.6

Figure 5.8 and Table 5.8 show as-machined vertical specimens' tensile test results. They have the highest tensile strength due to higher cooling rate. However, % elongation results are lower than the horizontal specimens. It can be resulted from again cooling rate.

Since cooling rate is higher than horizontal ones, its % elongation is lower although superior tensile strength values are obtained.

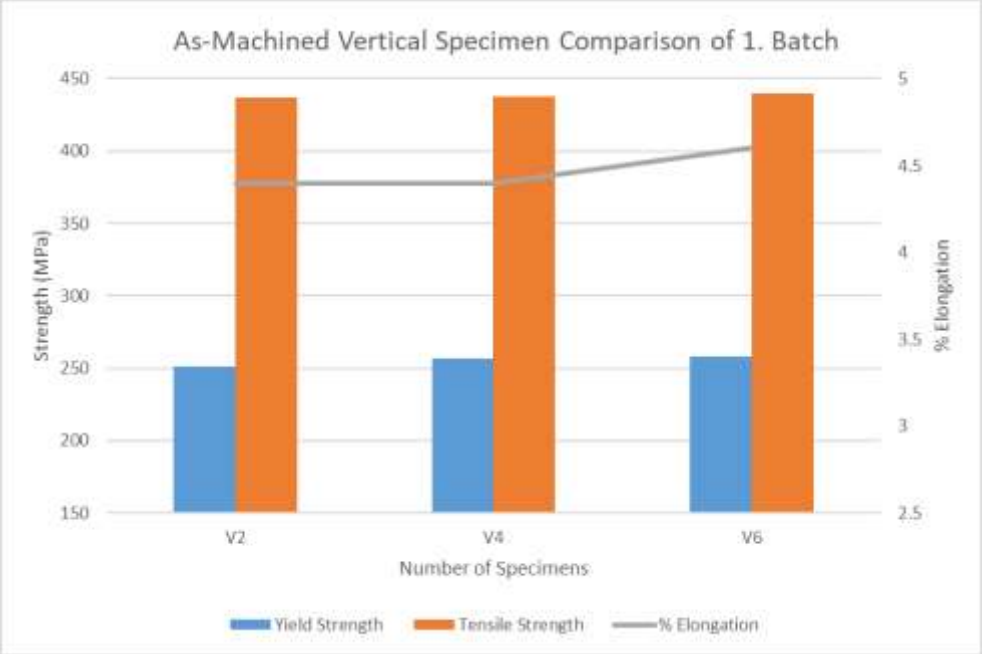

Figure 5.8 As-Machined Vertical Specimens Comparison for AlSi10Mg Material

Moreover, another important conclusion of the results is to obtain lowest standard deviations, which implies to characterize mechanical properties of AlSi10Mg alloys.

Table 5.8 As-Machined Vertical Specimens Tensile Strength Results

As-Machined Vertical Specimens				
		Yield Strength (MPa)	Tensile Strength (MPa)	% Elongation
Vertical	V2	251	437	4.4
	V4	257	438	4.4
	V6	258	440	4.6
Average		255	438	4.5
Standard Deviation		3.1	1.2	0.1

Tensile test results of horizontal specimens having as-machined specimen geometry can be seen in Figure 5.9 and Table 5.9. As seen in Table 5.8, standard deviation among as-machined horizontal specimens are very low.

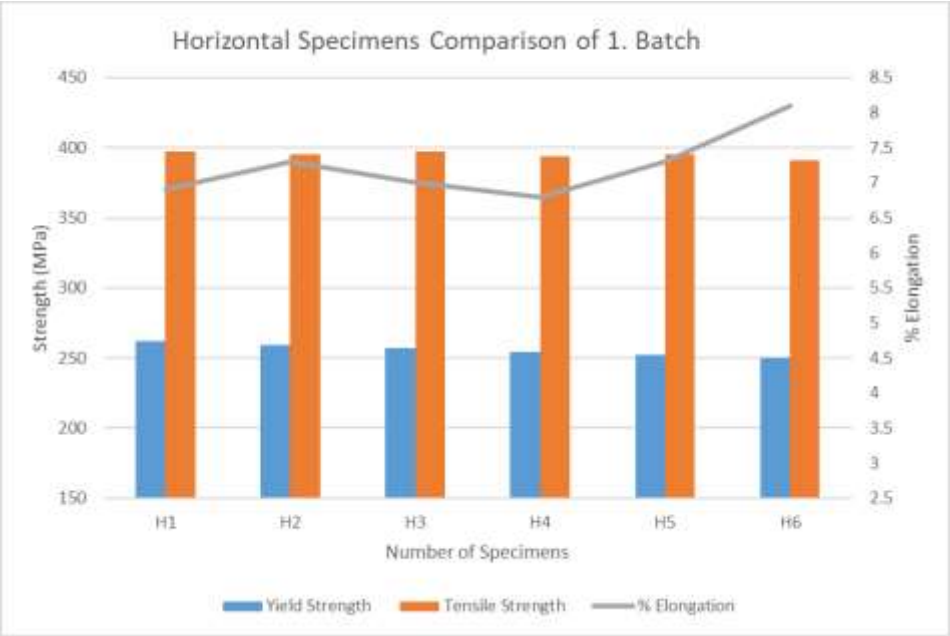

Figure 5.9 Horizontal Specimens Comparison for AlSi10Mg Material

When Table 5.7 and Table 5.9 are compared, which both needs higher supporter than as-machined vertical specimens, % elongation and tensile strength of horizontal specimens are higher than as – build vertical ones, which is opposed condition when compared Table 5.8 and Table 5.9. The reason can be explained as follows although vertical specimens have less supporters, that is higher cooling rate, surface roughness of as-build specimens make them prone to defect formation on the surface, which causes to obtain lower mechanical properties than machined horizontal condition.

Table 5.9 Horizontal Specimens Tensile Strength Results

Horizontal Specimens				
		Yield Strength (MPa)	Tensile Strength (MPa)	% Elongation
Horizontal	H1	262	397	6.9
	H2	259	395	7.3
	H3	257	397	7.0
	H4	254	394	6.8
	H5	252	395	7.3
	H6	250	391	8.1
Average		256	395	7.2
Standard Deviation		4.1	2.0	0.4

As a result of Figure 5.5 to Figure 5.9 and Table 5.5 to Table 5.9;

1. Horizontal samples have higher percent elongation than vertical samples. The reason behind this is the difference in surface roughness and orientation in printing design. Since surface roughness values of as-build samples are very higher than machined samples, crack formation starts from the surface and propagates into the center. In addition, since horizontal samples required more supporter in order to obtain desired geometry during printing, cooling rate of horizontal specimens are slower than vertical samples resulting in higher % elongation.
2. Vertical and machined specimens have highest tensile strength. Since vertical as-machined samples requires minimum amount of supporters, cooling rate is very high which plays an significant role in tensile strength.
3. When as-machined horizontal specimens and as-build vertical specimens are compared, it can be concluded that slow cooling rate which belongs to horizontal samples provides to obtain higher % elongation while surface roughness plays an important role in tensile strength.
4. Yield strength values are similar when all 12 sample results are compared. Since yield strength is a material characteristic, these results have been already expected.
5. When as-machined and as-build specimen results are compared separately, it can be seen that machined samples have less standard deviation than as-build samples due to the reason explained in the previous paragraphs.

- Radiographic Analysis Results

Figure 5.10 shows the X-Ray results. According to the X-ray images, there is no defect found inside the specimens.

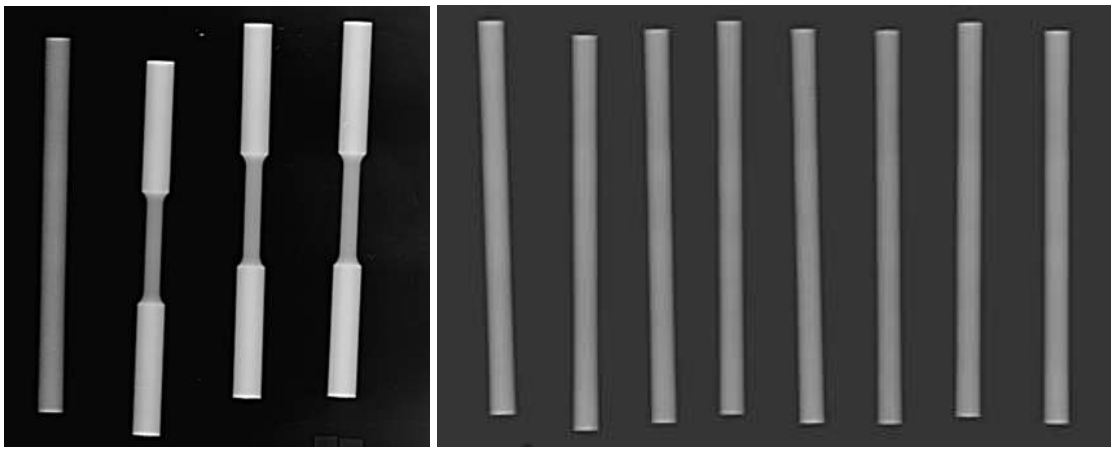

Figure 5.10 X-Ray Results of As-Build and As- Machined Specimens

- Surface Roughness Measurement Results

Figure 5.11 indicates the surface roughness results of as-build samples. The results are found as 10 Ra µm, while as – machined samples have 1.2 Ra µm.

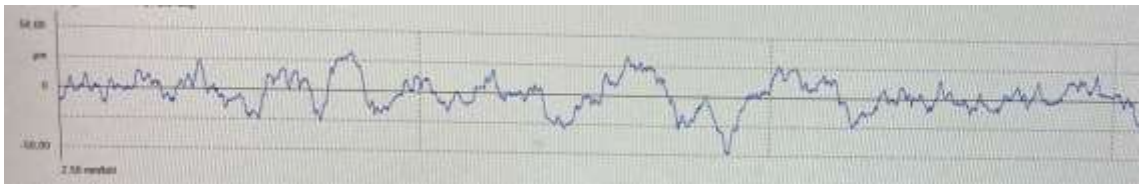

Figure 5.11 Surface Roughness Results

- Fractographic Analysis Results

Fracture surfaces were examined by using scanning electron microscope. In order to represent the all 12 samples, 3 of them shown in Table 5.3 were used. When electron microscope images are reviewed, it is seen mixed failure including both ductile and brittle manner. As it can be understood from Table 5.5, % elongation values are near to 5 % which is a theoretical limit for ductile to brittle transition failure, which implies to see mixed failure surface.

Figure 5.12 shows that all specimens have ductile ridges and they show partial intergranular fracture.

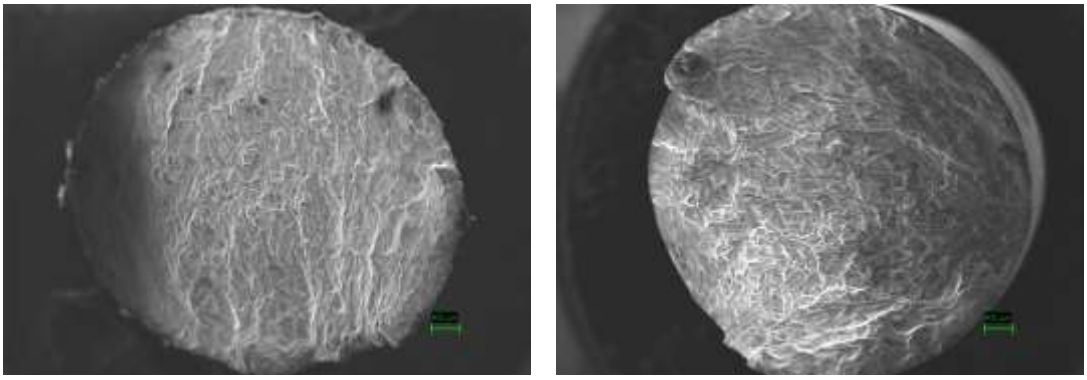

Figure 5.12 Fracture Surfaces of Specimens

Figure 5.13 shows that fracture surfaces have shallow dimples which is the evidence of ductile failure.

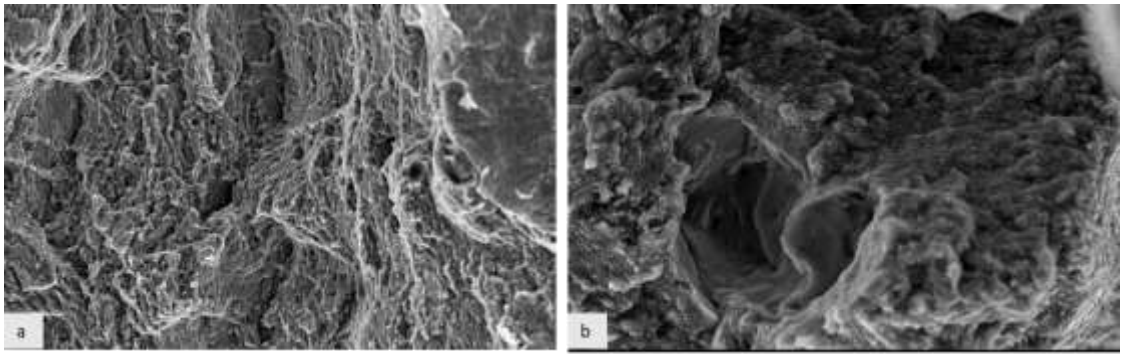

Figure 5.13 Fracture Surfaces at a) 2500x b) 8000x magnifications

Figure 5.14 shows 2 different types of un-melted powders. Figure 5.14-a indicates that the size of powder is approximetaly 30 µm which is the size of powders used in SLM. On the other hand, Figure 5.14-b explains the agglorameted un-melted powders whose sizes are approximately 87 µm.

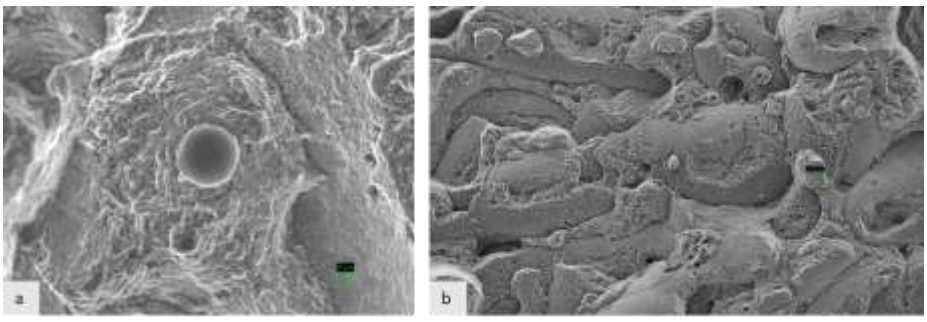

Figure 5.14 Fracture Surfaces Indicating Un-Melted Powders a)30 µm powder b) 87 µm agglorameted un-melted powders

Moreover, number of small pores are also detected during electron microscope examination, which is shown in Figure 5.15. Therefore, those pores are obtained is the fact that gases formed during rapid melting and cooling.

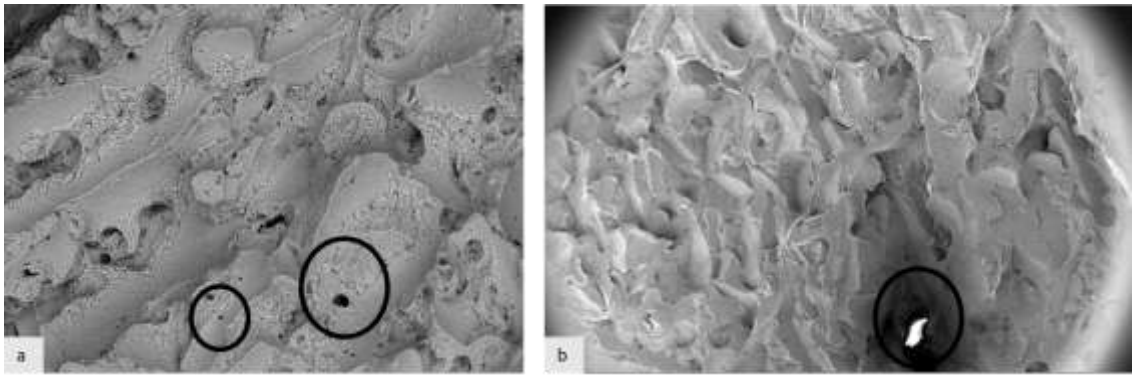

Figure 5.15 Fracture Surfaces Indicating a) Porosities b) Inclusions

- Optical Microstructures Analysis Results

As opposed to conventional cast hypoeutectic Al-Si alloys, microstructure of SLM printed products have different characteristics. In conventional cast alloys, cooling charactresitic is non-directional due to solidification process, and dendrite spacing between primary alpha are not fixed. In the microstructural examination images, characteristics of SLM printed products is seen clearly.

Figure 5.16 shows 4 different magnification of AlSi10Mg specimen. White areas represents the molten pool in which the areas first melting occurs. Solidification rate is very high in melt pools when compared to surrounding areas. For this reason, solidification occurs in dendritic shape in the white zone while surrounding areas has cellular growth due to solidification rate is slower than molten pool. Moreover, grain sizes in molten pool is very small compared to surrounding areas. It can be understood from Figure 5.16 – d that grain size is approximately 1.5 µm.

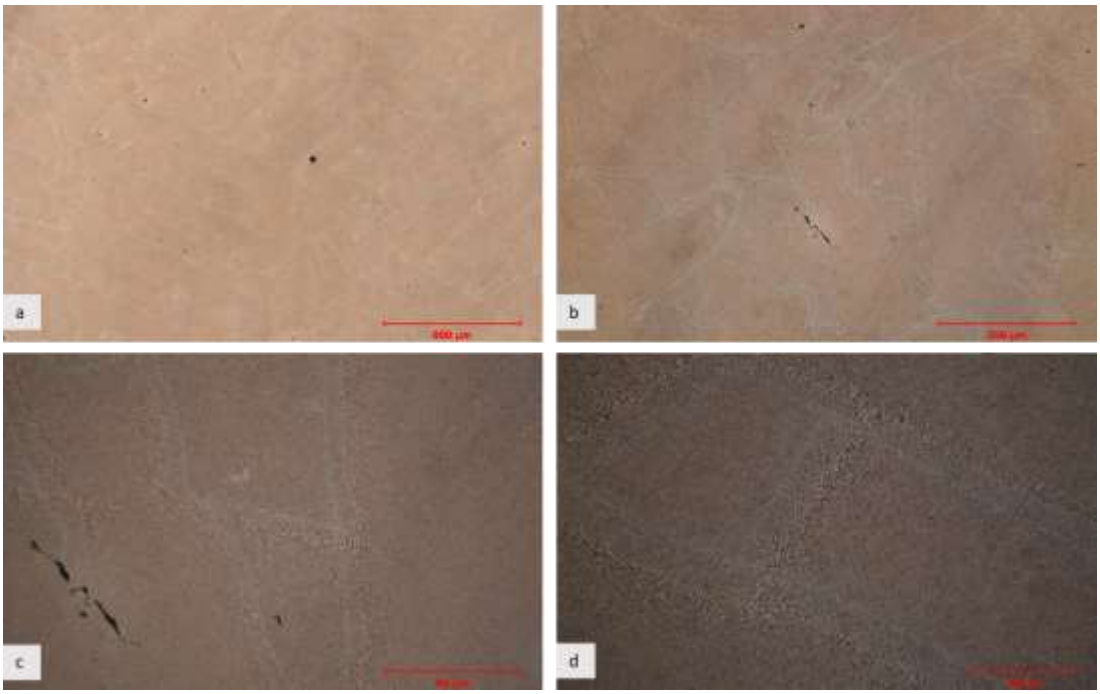

Figure 5.16 Optical Microstructure Images at a) 50x b) 200x c) 500x d) 1000x magnifications

Figure 5.17 indicates 1000x images of the specimens where molten pool areas are seen clearly.

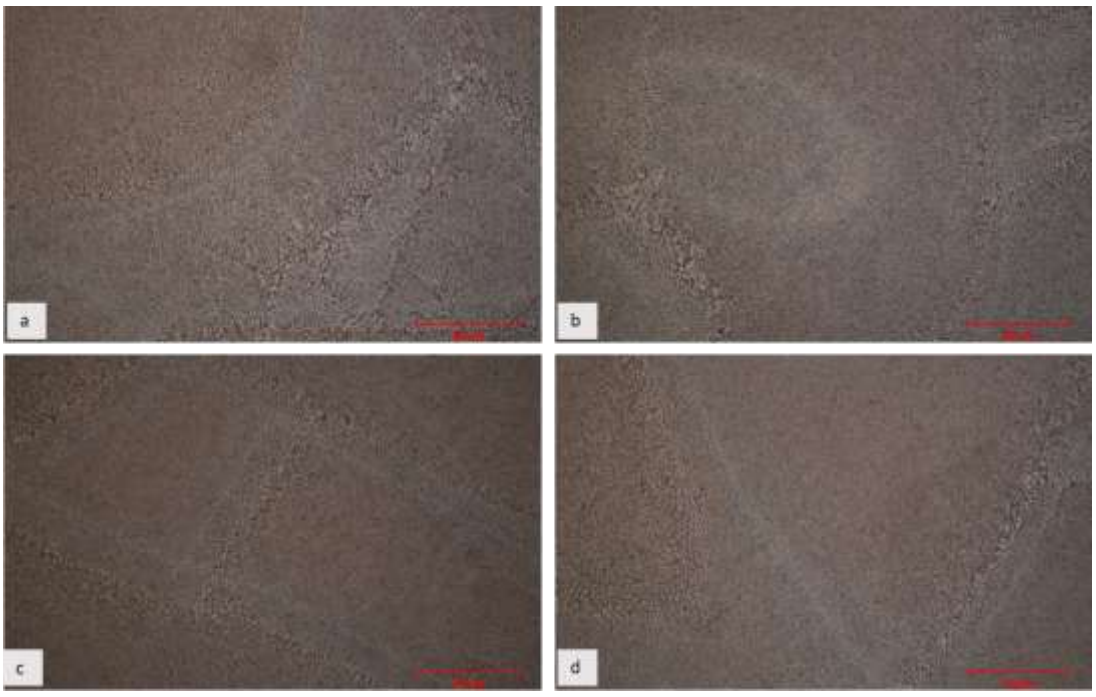

Figure 5.17 Optical Microstructure Images at 1000x magnification

Figure 5.18 indicates the micro images of different locations of the specimens to get better understanding of the distribution of the molten pool areas. All white areas shows the molten pools having rapid cooled zones.

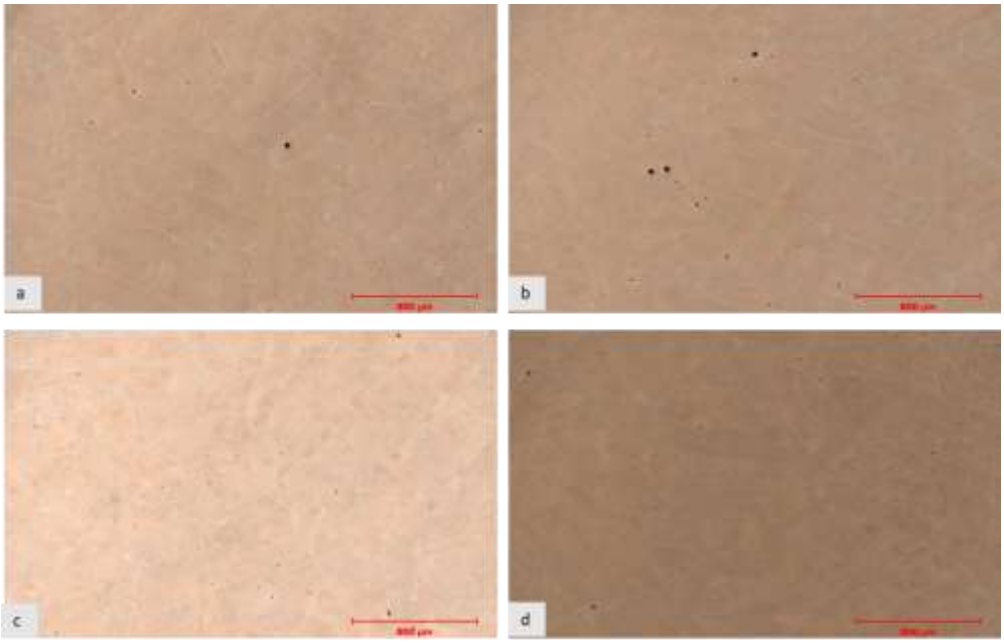

Figure 5.18 Optical Microstructure Images at 50x magnification images of a & b) Middle, c) Bottom, d) Top

Finally, defects like porosities and microshrinkage can also be seen in Figure 5.19 as given in Figure 5.15.

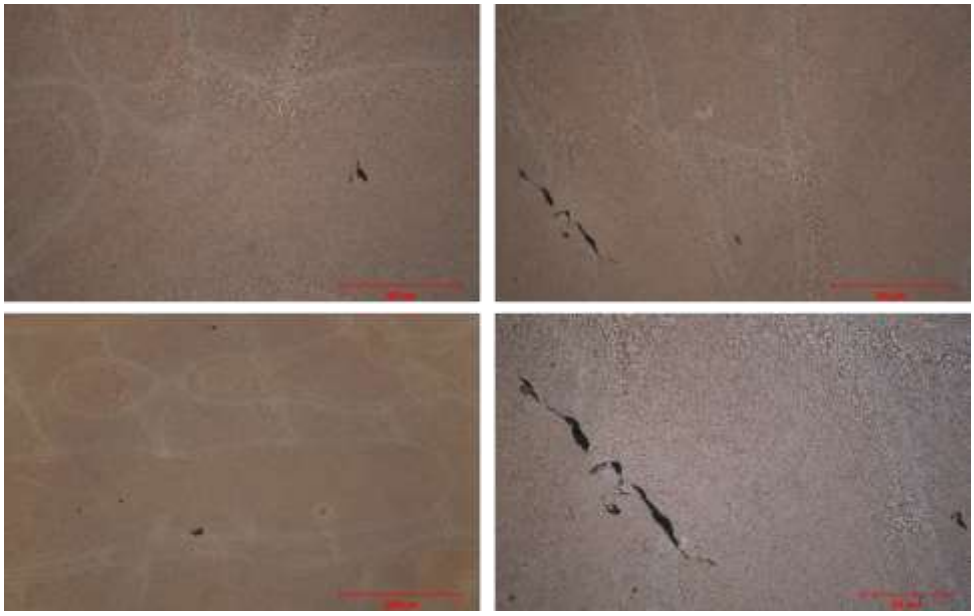

Figure 5.19 Porosities and Microshrinkages Types of Defects

6. CONCLUSION AND FUTURE WORKS

Optimization of the component was performed in 2 different ways, which are topology and size optimizations by using 2 different alloys, Al 6061 and AlSi10Mg. In addition, topology optimization was applied to the design extracted from the bulk model to determine the comparative effectiveness of the optimization in the first and last stages of the design. Moreover, static and modal analysis were applied for initial, topology and size-optimized models. Before the selection of the mesh size, mesh convergence study analysis was performed on the initial model in order to define the optimum mesh size to decrease analysis time.

Static and modal analysis results of the initial model whose material is Al 6061 was defined as base results in order to compare with further analysis results. Modal analysis results of trials were not matched with the natural frequency of the helicopter rotor dynamic system. These were the expected results otherwise it would cause the component to resonate and the part would fail due to fatigue. Topology optimization yielded a decrease in weight at the first stage from 5.86 kg to 4.91 kg, which is the aim of this thesis. Furthermore, static analysis results of topology optimization revealed that both stress, strain, and stiffness results were similar to the initial model. Then, size optimization was also performed in order to see a further decrease in the weight of the tubes. Size optimization revealed a decline in stiffness values for the tube structure while an increase in compliance appeared, while a moderate rise in stress was obtained as expected due to the decrease thickness of tube. However, since the margin of safety was greater than 1, increased stress was evaluated as acceptable. As a result, both topology and size optimization results of Al 6061 T62 provided lighter component while giving satisfying static and modal analysis results. With the help of size optimization, the aforementioned values have reduced the weight of the component from 5.86 to 4.86 kg by changing the thickness value for tubes.

Afterward, all optimizations were repeated for AlSi10Mg material since its mechanical properties are different than Al 6061. Since density values are the same for Al 6061 T62 and AlSi10Mg materials, weight reduction has not occurred.

Then, modal analysis was performed for size optimized model with both materials. However, before static and modal analysis results, experimental material allowable data were revealed by printing 12 tensile samples in SLM machine. Then, elastic modulus,

yield, and tensile strength results were obtained and used as input values for analysis. Since SLM printed samples show anisotropic results, the lowest yield strength and elastic modulus values were selected as input values for analysis results, which are 255 MPa in yield strength and 65 GPa in elastic modulus. Tensile test results indicated that yield strength values are similar for both vertical and horizontal specimens, and both machined and as-build specimens. However, tensile strength and % elongation results revealed differences according to the direction and surface condition. Since horizontal specimens have a slower cooling rate due to higher amounts of supporter requisite, tensile strength results of horizontal specimens are lower than vertical specimens. And, since tensile strength was increased, a reduction in % elongation was yielded. In addition, hardness results, 115 HB, indicated an increment in hardness when compared with Al 6061 T62 whose hardness is approximately 90 HB. After experimental mechanical properties were obtained, both static and modal analyses were repeated for AlSi10Mg material.

When size analysis results are reviewed, similar results with Al 6061T62 were observed. The only apparent difference is the increase in compliance and strain values which resulted from the reduction in elastic modulus of AlSi10Mg compared with Al 6061 T62. Finally, it is seen that the final topology optimized part, which is designed from bulk material to represent the final stage of topology optimization, manufactured with AlSi10Mg resulted in a significant decrease in weight, stress, strain, and compliance values due to the increase in stiffness.

To sum up, experimental tensile test analysis results of AlSi10Mg coupon samples yielded higher mechanical properties than conventional Al 6061 which provided a higher factor of safety for the part. Moreover, all optimization results provided to see lighter and stiffer part. Therefore, both decreases in weight and higher factor of safety are very important for the component in order to use in aerospace.

In the scope of this thesis, future works could be listed as follows;

1. Fatigue test results of AlSi10Mg SLM printed coupons can be revealed.
2. Tensile tests can be performed in different directions from 90° and 0°.
3. Other topology optimization formulations which are mentioned in Table 4.2 can be utilized.
4. For size optimization, constraints and objective can be changed to reach the ideal cross-sectional area for tubes on the bracket.

5. Buckling analysis and thermo-elastic analysis can be applied on the bracket.

6. Optimized part can be printed by SLM machine for component test activity.

7. REFERENCES

[1] Paolini, A., Kollmannsberger, S., & Rank, E. (2019). Additive manufacturing in construction: A review on processes, applications, and digital Additive Manufacturing, 30, 100894planning methods.https://doi.org/10.1016/j.addma.2019.100894.

[2] Additive Manufacturing. FHNW. (n.d.). Retrieved February 5, 2023, from https://www.fhnw.ch/de/die-fhnw/hochschulen/ht/institute/institut-fuer-produkt-und-produktionsengineering/additive-manufacturing

[3] Gibson, L. J., & Ashby, M. F. (1997). Cellular solids: Structure & Properties. Cambridge University Press.

[4] DebRoy, T., Wei, H. L., Zuback, J. S., Mukherjee, T., Elmer, J. W., Milewski, J. O., Beese, A. M., Wilson-Heid, A., De, A., & Zhang, W. (2018). Additive manufacturing of metallic components – process, structure and properties. Progress in Materials Science, 92, 112–224. https://doi.org/10.1016/j.pmatsci.2017.10.001.

[5] Wauthle, R., Vrancken, B., Beynaerts, B., Jorissen, K., Schrooten, J., Kruth, J.-P., & Van Humbeeck, J. (2015). Effects of build orientation and heat treatment on the microstructure and mechanical properties of selective laser melted ti6al4v lattice structures. Additive Manufacturing, 5, 77–84. https://doi.org/10.1016/j.addma.2014.12.008.

[6] Ahmed, R. (2020, March 18). How 3D printed lattice structures improve mechanical properties. 3D Printing. Retrieved February 5, 2023, from https://3dprinting.com/tips-tricks/3d-printed-lattice-structures.

[7] Atzeni, E., & Salmi, A. (2012). Economics of additive manufacturing for end-usable metal parts. The International Journal of Advanced Manufacturing Technology, 62(9-12), 1147–1155. https://doi.org/10.1007/s00170-011-3878-1.

[8] GE9X engine. GE Aerospace. (n.d.). Retrieved February 5, 2023, from https://www.geaerospace.com/propulsion/commercial/ge9x.

[9] M. P. Bendsoe and O. Sigmund, Topology Optimization: Theory, Methods, and Applications, Berlin: Springer, 2004.

[10] Allaire, G., Belhachmi, Z., & Jouve, F. (1996). The homogenization method for topology and shape optimization. single and multiple loads case. Revue Européenne Des Éléments Finis, 5(5-6), 649–672. https://doi.org/10.1080/12506559.1996.10511241

[11] Francfort, G., Murat, F., & Tartar, L. (1995). Fourth-order moments of nonnegative measures on S2 and applications. Archive for Rational Mechanics and Analysis, 131(4), 305–333. https://doi.org/10.1007/bf00380913

[12] Bendsøe, M. P., & Sigmund, O. (2003). Topology Optimization: Theory, methods and applications. Springer.

[13] Junk, S., Klerch, B., & Hochberg, U. (2019). Structural optimization in lightweight design for additive manufacturing. Procedia CIRP, 84, 277–282. https://doi.org/10.1016/j.procir.2019.04.277

[14] Hans A. Eschenauer and Niels Olhoff. Topology optimization of continuum structures: A review. Appl. Mech. Rev., 54(4):331–390, 2001.

[15] G. I. N. Rozvany. Aims, scope, methods, history and unified terminology of computeraided topology optimization in structural mechanics. Struct. Multidisc. Optim., 21:90– 108, 2000.

[16] BERNDTSSON, A. L. I. K. I., & MATTIASSON, A. N. D. R. E. A. S. (2019). Structural Optimization of Mechanical Systems Topology optimization with parametrization of hardpoint positions (thesis).

[17] SIMP method for topology optimization. SIMP Method for Topology Optimization - 2023 - SOLIDWORKS Help. (n.d.). Retrieved February 5, 2023, fromhttps://help.solidworks.com/2023/english/solidworks/cworks/c_simp_method_topology.htm

[18] Tanskanen, P. 2002. The evolutionary structural optimization method: Theoretical aspects. Computer Methods in Applied Mechanics and Engineering. 191 (47-48), 5485-5498.

[19] Edwards, C. S., Kim, H. A., & Budd, C. J. (2007). An evaluative study on ESO and simp for optimising a cantilever tie—beam. Structural and

Multidisciplinary Optimization, 34(5), 403–414. https://doi.org/10.1007/s00158-007-0102-x

[20] ALLAIRE, G., CAVALLINA, L., MIYAKE, N., OKA, T., & YACHIMURA, T. (2019). The homogenization method for topology optimization of structures: Old and new. Interdisciplinary Information Sciences, 25(2), 75–146. https://doi.org/10.4036/iis.2019.b.01

[21] Blog, T. G. E. A. (2018, October 4). Manufacturing milestone: 30,000 additive fuel nozzles - the GE Aerospace blog: Aviation & Flight News. The GE Aerospace Blog | Aviation & Flight News. Retrieved January 12, 2023, from https://blog.geaerospace.com/manufacturing/manufacturing-milestone-30000-additive-fuel-nozzles/

[22] Topography Optimization - Altair University. (n.d.). Retrieved January 17, 2023, from https://altairuniversity.com/wp content/uploads/2015/11/Topography_opti.pdf

[23] Czerwinski, F. (2021). Current trends in automotive lightweighting strategies and materials. Materials, 14(21), 6631. https://doi.org/10.3390/ma14216631

[24] EKİNCİ, F. A. T. İ. H. (2022). *Design For Additive Manufacturing Of The Turbojet Engine Part Via Topology Optimization And Structural Analysis* (thesis).

[25] MSC Community. (n.d.). Retrieved January 25, 2023, from https://simcompanion.hexagon.com/customers/s/article/What-are-topography-optimization-and-its-limitations

[26] Deng, C., Wang, Y., Qin, C., Fu, Y., & Lu, W. (2022). Self-directed online machine learning for topology optimization. Nature Communications, 13(1). https://doi.org/10.1038/s41467-021-27713-7

[27] Yuksel, O. (2019). Yapisal Mühendislikte Kullanilan TOPOLOJİ Eniyilemesi Yöntemleri üzerine Genel bir bakiş. Kırklareli Üniversitesi Mühendislik Ve Fen Bilimleri Dergisi. https://doi.org/10.34186/klujes.606666

[28] P. W. Christensen et al. An introduction to structural optimization. English. Vol. 153. Dordrecht: Springer, 2009;2008.

[29] Ponnusamy, P., Rahman Rashid, R. A., Masood, S. H., Ruan, D., & Palanisamy, S. (2020). Mechanical properties of SLM-printed aluminium alloys: A Review. Materials, 13(19), 4301. https://doi.org/10.3390/ma13194301

[30] Groen, J. P., & Sigmund, O. (2017). Homogenization-based topology optimization for high-resolution manufacturable microstructures. International Journal for Numerical Methods in Engineering, 113(8), 1148–1163. https://doi.org/10.1002/nme.5575

[31] R.J Yang. and C.H. Chuang, Optimal Topology Design Using Linear Programming, Structural Optimization, 68, pp. 265-290, 1993.

[32] Antonova, V., Alekseev, S., Tarasov, A., Scheglova, N., Klyavin, O., & Borovkov, A. (2019). Analysis and use of SIMP method in optimization of a car hood design. E3S Web of Conferences, 140, 04017. https://doi.org/10.1051/e3sconf/201914004017

[33] 3DEXPERIENCE platform. (n.d.). Retrieved February 11, 2023, from https://make.3dexperience.3ds.com/processes/photopolymerization

[34] Ttad. (2022, April 13). *Principle of 3D printing-stereolithography(sla)*. Bring Idea To Life. Retrieved February 12, 2023, from https://www.tanerxun.com/principle-of-3d-printing-stereolithography/.html

[35] Universität Zürich. (2022, September 5). *Digital Light Processing (DLP)*. UZH. Retrieved February 12, 2023, from https://www.amf.uzh.ch/en/additive-manufacturing/our_technologies/dlp.html

[36] Chandra, S., Kumar, D. P. R., Prasad, S., & Sainath. (2017). *Continuous Liquid Interface Production (CLIP)*.

[37] *What is SLS 3D printing?* Hubs. (n.d.). Retrieved February 18, 2023, from https://www.hubs.com/knowledge-base/what-is-sls-3d-printing/#how-does-sls-3d-printing-work

[38] *What is binder jetting 3D printing?* Hubs. (n.d.). Retrieved February 25, 2023, from https://www.hubs.com/knowledge-base/introduction-binder-jetting-3d-printing/#characteristics

[39] *Sheet lamination: Siemens Software*. Siemens Digital Industries Software. (n.d.). Retrieved February 25, 2023, from https://www.plm.automation.siemens.com/global/en/our-story/glossary/sheet-lamination/55512

[40] Suttey, L. J. (n.d.). Evaluation of metallurgical and mechanical properties of alsi10mg produced by Selective Laser Melting,2018 (thesis).

[41] Aboulkhair, N. T., Simonelli, M., Parry, L., Ashcroft, I., Tuck, C., & Hague, R. (2019). 3D printing of aluminium alloys: Additive manufacturing of aluminium alloys using selective laser melting. Progress in Materials Science, 106, 100578. https://doi.org/10.1016/j.pmatsci.2019.100578

[42] Jia, Q., Rometsch, P., Cao, S., Zhang, K., & Wu, X. (2019). Towards a high strength aluminium alloy development methodology for selective laser melting. Materials & Design, 174, 107775. https://doi.org/10.1016/j.matdes.2019.107775

[43] Skill-Lync. (n.d.). *Week 12:project 2-meshing of rear wheel holder challenge : Skill-lync*. Skill. Retrieved March 12, 2023, from https://skill-lync.com/student-projects/week-12-project-2-meshing-of-rear-wheel-holder-challenge-232

[44] GRIHON, S., KROG, L., & HERTEL, K. (2003). *A380 Weight Savings Using Numerical Structural Optimisation, Pg:*8–9.

[45] Zhu, J.-H., Zhang, W.-H., & Xia, L. (2015). Topology optimization in aircraft and aerospace structures design. *Archives of Computational Methods in Engineering*, *23*(4), 595–622. https://doi.org/10.1007/s11831-015-9151-2

[46] *3D printing satellite parts with EOS Technology: EOS GmbH*. 3D Printing Satellite Parts with EOS Technology | EOS GmbH. (n.d.). Retrieved February 26, 2023, from https://www.eos.info/en/all-3d-printing-applications/ruag-aerospace-3d-printed-satellite-components#video_32452

[47] Liang, M., Hu, J., Li, S., & Chen, Z. (2018). Topology optimization of transmission gearbox under multiple working loads. *Advances in Mechanical Engineering*, *10*(11), 168781401881345. https://doi.org/10.1177/1687814018813454

[48] Shind, T., Sheth, Y., Sindkar, M., & Shinde, A. (2021). *Design, Analysis and Natural Frequency Optimization of Engine Mount Bracket,Pg1-16:*.

[49] Alghamdi, F., & Haghshenas, M. (n.d.). Small-scale characterization of additively manufactured and heat treated alsi10mg (thesis).

[50] Niu, M. C.-Y. (2011). *Airframe stress analysis and sizing*. Conmilit Press.

[51] Limbasiya, N., Jain, A., Soni, H., Wankhede, V., Krolczyk, G., & Sahlot, P. (2022). A comprehensive review on the effect of process parameters and post-process treatments on microstructure and mechanical properties of selective laser melting of alsi10mg. Journal of Materials Research and Technology, 21, 1141–1176. https://doi.org/10.1016/j.jmrt.2022.09.092

[52] Aboulkhair, N. T. (2015). *Additive manufacture of an aluminium alloy: Processing, microstructure, and mechanical properties* (thesis).

[53] Wang, S. Krylov Subscpace Methods for Topology Optimization on Adaptive Meshes. Ph.D. Dissertation, University of Illinois, Champaign, IL, USA, 2007

[54] Bendsøe, M.P.; Kikuchi, N. Generating optimal topologies in structural design using a homogenization method. Comput. Methods Appl. Mech. Eng. 1988, 71, 197–224.

[55] MMPDS-04, Metallic Materials Properties Development and Standardization, April 2008

[56] Koppen, S., Langelaar, M., & van Keulen, F. (2022). A simple and versatile topology optimization formulation for flexure synthesis. *Mechanism and Machine Theory*, *172*, 104743. https://doi.org/10.1016/j.mechmachtheory.2022.104743